EM SIMULATION USING THE LAGUERRE-FDTD

SCHEME FOR MULTISCALE 3-D

INTERCONNECTIONS

A Dissertation
Presented to
The Academic Faculty

By

Myunghyun Ha

In Partial Fulfillment
of the Requirements for the Degree
Doctor of Philosophy in the
School of Electrical and Computer Engineering

Georgia Institute of Technology
December 2011

EM SIMULATION USING THE LAGUERRE-FDTD SCHEME FOR MULTISCALE 3-D INTERCONNECTIONS

Approved by:

Dr. Madhavan Swaminathan, Advisor
School of Electrical and Computer Engineering
Georgia Institute of Technology

Dr. Andrew F. Peterson
School of Electrical and Computer Engineering
Georgia Institute of Technology

Dr. Manos M. Tentzeris
School of Electrical and Computer Engineering
Georgia Institute of Technology

Dr. Muhannad Bakir
School of Electrical and Computer Engineering
Georgia Institute of Technology

Dr. Hao Min Zhou
School of Mathematics
Georgia Institute of Technology

Date Approved: Nov. 3, 2011

Dedicated to my parents

ACKNOWLEDGEMENTS

Ten years ago, I was a sophomore and about to choose my major. After long and careful consideration, I decided to study electrical engineering. Now, I am about to receive the Ph.D. degree in the electrical and computer engineering, which is the highest academic degree awarded by universities in the United States. It would not have been possible without the support of many people. I would like to express my gratitude to the people who inspired and encouraged me.

First of all, I cannot thank my advisor Prof. Madhavan Swaminathan enough for giving me an invaluable opportunity to work in EPSILON group. Without his continuous trust, guidance and enthusiasm and encouragement, none of my achievements during my Ph.D. life could be possible. His insight based on theoretical and industrial background directed my research to the right way. I would like to thank my committee members, Prof. Andrew F. Peterson, Prof. Manos M. Tentzeris, Prof. Muhannad Bakir, and Prof. Hao Min Zhou for taking much of their precious time to give me constructive advice and feedback.

I am forever grateful to Prof. Joungho Kim, my former advisor during my Master's degree, for the opportunity he gave me to be a Tera lab's member. The foundation I built with the experiences and studies in the Tera lab had a strong effect on shaping my ideas. I would like to thank my manager Dr. Dan Oh and mentor Dr. Joong Ho Kim at Rambus during my summer internship in 2009 for giving me great opportunities to learn and be inspired.

I was very lucky to have such good people as my colleagues in EPSILON group: Wansuk, Tae Hong, Lalgudi, Krishna S., Janani, Ranjeeth, Vishal, Sukruth, Aswani, Krishna B., Ki Jin, Nevin, Abhilash, Nithya, Narayanan, Eddy, Tapo, Suzanne, Jae Young, Jianyong, Kyu, Satyan, Biancun, Stephen, David, Rishik, Sung Joo, Ming, and Diapa. I would like to thank Suzanne, Eddy, and Jae Young who joined Tech together in 2007 for having fun and helping each other. Four years spent with them are priceless to me. I cannot forget weekly MSDT meetings where I had a lot of helpful discussions with Krishna S., Krishna B., Ki Jin, Jae Young, Narayanan,

Ranjeeth, and Bernie. My special thanks go to Krishna S., Ki Jin, Narayanan, Jianyong, and Jae Young who gave me invaluable discussions on my research ideas. The research faculty of the EPSILON group has been excellent mentors and I would like to thank Dr. Daehyun Chung, Dr. Andy Seo, and Dr. Sunghwan Min for constructive discussions.

I can never thank enough to my parents. All of my accomplishments through my life have been possible by endless loves and unconditional supports from my father, Mr. Jaein Ha, and my mother, Ms. Soonhye Kim. They provided me the best environment to follow my dream, armed me with positive attitude, and encouraged me whenever I was in difficult time. I sincerely appreciate all the gifts from my parents. Therefore, this dissertation is dedicated to my beloved parents. I wish their health and happiness.

TABLE OF CONTENTS

LIST OF TABLES

LIST OF FIGURES

SUMMARY

As the current electronic trend is toward integrating multiple functions in a single electronic device, there is a clear need for increasing integration density which is becoming more emphasized than in the past. To meet the industrial need and realize the new system-integration law [1], three-dimensional (3-D) integration is becoming necessary. 3-D integration of multiple functional IC chip/package modules requires co-simulation of the chip and the package to evaluate the performance of the system accurately. Due to large scale differences in the physical dimensions of chip-package structures, the chip-package co-simulation in time-domain using the conventional FDTD scheme is challenging because of Courant-Friedrich-Levy (CFL) condition that limits the time step. Laguerre-FDTD has been proposed to overcome the limitations on the time step. To enhance performance and applicability, SLeEC methodology [2] has been proposed based on the Laguerre-FDTD method. However, the SLeEC method still has limitations to solve practical 3-D integration problems.

This dissertation proposes further improvements of the Laguerre-FDTD and SLeEC method to address practical problems in 3-D interconnects and 3-D integration. A method that increases the accuracy in the conversion of the solutions from Laguerre-domain to time-domain is demonstrated. A methodology that enables the Laguerre-FDTD simulation for any length of time, which was challenging in prior work, is proposed. Therefore, the analysis of the low-frequency response can be performed from the time-domain simulation for a long time period. An efficient method to analyze frequency-domain response using time-domain simulations is introduced. Finally, to model practical structures, it is crucial to model dispersive materials. A Laguerre-FDTD formulation for frequency-dependent dispersive materials is derived in this dissertation and has been implemented.

CHAPTER I

INTRODUCTION

1.1 Background and Motivation

In the semiconductor industry, a need for high performance, small size, and low-cost solutions for functional integration is becoming more significant. To keep up with the industrial need, three-dimensional (3-D) integration called system-on-package (SoP) as shown in Figure 1 is becoming necessary. As more functionality is integrated into the package, electromagnetic interactions within the package pose a significant problem. The problem in high-density integration which includes 3-D structures is the requirement for tools that enable the design and analysis of package structures and ICs within the package together at the same time, which is also called "chip-package co-simulation".

Both chip-package co-simulation and the analysis of 3-D interconnection structures have a common ground in that there is a large scale difference in the physical dimensions of the structure to be dealt with. For chip-package co-simulation, structures with a wide range of physical dimensions from tens of nanometers to a few millimeters need to be considered together. In 3-D integration, vertical interconnections are realized using through-silicon via (TSV) interconnections, employing silicon as a new packaging substrate. Use of TSV increases the integration density considerably. Silicon oxide used as an oxide liner in TSVs plays an important role in the TSV's electrical response. However, the oxide's thickness is very thin compared to the via itself. Therefore, TSV structures fall into the category of multiscale structures. This dissertation however is not limited to TSVs and addresses any structure that contains a multiscale geometry.
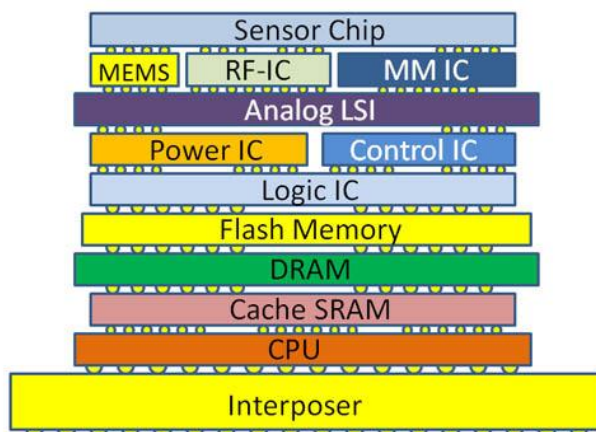
Figure 1. 3-D multi-functional vertical integration in semiconductor packages. (Courtesy: Interconnect and Package Center, Georgia Institute of Technology.)

Traditional time-domain techniques, such as the finite-difference time-domain method, are limited by the well-known Courant-Friedrich-Levy (CFL) condition and are not suitable for the simulation of multiscale problems which arise in high-density integration. The CFL condition poses an upper bound on the time step to obtain stable simulation results. The CFL limit is inversely proportional to the smallest mesh dimensions. In the case of the simulation of multiscale structures, small dimensions in the structure require a very fine mesh, which makes the time step prohibitively small. An unconditionally stable scheme using Laguerre polynomials, which is referred to as Laguerre-FDTD, is suggested for simulation of multiscale structures in 3-D integration as an alternative to FDTD. Because of the Laguerre-FDTD's unconditional stability, the time step in the Laguerre-FDTD is not limited by CFL condition. Therefore, the Laguerre-FDTD enables significant speed-up in the simulation of multiscale structures arising in high-density integration.

1.2 Contribution

Based on the Laguerre-FDTD, SLeEC methodology has been proposed to enhance the performance, which will be introduced in detail in CHAPTER III. However, both SLeEC methodology and Laguerre-FDTD still have difficulties in the application to practical problems. This dissertation focuses on enhancing the Laguerre-FDTD's applicability. The following work has been completed in this dissertation:

1. An efficient method to recover a time-domain waveform from solutions in the Laguerre-domain has been proposed.

2. The limited time duration for which the Laguerre-FDTD could be simulated earlier has been resolved, enabling low-frequency analysis using Laguerre-FDTD.

3. A frequency-domain analysis methodology using the Laguerre-FDTD has been proposed.

4. A Laguerre-FDTD based formulation for frequency-dependent dispersive materials has been proposed.

Based on the above contributions, a software tool has been developed that solves electromagnetic fields in time domain for a given structure and a given source current, which is called SLeEC. The term 'SLeEC' comes from SLeEC methodology which is an improved version of Laguerre-FDTD and will be shown in detail in 3.2. Because the code was initially developed using the SLeEC methodology and has been upgraded as the research in this dissertation proceeds, the software tool's name is still 'SLeEC' although improvements made in this dissertation are not limited to SLeEC methodology, but applicable to general Laguerre-FDTD. The flow chart in Figure 2 shows how the software tool works. It reads two files regarding structure description and simulation setup. The software is explained in detail in Appendix C.
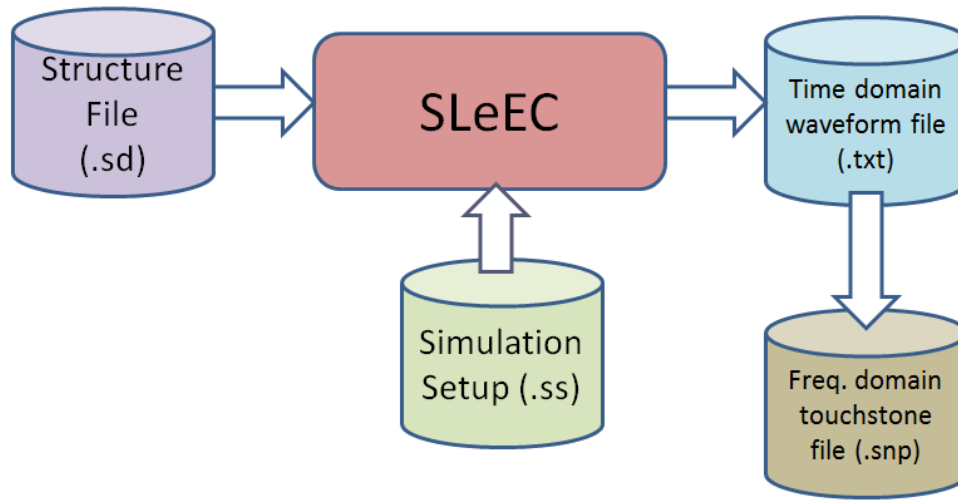
Figure 2. Flow chart of a software tool 'SLeEC'

1.3 Organization of the Thesis

The rest of this dissertation consists of the following chapters. Chapter 2 starts with the description of the nature and origin of the problem being addressed. Chapter 3 describes prior work in the unconditionally stable FDTD scheme using Laguerre polynomials in detail. SLeEC methodology, which is an improved version of the Laguerre-FDTD method, is explained in detail as well as the original Laguerre-FDTD method in Chapter 3. Chapter 4 proposes a method to generate a transient waveform from the solution in the Laguerre-domain that enhances accuracy and computation time compared to prior work. In Chapter 5, the limitation on simulation time in the prior work is introduced and a method to resolve the limitation is proposed, which enables low-frequency analysis using the Laguerre-FDTD method. Chapter 6 discusses a methodology to analyze frequency-domain response using Laguerre-FDTD. The fundamental theory to calculate frequency-domain parameters from transient simulation is introduced at the beginning. Then improved methods that enhance the efficiency of the analysis are shown.

4

Chapter 7 proposes a Laguerre-FDTD formulation for modeling losses. A mathematical technique to convert a formulation using frequency-domain information to Laguerre-domain is introduced. Chapter 8 documents practical 3-D test examples that show model-to-hardware correlation and correlation to commercial tools. Chapter 9 concludes this dissertation and summarizes the contributions of this dissertation. Finally, Chapter 10 proposes future work.

CHAPTER II

ORIGIN AND HISTORY OF THE PROBLEM

2.1 Need for 3-D integration

Modern electronics require higher computational speed and data bandwidth with a smaller form factor, which result in an increasing level of transistor integration density in semiconductors [3] [4]. From the development of integrated circuits (IC) to system-on-chip (SoC), silicon-based technology has driven the growth of the integration technology. SoC is increasing the capability for miniaturization of various computing units and memory blocks [5]. However, the extension of the functionality with SoC is limited. Multimedia mobile devices require various subsystems including analog, radio frequency (RF), and sensor submodules in addition to digital computing units, and SoC has difficulty in integrating various heterogeneous subsystems on one single chip. Furthermore, the time-to-market for SoC is not short enough to meet the rapidly-changing trends of mobile applications [6].

Package-based system integration is an attractive solution for multi-functional integration for mobile applications. As advanced packaging technology enables the integration of various submodules in a single package platform, the realization of the multi-functional system becomes easier. With progress in processing technology, package-based system component densities will increase, as shown in Figure 3 [1].
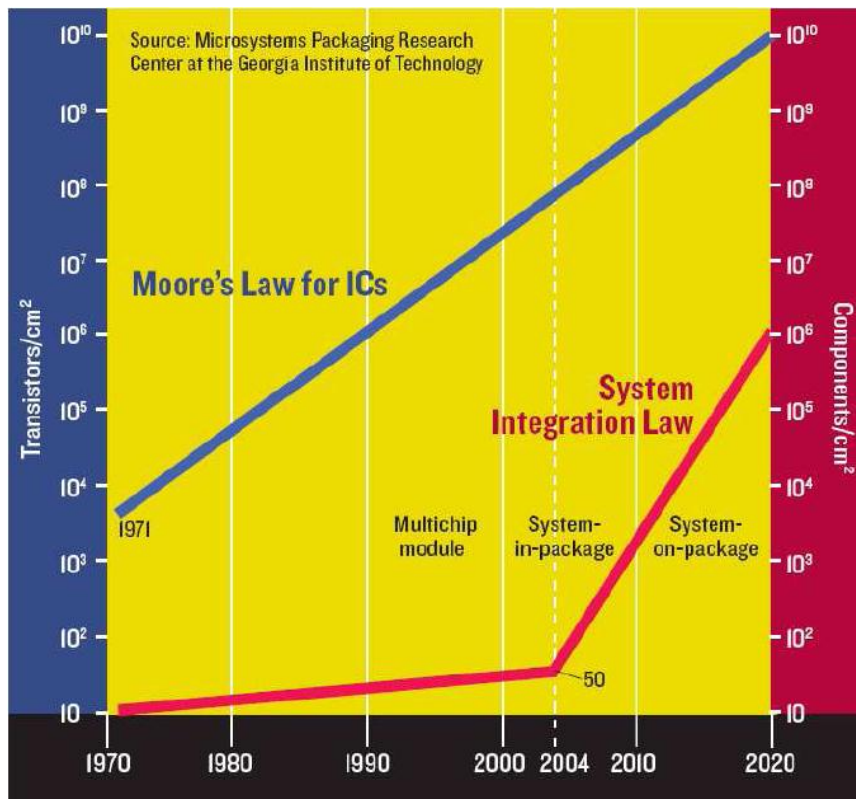
Figure 3. An estimate of system-integration density driven by package-based technology [1].

For the realization of the new system-integration law, instead of cramming chips on the planar substrate layout as in traditional multi-chip modules (MCM), the integration of submodules vertically using 3-D space is employed in such multilayer structures, as shown in Figure 4. Currently, the 3-D packaging concept is realized through System-in-Package (SiP), which stacks bare or packaged ICs vertically. System-on-Package (SoP) is a more extensive architecture of 3-D integration than SiP and contains embedded passives and active components in a package. For microminiaturization, 3-D integration is the fundamental method being pursued for today's package-based system integration [7] [8].

7
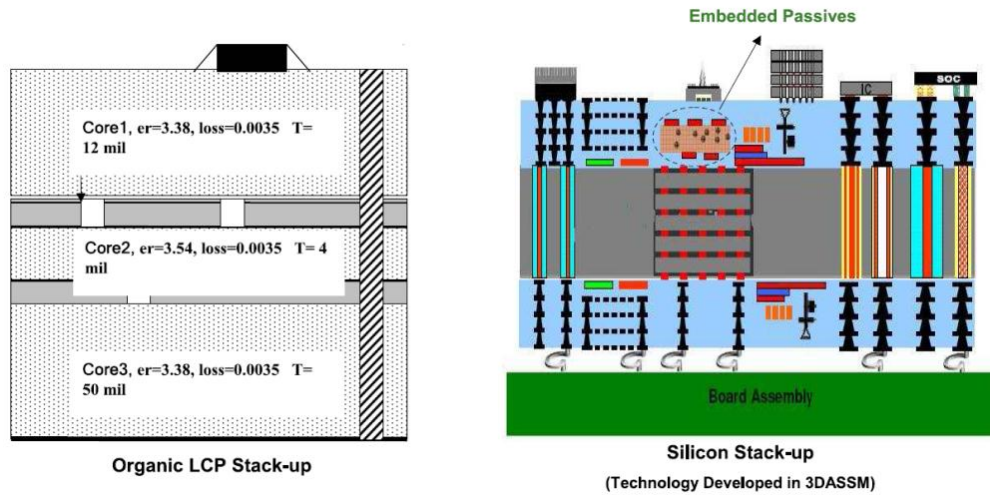
Figure 4. Typical multilayer stack-ups used/proposed for electronic packages. (Courtesy: Packaging Research Center, Georgia Institute of Technology.)

2.2 Major Electromagnetic Design Challenges

There are several critical electromagnetic effects that one needs to carefully consider in the design of SiP or SoP. Those effects can be classified into reflected noise, simultaneous switching noise (SSN), crosstalk noise, and attenuation [9] [10].

Reflection noise is produced due to impedance mismatch. Incorrect terminations and signal path discontinuities cause impedance mismatch and result in overshoot, undershoot, and ringing. Possible sources of impedance mismatch are changes in the signal-trace width, branching of the signal trace, and signal-line crossing a gap in the reference plane giving rise to return-path discontinuity. SSN is caused by parasitic inductance of the power-distribution network (PDN). SSN causes fluctuation in the voltage between power and ground planes, especially when a large number of devices switch simultaneously. It is because SSN is proportional to the inductance of the PDN and the first derivative of current flow with respect to time. Crosstalk noise is caused by the direct electromagnetic coupling between signal traces and vias. The close placement of such

8

structures results in the coupling of electric and magnetic fields, giving rise to mutual capacitance and mutual inductance, respectively. Attenuation is caused by dielectric dispersion and conductor loss. Attenuation suppresses the signal's amplitude therefore signal-to-noise ratio (SNR) is degraded. In addition, loss is proportional to the frequency. The high-frequency component and low-frequency component of a signal are attenuated differently, which results in signal distortion deteriorating signal integrity.

As more functionality is integrated in a package with higher performance in the 3-D integration, the electromagnetic interactions within the package become more significant and complex. Especially, in the case of a mixed-signal system containing digital, analog, and RF modules, it is critical to fully characterize the system at the design level using an electromagnetic solver. Therefore, 3-D interconnection design requires engineering solutions for issues that were not observed earlier in the planar-interconnection design.

2.3 Challenges in Time-Domain Simulation Method

Key features in chip-package structures that need to be addressed in the design of 3-D integrated systems stem from its multiscale physical dimensions. For chip-package co-simulation, structures with a wide range of physical dimensions from tens of nanometers to a few millimeters need to be considered together. In 3-D integration, vertical interconnections are realized using through-silicon via (TSV) interconnections which also fall into the category of multiscale structures.

2.3.1 Finite-Difference Time-Domain Method

The finite-difference time-domain (FDTD) scheme is a ubiquitous method for transient electromagnetic (EM) analysis [11]. The main drawback of FDTD is the Courant-Friedrich-Levy (CFL) condition, which limits the time step for obtaining stable and accurate simulation results

[12]. In EM analysis, smaller mesh dimension contributes to a smaller CFL time step. In mathematical form, the CFL condition for EM simulation is given by

$$\Delta t < \frac{1}{v_{max}} \left(\left(\frac{1}{\Delta x} \right)^2 + \left(\frac{1}{\Delta y} \right)^2 + \left(\frac{1}{\Delta z} \right)^2 \right)^{-\frac{1}{2}}, \tag{1}$$

where v_{max} is the maximum phase velocity of the wave propagation while Δx, Δy, and Δz are the smallest mesh dimensions in the x, y, and z directions [12]. The time-step limit for numerical stability can be derived using dispersion analysis [12].

The CFL condition is a major bottleneck in using FDTD for co-simulation of multiscale structures. Multiscale dimensions in a chip-package structure are shown in Figure 5. The on-chip structures are in the nanometer scale, the solder pads typically have a diameter of 50 μm, the package interconnects are in the 100 μm range, and the package structures, such as the power-ground planes, are in the mm scale. The on-chip structures that are in the nm range require fine meshes, making the time step prohibitively small.
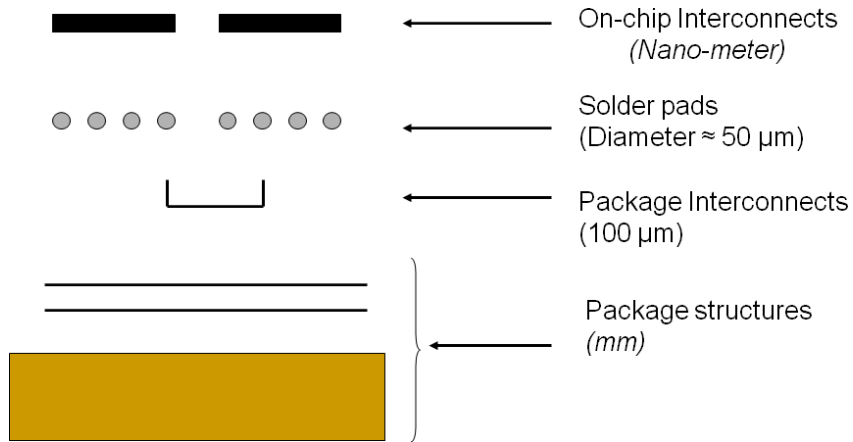
Figure 5. Multiscale features in a chip-package structure.

2.3.2 Alternate Time-Domain Methods

The multi-resolution time-domain (MRTD) scheme using scaling and wavelet functions has been shown to provide savings of an order of magnitude with respect to execution time [13]. By using orthonormal wavelet spatial expansions, the MRTD scheme can reduce the spatial discretization to two steps per wavelength. However, the stability condition for MRTD becomes more stringent [14]. Hollands' method proposed in [15] has been used to reduce the simulation time by avoiding fine meshing for thin wires, by modeling the thin wires with a cell size smaller than the FDTD cell. The MRTD and Holland method are not applicable to general structures arising in high-density integration.

To eliminate the CFL stability condition, implicit methods can be used. These implicit techniques, in particular, alternating-direction-implicit (ADI) methods, have been used in solving heat transfer problems [16], followed by various unconditionally stable finite-difference formulations for parabolic equations [17]. Such implicit techniques were introduced into the FDTD schemes for solving Maxwell's equations, resulting in an implicit unconditionally stable ADI–FDTD method [18]. The ADI-FDTD scheme can be used to speed up simulation and has been shown to provide a $10\times$ improvement in the simulation time [19]. A rigorous theoretical proof of the unconditional stability was presented with numerical verifications in [20]. Due to the removal of the CFL conditions in the ADI-FDTD method, the time step is no longer restricted by the stability conditions, but by the modeling accuracy of the algorithm. One of the factors that affect the accuracy is numerical dispersion. In [21], it has been shown that using a time step larger than the CFL limit results in increased numerical dispersion in the ADI-FDTD based method.

Recently, based on the time-domain finite element method (FEM), the time-domain finite element reduction recovery (FE-RR) method has been proposed [22]. The time-domain FE-RR method has an advantage of linear complexity, which is suitable to solve very large scale and

11

complex problems. The time-domain FE-RR method has been improved to have unconditional stability by employing unconditionally stable time-domain differencing schemes [23]. However, since the time-domain FE-RR method is a marching-on-time scheme, similar to ADI-FDTD, the author believes that larger time-step then CFL limit may introduce computational error even though the stability of the simulation is maintained.

2.4 Laguerre-FDTD and SLeEC methodology

Laguerre-FDTD and SLeEC methodologies have been proposed to overcome the limitation on the time step in the conventional FDTD. They use Laguerre polynomials to ensure unconditional stability of the simulation and are explained in detail in CHAPTER III. However, they still have limitations when used to solve the practical 3-D integration problems, e.g., the difficulty to obtain the low-frequency response and to treat frequency-dependent material properties. For the Laguerre polynomial based methods to be applicable to practical problems, it is crucial to resolve these limitations, which motivated this research.

CHAPTER III

TRANSIENT SIMULATION USING LAGUERRE POLYNOMIALS

Laguerre-FDTD can be significantly faster than FDTD and other time-domain methods especially for packaging problems containing multiscale dimensions. By using an implicit-solution technique, a decrease in simulation time has been achieved at the expense of an increase in memory consumption. More importantly, because of the Laguerre-FDTD's unconditional stability, the time-step limitation has been removed. Since the Laguerre-FDTD is a marching-on-time scheme, a time step larger than Courant-Friedrich-Levy (CFL) limit does not deteriorate the accuracy of the simulation. In contrast, other methods such as ADI-FDTD [18] suffer from numerical dispersion when the time-step is larger than the CFL limit [21].

3.1 *Laguerre-FDTD*

An unconditionally stable implicit-FDTD scheme using Laguerre polynomials has been proposed in [24]. The method presented in [24] is referred to as the Laguerre-FDTD scheme in this dissertation. The Laguerre-FDTD is an unconditionally stable scheme and therefore, the time step is not limited by the CFL condition. In [24], it has been shown that the Laguerre-FDTD can be 80 to 100 times faster than the conventional FDTD scheme where a marching-on-time method is used to update the electromagnetic fields. Because of the unconditional stability of the transient simulation using Laguerre polynomials and the use of an implicit computational method, the author believes that the Laguerre-FDTD method is ideally suited for the simulation of multiscale structures arising in chip-package co-design.

3.1.1 Weighted Laguerre Polynomials as Basis Functions

Consider the set of polynomials defined by

$$L_p(t) = \frac{e^t}{p!}\frac{d^p}{dt^p}(t^p e^{-t}), \text{ for } p \geq 0, t \geq 0. \tag{2}$$

$L_p(t)$ is the Laguerre polynomial of order p. Note that the Laguerre polynomials are causal, which means that they are defined for time $t \geq 0$. The Laguerre polynomials satisfy a recursive relationship given by

$$L_0(t) = 1, \tag{3}$$

$$L_1(t) = 1 - t, \tag{4}$$

$$pL_p(t) = (2p - 1 - t)L_{p-1}(t) - (p - 1)L_{p-2}(t); for\ p \geq 2. \tag{5}$$

The Laguerre polynomials are orthogonal with respect to the weighting function e^{-t}:

$$\int_0^\infty e^{-t} L_p(t) L_q(t) dt = \delta_{pq}, \tag{6}$$

where δ_{pq} is the Kronecker delta. Therefore, an orthonormal set of basis functions $\{\varphi_0, \varphi_1, \varphi_2 \dots\}$ can be derived from (6) as follows:

$$\varphi_p(t, s) = e^{-\frac{s \cdot t}{2}} L_p(s \cdot t), \tag{7}$$

where $s > 0$ is a time-scale factor. These basis functions are referred to as the Laguerre basis functions. The Laguerre basis functions are also orthogonal with respect to the scaled time variable $\bar{t}$, which can be expressed as

$$\int_0^\infty \varphi_u(\bar{t})\varphi_v(\bar{t})d\bar{t} = \delta_{uv}, \tag{8}$$

where $\bar{t} = s \cdot t$. In (8), $\bar{t}$ is the time multiplied by the time-scale factor s. The Laguerre basis functions for orders $p = 0 - 4$ without the time-scale factor are plotted in Figure 6. The basis functions fluctuate in the order of seconds as shown by the x-axis in Figure 6. Such change rate is too slow to represent time-domain waveforms resulting from the chip-package problems, whose bandwidth is in the GHz range. Therefore, the need for the time-scale factor arises.

14

Note that the Laguerre basis functions converge to zero as $t \rightarrow \infty$. Therefore, arbitrary functions spanned by these basis functions also converge to zero as $t \rightarrow \infty$, which means that any function consisting of Laguerre basis functions is unconditionally stable.
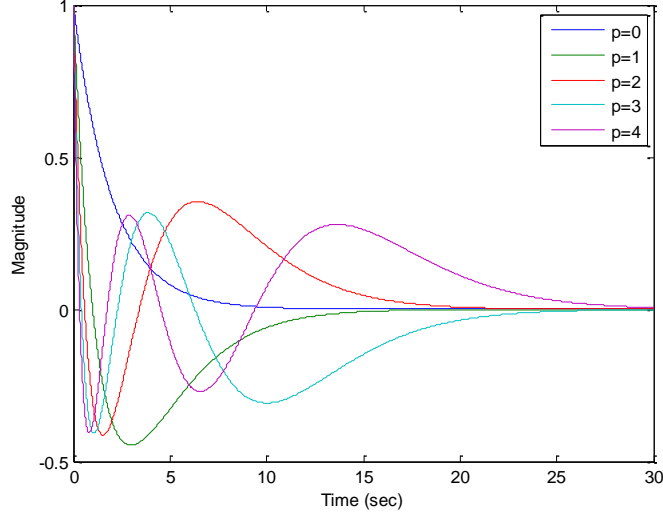
Figure 6. Laguerre basis functions for orders $p = 0$ to $p = 4$.

3.1.2 FDTD with Laguerre Basis Functions

Consider the following three of six Maxwell's differential equations [12]:

$$\frac{\partial E_y}{\partial t} = \frac{1}{\epsilon} \left(\frac{\partial H_x}{\partial z} - \frac{\partial H_z}{\partial x} - J_y \right), \tag{9}$$

$$\frac{\partial H_x}{\partial t} = \frac{1}{\mu} \left(\frac{\partial E_y}{\partial z} - \frac{\partial E_z}{\partial y} \right), \tag{10}$$

$$\frac{\partial H_z}{\partial t} = \frac{1}{\mu} \left(\frac{\partial E_x}{\partial y} - \frac{\partial E_y}{\partial x} \right). \tag{11}$$

Using the Laguerre basis functions, the temporal coefficients for the electric and magnetic fields in (9)-(11) can be expanded as

$$E_y(\vec{r}, t) = \sum_{p=0}^{\infty} E_y^p(\vec{r}) \varphi_p(\bar{t}), \tag{12}$$

15

$$H_x(\vec{r}, t) = \sum_{p=0}^{\infty} H_x^p(\vec{r}) \varphi_p(\bar{t}), \tag{13}$$

$$H_z(\vec{r}, t) = \sum_{p=0}^{\infty} H_z^p(\vec{r}) \varphi_p(\bar{t}), \tag{14}$$

where $\bar{t} = s \cdot t$, and s is the time-scale factor. The first derivative of the field variables with respect to time t can be expressed in terms of the temporal coefficients as

$$U(\vec{r}, t) = s \sum_{p=0}^{\infty} \left(0.5 U_p(\vec{r}) + \sum_{k=0,p>0}^{p-1} U_k(\vec{r}) \right) \varphi_p(\bar{t}), \tag{15}$$

where $U(\vec{r}, t)$ is a casual function [25]. Using (15), (12)-(14) can be inserted to (9)-(11) as follows:

$$s \sum_{p=0}^{\infty} \left(0.5 E_y^p(\vec{r}) + \sum_{k=0,p>0}^{p-1} E_y^k(\vec{r}) \right) \varphi_p(\bar{t})$$

$$= \frac{1}{\varepsilon(\vec{r})} \sum_{p=0}^{\infty} \left[\frac{\partial}{\partial z} H_x^p(\vec{r}) - \frac{\partial}{\partial x} H_z^p(\vec{r}) \right] \varphi_p(\bar{t}) \tag{16}$$

$$- \frac{J_y(\vec{r}, t)}{\varepsilon(\vec{r})},$$

$$s \sum_{p=0}^{\infty} \left(0.5 H_x^p(\vec{r}) + \sum_{k=0,p>0}^{p-1} H_x^k(\vec{r}) \right) \varphi_p(\bar{t})$$

$$= \frac{1}{\mu(\vec{r})} \sum_{p=0}^{\infty} \left[\frac{\partial}{\partial z} E_y^p(\vec{r}) - \frac{\partial}{\partial y} E_z^p(\vec{r}) \right] \varphi_p(\bar{t}), \tag{17}$$

$$s \sum_{p=0}^{\infty} \left(0.5 H_z^p(\vec{r}) + \sum_{k=0,p>0}^{p-1} H_z^k(\vec{r}) \right) \varphi_p(\bar{t})$$

$$= \frac{1}{\mu(\vec{r})} \sum_{p=0}^{\infty} \left[\frac{\partial}{\partial y} E_x^p(\vec{r}) - \frac{\partial}{\partial x} E_y^p(\vec{r}) \right] \varphi_p(\bar{t}). \tag{18}$$

To eliminate the time-dependent terms $\varphi_p(\bar{t})$, a temporal Galerkin's testing procedure of (16)-(18) can be performed by using the orthogonal property of the Laguerre basis functions. By multiplying both sides of (16)-(18) by $\varphi_p(\bar{t})$ and integrating over $\bar{t} = [0, \infty)$, we get

$$s \left(0.5 E_y^p(\vec{r}) + \sum_{k=0,p>0}^{p-1} E_y^k(\vec{r}) \right)$$

$$= \frac{1}{\varepsilon(\vec{r})} \left(\frac{\partial}{\partial z} H_x^p(\vec{r}) - \frac{\partial}{\partial x} H_z^p(\vec{r}) \right) - \frac{J_y^p(\vec{r})}{\varepsilon(\vec{r})}, \tag{19}$$

$$s \left(0.5 H_x^p(\vec{r}) + \sum_{k=0,p>0}^{p-1} H_x^k(\vec{r}) \right) = \frac{1}{\mu(\vec{r})} \left(\frac{\partial}{\partial z} E_y^p(\vec{r}) - \frac{\partial}{\partial y} E_z^p(\vec{r}) \right), \tag{20}$$

$$s \left(0.5 H_z^p(\vec{r}) + \sum_{k=0,p>0}^{p-1} H_z^k(\vec{r}) \right) = \frac{1}{\mu(\vec{r})} \left(\frac{\partial}{\partial y} E_x^p(\vec{r}) - \frac{\partial}{\partial x} E_y^p(\vec{r}) \right), \tag{21}$$

where

$$J_y^p(\vec{r}) = \int_0^{\infty} J_y(\vec{r}, t) \varphi_q(\bar{t}) d\bar{t}. \tag{22}$$

Consider the standard FDTD Yee cell [11] shown in Figure 7. The cross sections of the FDTD cell at the locations marked by the dotted lines in Figure 7 are shown in Figure 8. The cross sections in Figure 8 are viewed by standing at $+\infty$ of the y, x, and z axis and facing the Yee cell, respectively.

Figure 7. Standard Yee cell.

Figure 8. Sections of the Yee cell marked by the dotted lines in Figure 7 parallel to the *xz*, *yz*, and *xy* planes, respectively. Dots indicate direction of the fields pointing out of the page.

Rewriting (19)-(21) in a matrix form after discretization using the central-difference scheme in space as shown in Figure 7 and Figure 8, we have

18

$$E_y^q \big|_{i,j+\frac{1}{2},k} = -C_x^E \big|_{i,j,k} \left(H_z^q \big|_{i+\frac{1}{2},j+\frac{1}{2},k} - H_z^q \big|_{i-\frac{1}{2},j+\frac{1}{2},k} \right)$$

$$+ C_z^E \big|_{i,j,k} \left(H_x^q \big|_{i,j+\frac{1}{2},k+\frac{1}{2}} - H_x^q \big|_{i,j+\frac{1}{2},k-\frac{1}{2}} \right) \tag{23}$$

$$- \frac{2}{s\varepsilon} J_y^q \big|_{i,j+\frac{1}{2},k} - 2 \sum_{l=0,q>0}^{q-1} E_y^l \big|_{i,j+\frac{1}{2},k},$$

$$H_x^q \big|_{i,j+\frac{1}{2},k+\frac{1}{2}} = -C_y^H \big|_{i,j,k} \left(E_z^q \big|_{i,j+1,k+\frac{1}{2}} - E_z^q \big|_{i,j,k+\frac{1}{2}} \right)$$

$$+ C_z^H \big|_{i,j,k} \left(E_y^q \big|_{i,j+\frac{1}{2},k+1} - E_y^q \big|_{i,j+\frac{1}{2},k} \right) \tag{24}$$

$$- 2 \sum_{l=0,q>0}^{q-1} H_x^l \big|_{i,j+\frac{1}{2},k+\frac{1}{2}},$$

$$H_z^q \big|_{i+\frac{1}{2},j+\frac{1}{2},k} = -C_x^H \big|_{i,j,k} \left(E_y^q \big|_{i+1,j+\frac{1}{2},k} - E_y^q \big|_{i,j+\frac{1}{2},k} \right)$$

$$+ C_y^H \big|_{i,j,k} \left(E_x^q \big|_{i+\frac{1}{2},j+1,k} - E_x^q \big|_{i+\frac{1}{2},j,k} \right) \tag{25}$$

$$- 2 \sum_{l=0,q>0}^{q-1} H_z^l \big|_{i+\frac{1}{2},j+\frac{1}{2},k},$$

where

$$C_x^E \big|_{i,j,k} = \frac{2}{s\varepsilon_{i,j,k}\Delta x_i}, \tag{26}$$

$$C_z^E \big|_{i,j,k} = \frac{2}{s\varepsilon_{i,j,k}\Delta z_k}, \tag{27}$$

$$C_x^H \big|_{i,j,k} = \frac{2}{s\mu_{i,j,k}\Delta x_i}, \tag{28}$$

$$C_y^H \big|_{i,j,k} = \frac{2}{s\mu_{i,j,k}\Delta y_j}, \tag{29}$$

19

$$C^H_{z\,i,j,k} = \frac{2}{s\mu_{i,j,k}\Delta z_k}. \tag{30}$$

Inserting (24) and (25) into (23) and rewriting (23), we have

$$C^*_y\big|_{i,j+\frac{1}{2},k} E^q_{y\,i,j+\frac{1}{2},k} + C^*_x\big|_{i+\frac{1}{2},j+1,k} E^q_{x\,i+\frac{1}{2},j+1,k} +$$

$$C^*_x\big|_{i+\frac{1}{2},j,k} E^q_{x\,i+\frac{1}{2},j,k} + C^*_x\big|_{i-\frac{1}{2},j+1,k} E^q_{x\,i-\frac{1}{2},j+1,k} +$$

$$C^*_x\big|_{i-\frac{1}{2},j,k} E^q_{x\,i-\frac{1}{2},j,k} + C^*_y\big|_{i+1,j+\frac{1}{2},k} E^q_{y\,i+1,j+\frac{1}{2},k} +$$

$$C^*_y\big|_{i,j+\frac{1}{2},k+1} E^q_{y\,i,j+\frac{1}{2},k+1} + C^*_y\big|_{i,j+\frac{1}{2},k-1} E^q_{y\,i,j+\frac{1}{2},k-1} + \tag{31}$$

$$C^*_y\big|_{i-1,j+\frac{1}{2},k} E^q_{y\,i-1,j+\frac{1}{2},k} + C^*_z\big|_{i,j+1,k+\frac{1}{2}} E^q_{z\,i,j+1,k+\frac{1}{2}} +$$

$$C^*_z\big|_{i,j+1,k-\frac{1}{2}} E^q_{z\,i,j+1,k-\frac{1}{2}} + C^*_z\big|_{i,j,k+\frac{1}{2}} E^q_{z\,i,j,k+\frac{1}{2}} +$$

$$C^*_z\big|_{i,j,k-\frac{1}{2}} E^q_{z\,i,j,k-\frac{1}{2}} = C^c_y\big|_{i,j+\frac{1}{2},k},$$

where

$$C^*_{y\,i,j+\frac{1}{2},k} = 1 + C^E_x\big|_{i,j,k} C^H_x\big|_{i,j,k} + C^E_x\big|_{i,j,k} C^H_x\big|_{i-1,j,k}$$

$$+ C^E_z\big|_{i,j,k} C^H_z\big|_{i,j,k} + C^E_z\big|_{i,j,k} C^H_z\big|_{i,j,k-1}, \tag{32}$$

$$C^*_{x\,i+\frac{1}{2},j+1,k} = C^E_x\big|_{i,j,k} C^H_y\big|_{i,j,k}, \tag{33}$$

$$C^*_{x\,i+\frac{1}{2},j,k} = -C^E_x\big|_{i,j,k} C^H_y\big|_{i,j,k}, \tag{34}$$

$$C^*_{x\,i-\frac{1}{2},j+1,k} = C^E_x\big|_{i,j,k} C^H_y\big|_{i-1,j,k}, \tag{35}$$

$$C^*_{x\,i-\frac{1}{2},j,k} = -C^E_x\big|_{i,j,k} C^H_y\big|_{i-1,j,k}, \tag{36}$$

$$C^*_{y\,i+1,j+\frac{1}{2},k} = -C^E_x\big|_{i,j,k} C^H_x\big|_{i,j,k}, \tag{37}$$

$$C^*_{y\,i,j+\frac{1}{2},k} = C^E_z \big|_{i,j,k} C^H_z \big|_{i,j,k}, \tag{38}$$

$$C^*_{y\,i,j+\frac{1}{2},k-1} = C^E_z \big|_{i,j,k} C^H_z \big|_{i,j,k-1}, \tag{39}$$

$$C^*_{y\,i-1,j+\frac{1}{2},k} = -C^E_x \big|_{i,j,k} C^H_x \big|_{i-1,j,k}, \tag{40}$$

$$C^*_{z\,i,j+1,k+\frac{1}{2}} = C^E_z \big|_{i,j,k} C^H_y \big|_{i,j,k}, \tag{41}$$

$$C^*_{z\,i,j+1,k-\frac{1}{2}} = -C^E_z \big|_{i,j,k} C^H_y \big|_{i,j,k-1}, \tag{42}$$

$$C^*_{z\,i,j,k+\frac{1}{2}} = -C^E_z \big|_{i,j,k} C^H_y \big|_{i,j,k}, \tag{43}$$

$$C^*_{z\,i,j,k-\frac{1}{2}} = C^E_z \big|_{i,j,k} C^H_y \big|_{i,j,k-1}, \tag{44}$$

$$
\begin{aligned}
C^c_y \big|_{i,j+\frac{1}{2},k} = {} & 2C^E_x \big|_{i,j,k} \sum_{\substack{l=0.q>0}}^{q-1} H^l_z \big|_{i+\frac{1}{2},j+\frac{1}{2},k} \\
& - 2C^E_x \big|_{i,j,k} \sum_{\substack{l=0.q>0}}^{q-1} H^l_z \big|_{i-\frac{1}{2},j+\frac{1}{2},k} \\
& - 2C^E_z \big|_{i,j,k} \sum_{\substack{l=0.q>0}}^{q-1} H^l_z \big|_{i,j+\frac{1}{2},k+\frac{1}{2}} \\
& + 2C^E_z \big|_{i,j,k} \sum_{\substack{l=0.q>0}}^{q-1} H^l_z \big|_{i,j+\frac{1}{2},k-\frac{1}{2}}.
\end{aligned}
\tag{45}
$$

In (31), $E^q_{y\,i,j+\frac{1}{2},k}$ has a relationship with the adjacent 12 electric fields. Equations for the electric fields in the x and z directions can be derived in a similar fashion. In (31), the magnetic fields are known because their orders are lower than those of the electric fields. Therefore, equations for the electric fields can be written as a matrix equation as follows:

$$[A]\{E^q\} = \{J^q\} + \{\beta^{q-1}\}, q = 0,1,2, \ldots, \tag{46}$$

where

$$\{E^q\} = \left\{E_x^q, E_y^q, E_z^q\right\}^T, \tag{47}$$

$$\{J^q\} = \left\{J_x^q, J_y^q, J_z^q\right\}^T. \tag{48}$$

In (46), $\{\beta^{q-1}\}$ is the summation term from order 0 to $q - 1$. In addition, $\{J^q\}$ represents the excitation current source, which is a known vector. Therefore, the Laguerre coefficients for the electric fields $\{E^q\}$ can be calculated recursively using (46) from order $q = 0$.

Contrary to the conventional FDTD method, the Laguerre-FDTD has an implicit relationship between the field variables, which results in a sparse system matrix $[A]$. This system matrix $[A]$ is independent of the order q of the temporal-testing function $\varphi_p(\bar{t})$. Therefore, after the LU decomposition of $[A]$ is performed at the beginning of the computations, (46) can be solved by using the back-substitution routine repeatedly.

By using the Laguerre basis functions which decay as $t \rightarrow \infty$, the stability is no longer affected by the time-step size. The time step is used only to calculate the Laguerre coefficients of the excitation in (22) at the beginning of the computations. Therefore, choosing a small time step does not increase the compute time.

3.1.3 Choice of the Number of Temporal Basis Functions

The method to choose the number of basis functions introduced in [24] is explained in this section. Consider a real time-domain signal $P(t)$ which is defined over the range [0, T_f] and is band-limited up to a frequency B. $P(t)$ can be represented by a Fourier series as follows:

$$P(t) = \sum_u C_u e^{ju\omega_0 t}, \tag{49}$$

where $\omega_0 = \frac{2\pi}{T_f}$. Since $P(t)$ is real, $C_u^* = C_{-u}$ where * means conjugate transpose. If $P(t)$ is band-limited to B Hz, then the value of u can be fixed by

$$-B \leq \frac{u}{T_f} \leq B. \tag{50}$$

Therefore, we have

$$P(t) = \sum_{u=-BT_f}^{BT_f} C_u e^{ju\omega_0 t}. \tag{51}$$

In (57), there are $2BT_f+1$ terms in the expansion of $P(t)$. From this, [24] concludes that at least $2BT_f+1$ terms of the Laguerre series are required to completely characterize the time-domain waveform of duration T_f and bandwidth $2B$, irrespective of its shape.

3.1.4 Calculation of Electric and Magnetic Fields in Time Domain

By solving (46) recursively, the coefficients of each Laguerre basis function can be obtained, which are the expansion coefficients of the electric and magnetic fields. From (12)-(14), we obtain

$$E_y\Big|_{i,j+\frac{1}{2},k}(t) = \sum_{p=0}^{2BT_f+1} E_y^p\Big|_{i,j+\frac{1}{2},k}\varphi_p(\bar{t}), \tag{52}$$

$$H_x\Big|_{i,j+\frac{1}{2},k+\frac{1}{2}}(t) = \sum_{p=0}^{2BT_f+1} H_x^p\Big|_{i,j+\frac{1}{2},k+\frac{1}{2}}\varphi_p(\bar{t}), \tag{53}$$

$$H_z\Big|_{i+\frac{1}{2},j+\frac{1}{2},k}(t) = \sum_{p=0}^{2BT_f+1} H_z^p\Big|_{i+\frac{1}{2},j+\frac{1}{2},k}\varphi_p(\bar{t}). \tag{54}$$

As shown in Figure 6, the Laguerre basis functions $\varphi_p(\bar{t})$ decays to zero as $\bar{t} \to \infty$. Therefore, the electric and magnetic fields obtained from (52)-(54) also decay to zero as $\bar{t} \to \infty$.

3.2 The SLeEC Algorithm

Since the introduction of the Laguerre-FDTD methodin [24], several modifications have been made to the algorithm for enhancing its performance [2]. In [2], an equivalent-circuit model of the FDTD grid has been developed. This method has been applied to both electromagnetic and circuit problems consisting of inductors, resistors and capacitors in [26]. The modified algorithm has been named SLeEC which stands for "Simulation using Laguerre Equivalent Circuit."

The following modifications and additions to the original Laguerre-FDTD scheme have been made in the SLeEC algorithm [27].

1. The limited time duration for which Laguerre-FDTD could be simulated has been resolved, so that Laguerre-FDTD can be done for all time duration (to capture the fast and slow transients up to DC).

2. The companion model for the FDTD grid has been developed, making the implementation easier without the use of long cumbersome equations.

3. A numerical method by which the correct number of basis coefficients is chosen has been proposed to obtain maximum accuracy.

4. A node numbering scheme for optimal memory efficiency has been suggested.

Each of these modifications is explained in detail in the following sections.

3.2.1   Simulation for Long Time Duration

A major drawback of the Laguerre-FDTD in [24] is that the transient simulation can be performed only for a limited time duration. The reason is the difficulty in the calculation of the Laguerre basis functions for long time and high order, which will be explained in detail in CHAPTER V.

In the SLeEC method, the limitation is overcome by dividing the total simulation time into different intervals [2]. Let Interval 1 span from time $t = t_0$ to $t = t_1$, Interval 2 span from time $t =$

t_1 to $t = t_2$, and so on, as shown in Figure 9. The length of each interval is chosen such that simulation can be accurately performed in the time duration. The final values at the end of Interval i are used as initial conditions to simulate in Interval $(i + 1)$. This process is repeated until the time duration for which the simulation needs to be done is completed. The companion models for FDTD simulation include initial conditions to enable restarting a simulation, which will be shown in the following subsection. The differential equations that describe the transient behavior of a system have been modified to explicitly include initial conditions that will permit simulation for all time duration. The SLeEC algorithm is applied in each of the time intervals.
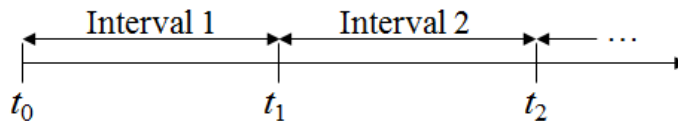
Figure 9. The total simulation time divided into different intervals.

3.2.2 Equivalent-Circuit Model Representation of the FDTD Grid

The Laguerre-FDTD approach requires solving a system of linear equations of the form $Ax = b$ to obtain the unknown Laguerre basis coefficients. In the SLeEC method, the linear equations on FDTD grid are replaced by equivalent companion models composed of resistors, voltage-controlled current sources and independent current sources. The equivalent-circuit models enable the use of the stamping rule [28] used in modified nodal analysis [29] to generate and solve the matrix equation, thereby making the implementation easier [30]. Spice [31] simulators, in general, use the modified-nodal-analysis method for simulation. Therefore, the SLeEC method can be seamlessly integrated into Spice for transient EM simulations using Laguerre polynomials.

In the Laguerre-FDTD method, Maxwell's differential equations of the FDTD grid are converted into the Laguerre domain as shown in the previous section. Figure 10 and Figure 11

25

show the standard FDTD Yee cell [11] and the cross sections of the FDTD cell at the locations marked by the dotted lines in Figure 10, respectively.
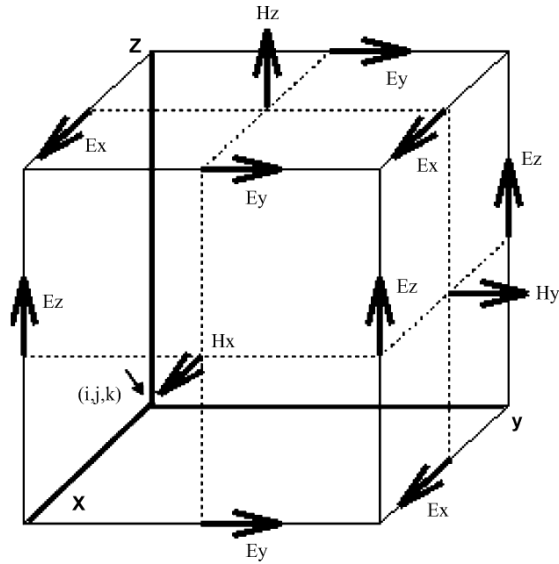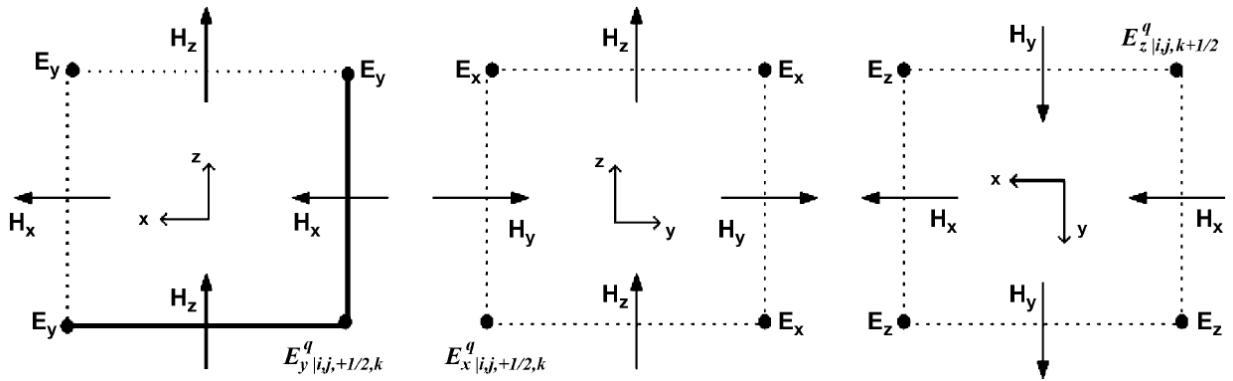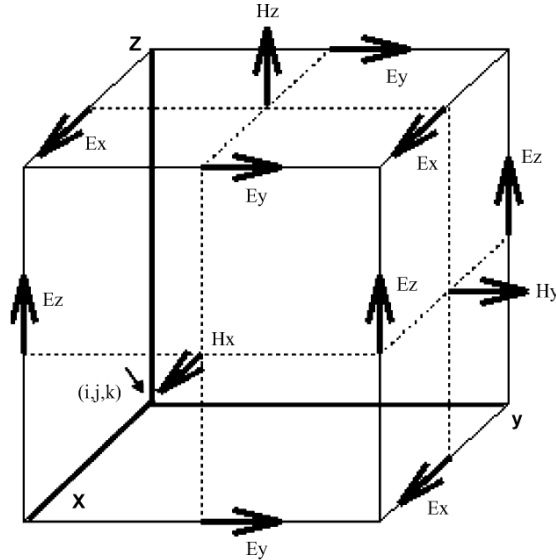

Figure 10. Standard Yee cell.
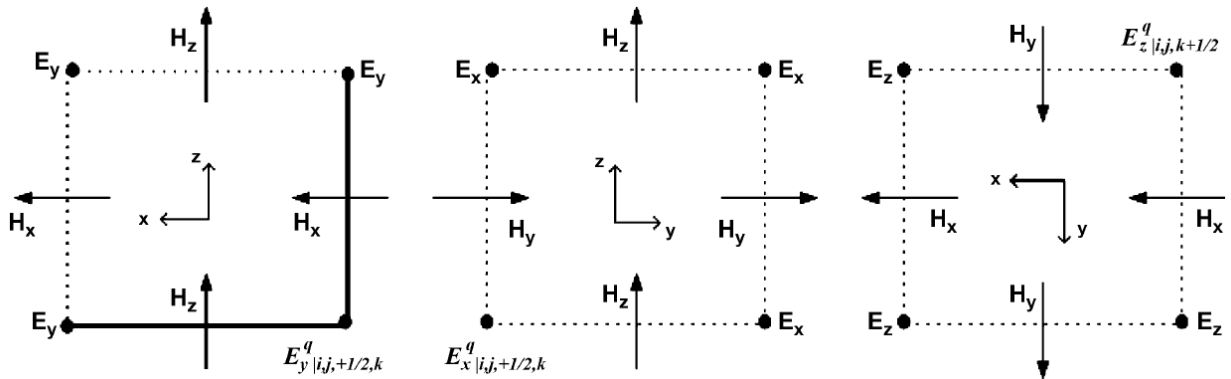
Figure 11. Sections of the Yee cell marked by the dotted lines in Figure 10 parallel to the *xz*, *yz*, and *xy* planes, respectively. Dots indicate direction of the fields pointing out of the page.

The Laguerre-domain representations of two of six Maxwell's differential equations of FDTD grid are shown in the following:

$$H_{z}^{q}\Big|_{i+\frac{1}{2},j+\frac{1}{2},k} - 2H_{z}^{init}\Big|_{i+\frac{1}{2},j+\frac{1}{2},k}$$

$$= -C_{x}^{H}\Big|_{i,j,k}\left(E_{y}^{q}\Big|_{i+1,j+\frac{1}{2},k} - E_{y}^{q}\Big|_{i,j+\frac{1}{2},k}\right)$$

$$+ C_{y}^{H}\Big|_{i,j,k}\left(E_{x}^{q}\Big|_{i+\frac{1}{2},j+1,k} - E_{x}^{q}\Big|_{i+\frac{1}{2},j,k}\right) \tag{55}$$

$$- 2\sum_{k=0,q>0}^{q-1} H_{z}^{k}\Big|_{i+\frac{1}{2},j+\frac{1}{2},k'}$$

$$E_{y}^{q}\Big|_{i,j+\frac{1}{2},k} - 2E_{y}^{init}\Big|_{i,j+\frac{1}{2},k}$$

$$= -C_{x}^{E}\Big|_{i,j,k}\left(H_{z}^{q}\Big|_{i+\frac{1}{2},j+\frac{1}{2},k} - H_{z}^{q}\Big|_{i-\frac{1}{2},j+\frac{1}{2},k}\right)$$

$$+ C_{z}^{E}\Big|_{i,j,k}\left(H_{x}^{q}\Big|_{i,j+\frac{1}{2},k+\frac{1}{2}} - H_{x}^{q}\Big|_{i,j+\frac{1}{2},k-\frac{1}{2}}\right) \tag{56}$$

$$- \frac{2}{s\varepsilon}J_{y}^{q}\Big|_{i,j+\frac{1}{2},k} - 2\sum_{k=0,q>0}^{q-1} E_{y}^{k}\Big|_{i,j+\frac{1}{2},k'}$$

where

$$C_{x}^{E}\Big|_{i,j,k} = \frac{2}{s\varepsilon_{i,j,k}\Delta x_{i}}, \tag{57}$$

$$C_{y}^{E}\Big|_{i,j,k} = \frac{2}{s\varepsilon_{i,j,k}\Delta y_{i}}, \tag{58}$$

$$C_{x}^{H}\Big|_{i,j,k} = \frac{2}{s\mu_{i,j,k}\Delta x_{i}}, \tag{59}$$

$$C_{y}^{H}\Big|_{i,j,k} = \frac{2}{s\mu_{i,j,k}\Delta y_{i}}. \tag{60}$$

Note that the initial conditions are explicitly included in (55) and (56) to enable restarting a simulation beyond a certain time duration, as explained in the previous subsection. Equations (55) and (56) can be represented in a circuit form as shown in Figure 12. Figure 12 represents the

27

circuit model for the magnetic field $H_z^q{}_{i+\frac{1}{2},j+\frac{1}{2},k}$ and the electric field $E_y^q{}_{i,j+\frac{1}{2},k}$ at the location

marked by the solid edges and their intersection in Figure 11. Only the partial 3-D model is

shown in Figure 12. The complete model can be derived in a similar fashion and is shown in

Appendix A.
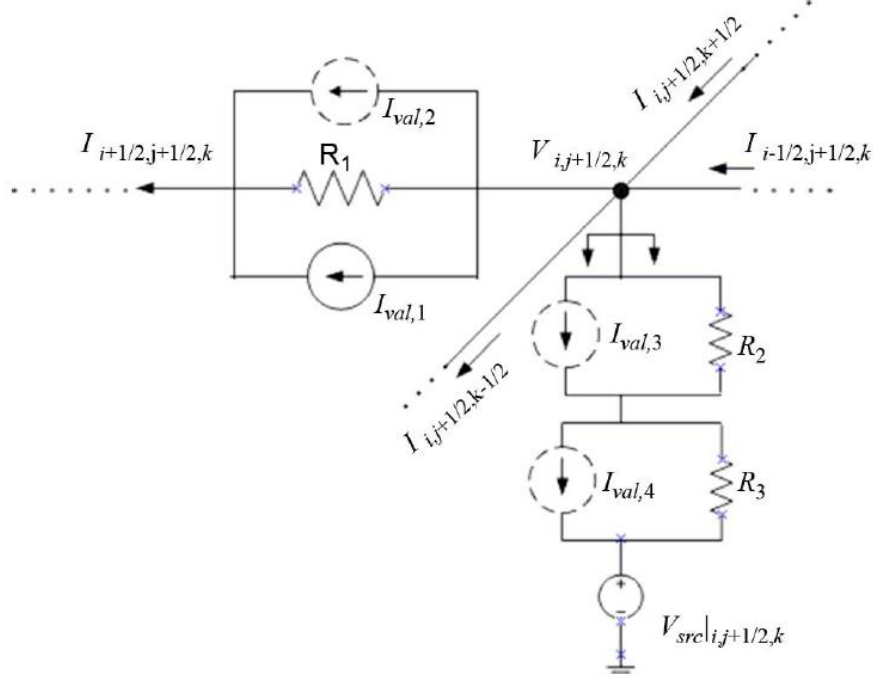
Figure 12. Companion model of the 3-D FDTD grid in Laguerre domain.

The branch currents represent the qth Laguerre basis coefficient of the magnetic fields and

are given by

$$H_z^q{}_{i+\frac{1}{2},j+\frac{1}{2},k} = I_{i+\frac{1}{2},j+\frac{1}{2},k},\tag{61}$$

$$H_z^q{}_{i-\frac{1}{2},j+\frac{1}{2},k} = I_{i-\frac{1}{2},j+\frac{1}{2},k},\tag{62}$$

$$H_x^q{}_{i,j+\frac{1}{2},j+\frac{1}{2}} = I_{i,j+\frac{1}{2},k+\frac{1}{2}},\tag{63}$$

28

$$H_x^q \Big|_{i,j+\frac{1}{2},k-\frac{1}{2}} = I_{i,j+\frac{1}{2},k-\frac{1}{2}}. \tag{64}$$

The nodal voltages represent the qth basis coefficient of the electric fields given by

$$E_y^q \Big|_{i,j+\frac{1}{2},k} = V_{i,j+\frac{1}{2},k}. \tag{65}$$

In Figure 12, the branch-current circuitry represents (55) and the circuitry connected to the node with voltage $V_{i,j+\frac{1}{2},k}$ represents (56).

The values of the current sources and the resistor in the branch-current circuitry in Figure 12 are

$$I_{val,1} = 2H_z^{init} \Big|_{i+\frac{1}{2},j+\frac{1}{2},k} - 2\sum_{k=0,q>0}^{q-1} H_z^k \Big|_{i+\frac{1}{2},j+\frac{1}{2},k}, \tag{66}$$

$$I_{val,2} = C_y^H \left(V_{i+\frac{1}{2},j+1,k} - V_{i+\frac{1}{2},j,k} \right), \tag{67}$$

$$R_1 = \frac{1}{C_x^H}. \tag{68}$$

The current sources and the resister connected between the ground and the node with voltage $V_{i,j+\frac{1}{2},k}$ in Figure 12 have the following values:

$$I_{val,3} = I_{i,j+\frac{1}{2},k+\frac{1}{2}} - I_{i,j+\frac{1}{2},k-\frac{1}{2}}, \tag{69}$$

$$I_{val,4} = I_{i-\frac{1}{2},j+\frac{1}{2},k} - I_{i+\frac{1}{2},j+\frac{1}{2},k}, \tag{70}$$

$$R_2 = C_x^E, \tag{71}$$

$$R_3 = C_z^E, \tag{72}$$

$$V_{src} \Big|_{i,j+\frac{1}{2},k} = 2E_y^{init} \Big|_{i,j+\frac{1}{2},k} - \frac{2}{s\varepsilon} J_y^q \Big|_{i,j+\frac{1}{2},k} - 2\sum_{k=0,q>0}^{q-1} E_y^k \Big|_{i,j+\frac{1}{2},k}. \tag{73}$$

The circuit given in Figure 12 can be stamped in a modified-nodal-analysis matrix [29] and solved to find the unknown Laguerre basis coefficients of the electric and magnetic fields.

Solving the circuit shown in Figure 12 in the SLeEC method is equivalent to solving (46) in the Laguerre-FDTD algorithm. In the Laguerre-FDTD algorithm, the recursive calculations of (46) are needed as the order q increases. In the SLeEC method, the recursive calculations in the Laguerre-FDTD approach are realized by obtaining DC solutions of the equivalent-circuit model for each order q as the order q increases. The DC solution at the end of the qth iteration represents the qth Laguerre basis coefficient of the electric and the magnetic fields. The DC solution at the end of the qth iteration is used to update the companion model before solving for the next set of Laguerre basis coefficients. The number of unknowns that needs to be solved in the DC analysis can be reduced by using the Norton equivalent form [27] looking into the circuit marked by the double arrow in Figure 12. The values of the Norton equivalent circuit are given by

$$I_N = \frac{-I_{val,3}R_2 + V_{src} - I_{val,4}R_3}{R_2 + R_3},$$
(74)

$$R_N = R_2 + R_3.$$
(75)

In (74), I_N has terms involving $I_{val,3}$ and $I_{val,4}$. Therefore, I_N is a current-controlled current source. In the modified nodal analysis [29], current-controlled current-source terms in I_N introduce additional unknowns, besides the unknown nodal voltages [30]. However, I_N can be implemented as a voltage-controlled current source and independent current source, by stamping the current in a branch directly with the additional unknowns being eliminated. Voltage-controlled current sources do *not* introduce additional unknowns [30]. The unknowns to be solved are only the electric-field coefficients (nodal voltages). Therefore, the matrix dimension to be solved is in its optimal form.

The partial model shown in Figure 12 can be extended in a similar fashion to satisfy the complete set of Maxwell's differential equations in 3-D form in the Laguerre domain.

3.2.3 Choosing the Correct Number of Basis Functions

The final step of the Laguerre-FDTD is to convert the Laguerre-domain coefficients to time-domain parameters at the output nodes of interest. Here, the number of basis functions used in generating the time-domain waveform is very important to obtain accurate results because of the time-domain waveform's sensitivity to the number of basis functions. A Fourier-transform-based method to choose the number of basis functions in the Laguerre-FDTD is proposed in [24], which is shown in detail in 3.2.3. However, the method only provides the minimum number of basis functions and misses maximizing accuracy. The methodology for choosing the optimal number of basis coefficients is improved in the SLeEC method to maximize the accuracy [32], which is explained below.

1)   Energy analysis (Step 1): Laguerre basis functions decay to 0 as time increases, as shown in Figure 6, and decay slower as the order of Laguerre basis function increases. Thus, for the later part of a time-domain waveform, which is computed as the sum of weighted Laguerre basis functions, the number of basis function needs to be sufficiently large. The minimum number of basis functions q_{knee} to represent a time-domain waveform can be found by analyzing the time-domain waveform's energy content as a function of the number of basis functions.

Energy content $E(q)$ is defined as a summation of the L^1 norm:

$$E(q) = \sum_{i=0}^{N} |W_q[i]|, \tag{76}$$

where W_q is the time-domain waveform obtained using $q+1$ basis coefficients, and N is the number of discrete time points making up the time-domain waveform.

The energy content as a function of the number of basis functions is shown in Figure 13. When the number of basis function is larger than 100, those basis functions have

31

constant energy content. Therefore, $q_{knee} = 100$ is considered as the minimum number of basis functions to have sufficient energy to represent the time-domain waveform for the time duration of interest.
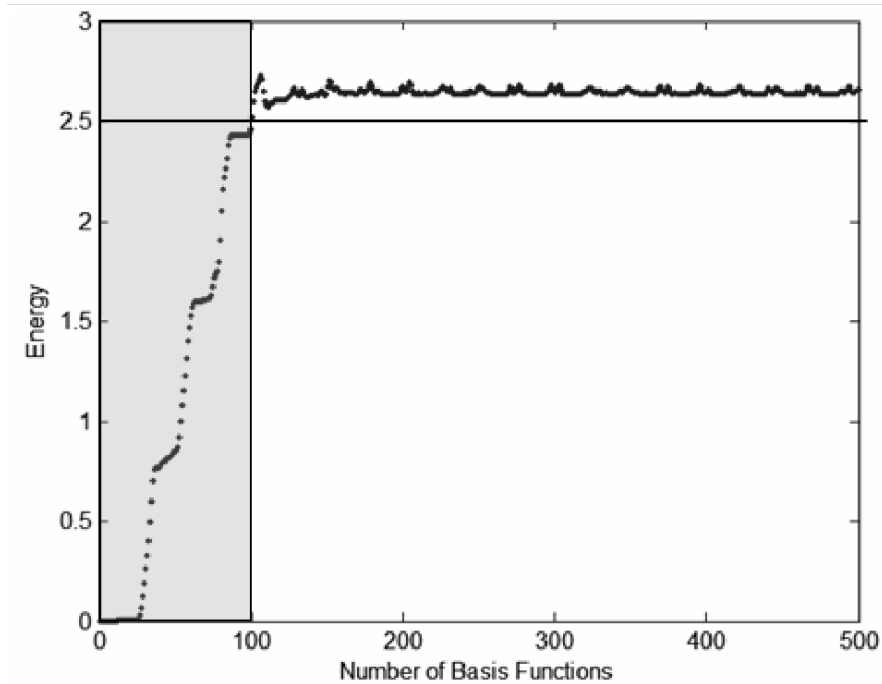
Figure 13. Energy content as a function of the number of basis functions.

2)   Finding the optimal number of basis functions (Step 2): Given the minimum number of basis functions from Step 1, the correct number of basis functions which maximizes the accuracy can be chosen by doing an error analysis. Using more Laguerre basis functions does not always improve accuracy, which is explained in detail in CHAPTER IV. Since the Laguerre basis function's value equals 1 at time $t = 0$ regardless of the basis function's order, minimizing the error at time $t = 0$ is sufficient to determine the exact number of basis coefficients. The optimal number of basis functions q_{opt} is chosen between $\{q_{knee}, \ldots, q_{max}\}$ in order to produce the smallest error at time $t = 0$. By using a source waveform with initial value zero, the field values at all locations also

have the value zero at time $t = 0$. By starting the simulation in a known state, the initial value is therefore known and can be used to minimize error at time $t = 0$.

Although this methodology for transformation from Laguerre domain to time domain provides guidance in determining the number of basis functions, it still has limitations such as spurious oscillations similar to Gibb's phenomena in the Fourier series. The methodology for obtaining the time-domain waveform has been improved in this dissertation as compared to prior work [32]. The efficient recovery of the time-domain waveform using a reduced number of basis coefficients with an increased accuracy level is in detail in CHAPTER IV.

3.2.4 Node-Numbering Scheme

The SLeEC method requires solving a matrix of the form $Ax=b$ at every iteration. However, LU decomposition has to be done only once because the matrix stays constant throughout the iterations. The matrix is sparse and symmetric. To make the matrix banded, the nodes are numbered on a cell by cell basis.

Let us assume that the problem domain consists of $nx \times ny \times nz$ cells where the label for the ith Yee cell in the jth row on kth plane can be written as cell (ijk), as shown in Figure 14.

The nodes within a cell (000) at the corner are numbered first, and the nodes within an adjacent cell in x direction, cell (100), are labeled next. In the case of the shared nodes between cell (000) and cell (100), since all nodes within cell (000) are numbered prior to the numbering of the nodes within cell (100), the shared nodes are skipped in the numbering of the nodes within cell (100). Next, the nodes within the cell (200) are numbered in a similar fashion, and the numbering scheme continues until it reaches cell (nx00). This numbering process is repeated for the nodes within cells on other rows and planes, leading to the numbering of all the nodes that define the structure.

Because of the local behavior of Maxwell's equations in a Yee cell, this form of node numbering can lead to the *A* matrix being banded, as shown in Figure 15.
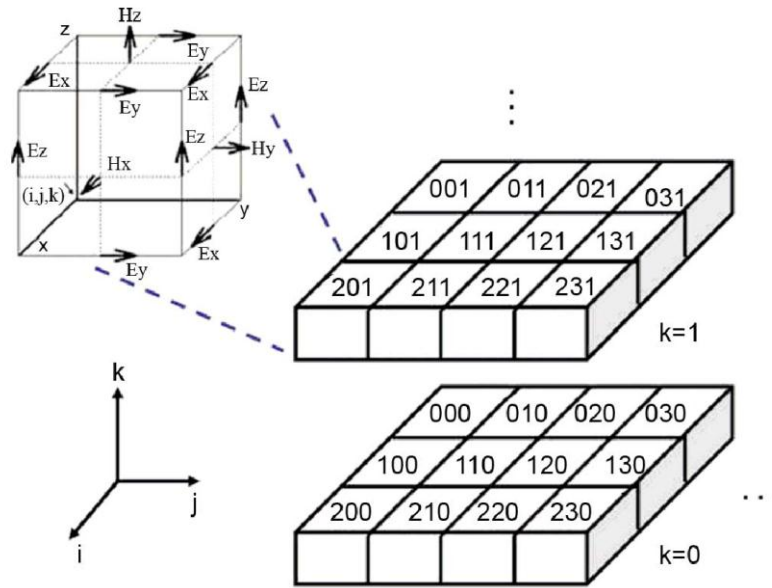
Figure 14. Efficient node-numbering scheme.
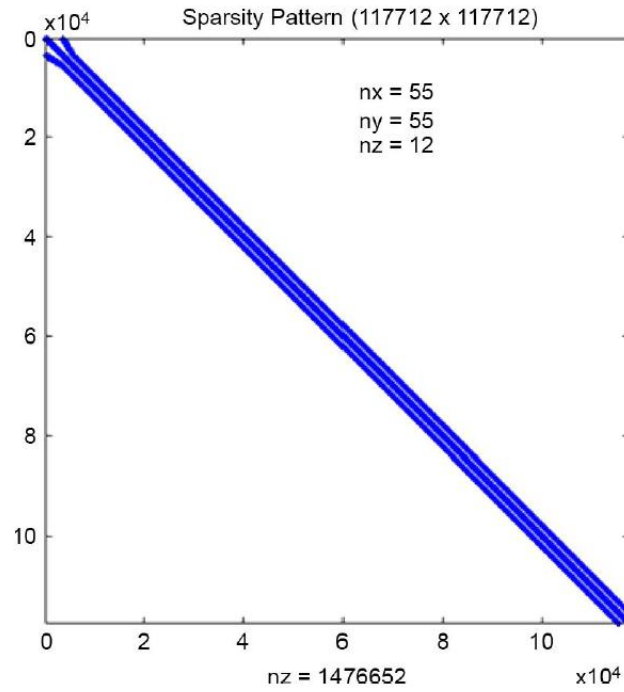
Figure 15. Sparsity pattern of the *A* matrix suitable for LU decomposition.

3.3 Advantages of using Laguerre Polynomials

Orthogonal polynomials are classes of polynomials $\{p_n(x)\}$ defined over a range $[a, b]$ that obey an orthogonality relationship in the form

$$\int_a^b w(x)p_m(x)p_n(x)dx = \delta_{mn}c_n, \tag{77}$$

where $w(x)$ is a weighting function and δ_{mn} is the Kronecker delta. A table of some orthogonal polynomials is given in Table 1, where $w(x)$ is the weighting function.

Table 1. Selected orthogonal polynomials.

Polynomial	Interval	$w(x)$
Chebyshev polynomial of the first kind	[-1, 1]	$(1-x^2)^{-1/2}$
Chebyshev polynomial of the second kind	[-1, 1]	$(1-x^2)^{1/2}$
Gegenbauer polynomial	[-1, 1]	$(1-x^2)^{\alpha-1/2}$
Hermite polynomial	$[-\infty,\infty]$	e^{-x^2}
Jacobi polynomial	(-1, 1)	$(1-x)^\alpha(1+x)^\beta$
Laguerre polynomial	$[0, \infty]$	e^{-x}
Legendre polynomial	[-1, 1]	1

There are several reasons why Laguerre polynomials are attractive as compared to other orthogonal polynomials, which are described below:

1. Laguerre polynomials are defined in the interval of $[0,\infty]$, which is suitable for transient simulation because it is easy to enforce the initial condition at time $t = 0$.

2. By having an exponential function as its weighting function, transient simulation using Laguerre polynomials is unconditionally stable since the amplitude of the functions decays with time.

3. When solving for N Laguerre basis coefficients $\{W_0, W_1, \ldots, W_{N-1}\}$, the dimension of the matrix to be solved is independent of N since the coefficients are calculated recursively depending only on the previous order's coefficients. In contrast, when other orthogonal polynomials are used, the formulations are not given in the recursive form.

3.4 Summary

An unconditionally stable implicit-FDTD scheme using Laguerre polynomials has been proposed, which is referred to as the Laguerre-FDTD scheme. Laguerre-FDTD can be significantly faster than FDTD and other time-domain methods especially for packaging problems containing multiscale dimensions. By using an implicit-solution technique, a decrease in simulation time is possible at the expense of an increase in memory consumption. Most importantly, because of Laguerre-FDTD's unconditional stability, the time-step limitation can be removed. Since Laguerre-FDTD is a marching-on-in-time scheme, a time step larger than Courant-Friedrich-Levy (CFL) limit does not deteriorate the accuracy of the simulation.

Since the introduction of the Laguerre-FDTD algorithm, several modifications have been made to the algorithm for enhancing its performance. The modified algorithm has been named SLeEC which stands for "Simulation using Laguerre Equivalent Circuit," which uses an equivalent-circuit model of the FDTD grid in the simulation. The SLeEC method enables the transient simulation for a long time interval which has been difficult using the Laguerre-FDTD scheme described earlier by other researchers. Also, the SLeEC method can be seamlessly integrated into Spice simulators by using the equivalent-circuit models. In addition, the SLeEC method provides the methodology for choosing the correct number of basis functions for maximizing accuracy, and uses a node-numbering scheme that enables efficient LU decomposition of the system matrix.

CHAPTER IV

GENERATING THE TIME-DOMAIN WAVEFORM FROM LIMITED

NUMBER OF LAGUERRE BASIS COEFFICIENTS

As stated earlier, in the Laguerre-FDTD method, a time-domain problem is rewritten and solved in the Laguerre-domain. Since it is impossible to use an infinite number of Laguerre basis functions in the calculation, an approximation with a finite number of Laguerre basis functions is needed for accurate and efficient simulation.

4.1 Limitations of Prior Work

A Fourier-transform-based method to choose the number of basis functions in the Laguerre-FDTD is proposed in [24], which is shown in detail in 3.2.3. However, the method only provides the minimum number of basis functions and misses maximizing accuracy. To improve the method to choose the number of basis functions, the SLeEC method proposed two steps to choose the optimal number of basis functions [32], which is discussed in CHAPTER III in detail. The first step is to calculate the energy contained in the time-domain waveform. The energy is defined as a summation of the L^1 norm. By analyzing the energy, the lower bound of the number of basis functions can be found, which has enough energy to represent the time-domain waveform for the desired time duration. The second step is to analyze error at the initial point (in general, time $t = 0$) and choose the number of basis functions that gives the minimum error at the initial point. The error at the initial point provides the statistical upper bound of error over the whole simulated time duration as shown in Appendix B. However, the proposed method in [32] does not guarantee the minimum error over the whole simulated time duration.

For example, for the given time-domain waveform shown in Figure 16, the energy analysis (first step) shows that the number of basis function needs to be more than 100 as shown in Figure

17. Errors at time $t = 0$ are plotted with respect to the number of basis functions as shown in Figure 18. Based on the error analysis, the SLeEC methodology picks 162, which generates the smallest error at time $t = 0$, as the optimal number of basis functions, resulting in the recovered time-domain waveform shown in Figure 19. Compared to the original time-domain waveform, 162 basis functions seem to produce an accurate waveform.
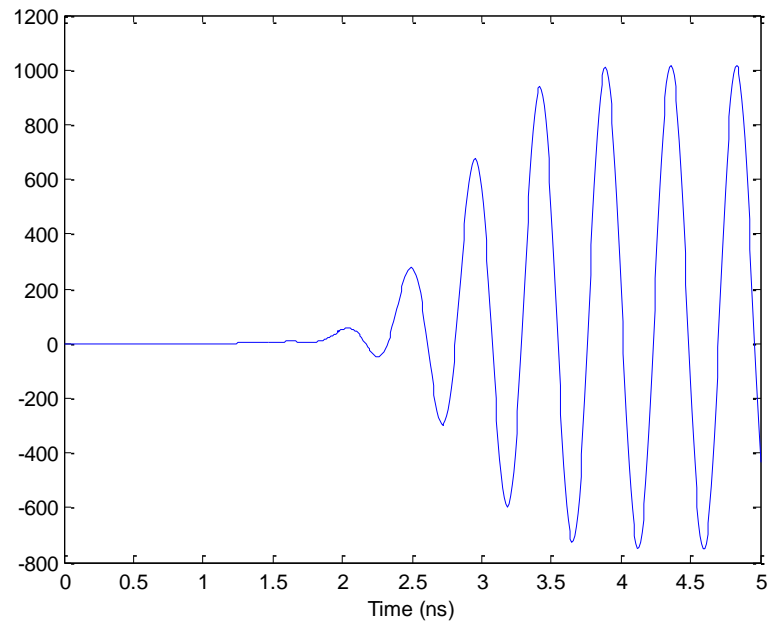
Figure 16. Example time-domain waveform to be recovered using Laguerree basis functions.
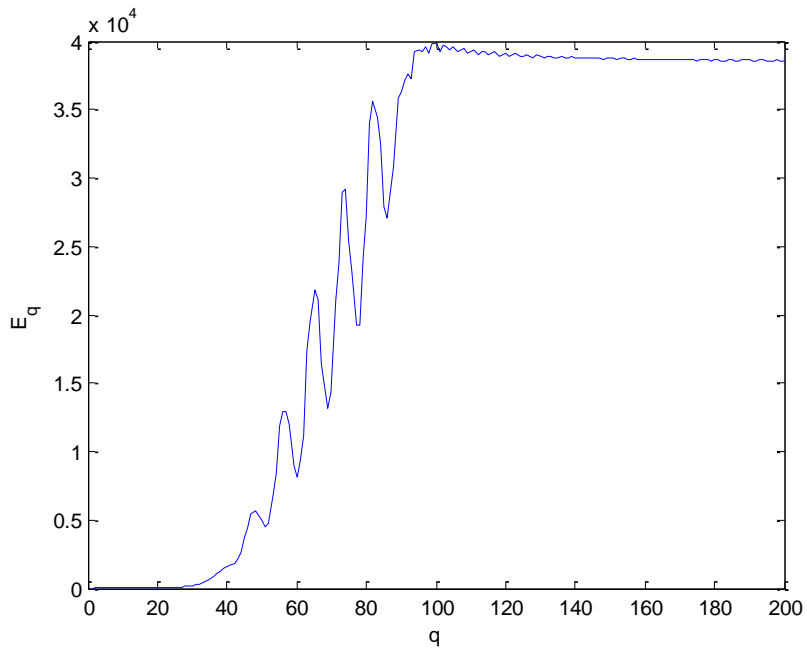
Figure 17. Energy content of the recovered waveform as a function of the number of basis functions.
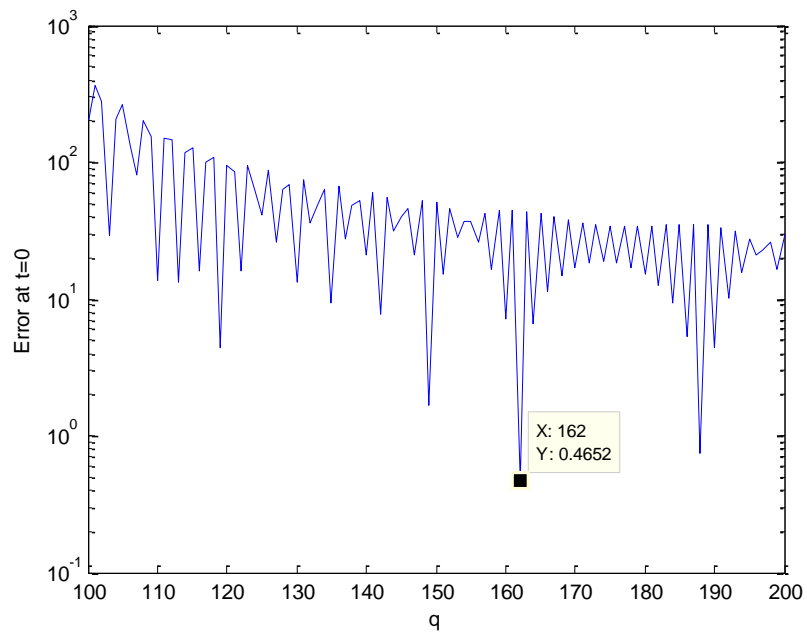
Figure 18. Error at $t = 0$ as a function of the number of basis functions.

40
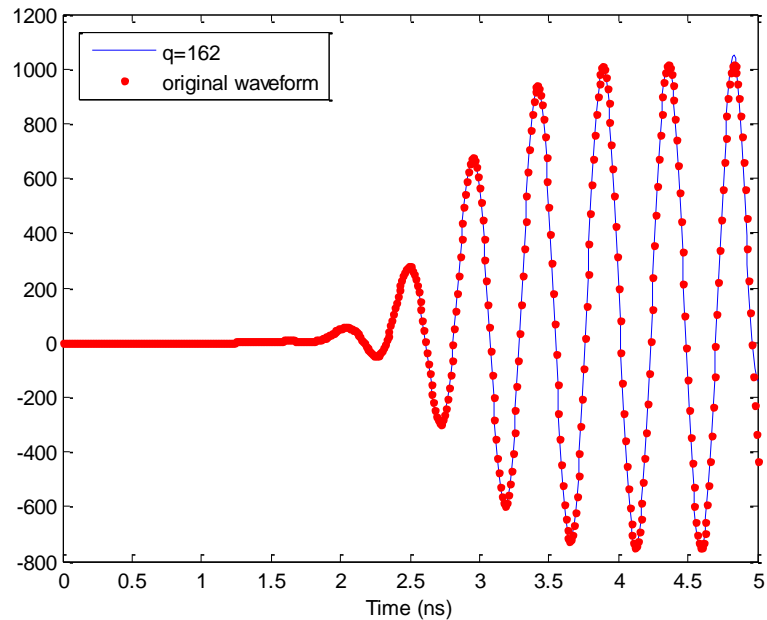
Figure 19. Recovered time-domain waveform using 162 basis functions compared with original waveform.

4.1.1 One Optimal Number of Basis Functions for Multiple Time Points

However, good correlation between the recovered waveform using 162 basis functions and the original waveform does not necessarily mean that 162 is the optimal number of basis functions in terms of accuracy. A recovered waveform using 188 basis functions is considered for comparison. At time $t = 4.6$ *ns*, the waveform using 162 shows better accuracy than one using 188 basis functions as shown in Figure 20. However, at time $t = 4.35$ *ns*, the use of 188 basis functions produces a closer value to the original waveform than the use of 162 basis functions, as shown in Figure 21, which means that the optimal number of basis function can be different at each time point.

41
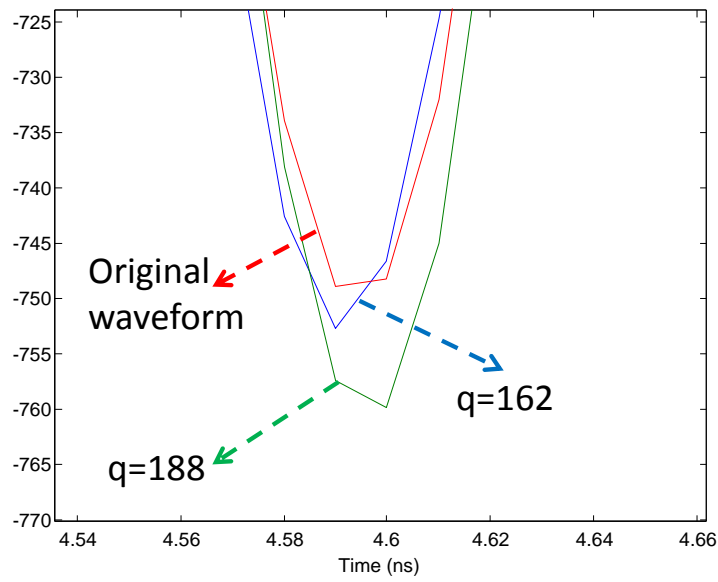
Figure 20. Comparison of the recovered time-domain waveforms near *t* = 4.6 *ns.*
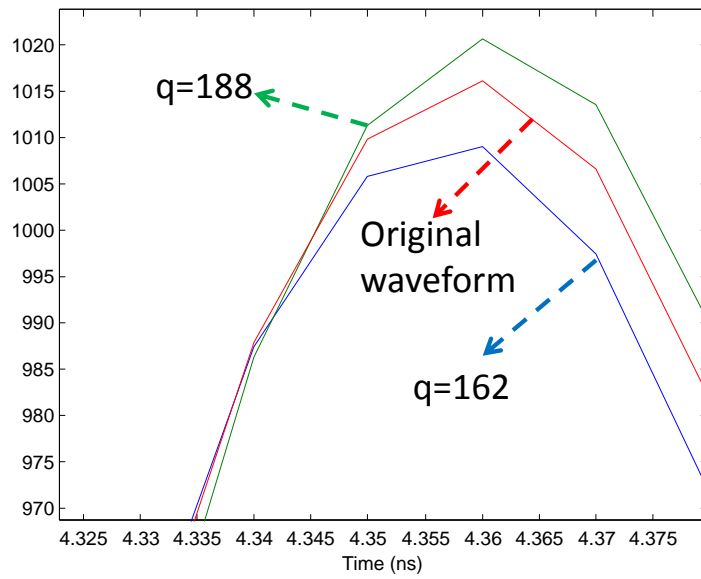
Figure 21. Comparison of the recovered time-domain waveforms near *t* = 4.35 *ns.*

4.1.2 Spurious Oscillations

In addition, a recovered time-domain waveform has spurious oscillations in early time and near sharp transitions as shown in Figure 22.
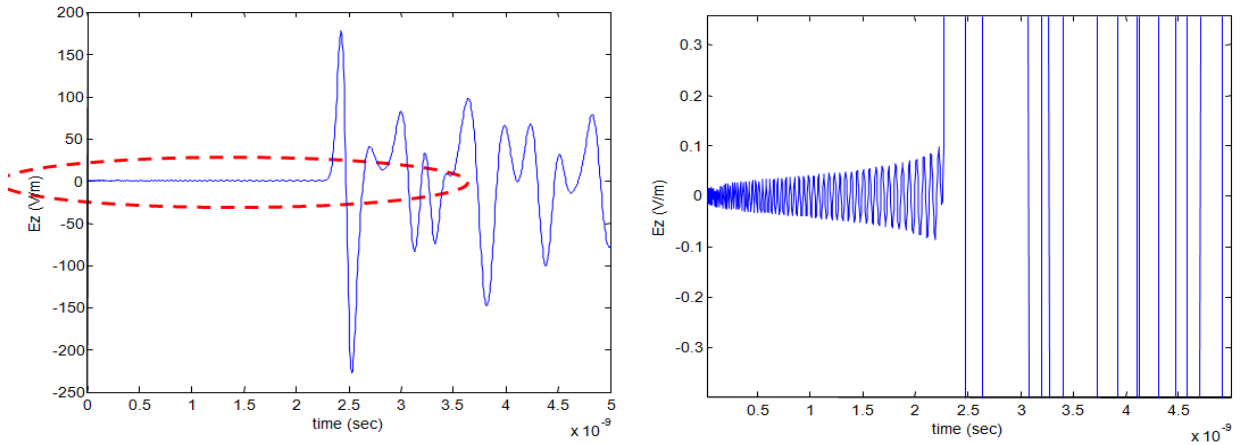
Figure 22. Spurious oscillations.
(Left: Recovered time-domain waveform, right: magnified view of the circled area)

To qualitatively analysis the spurious oscillations, the step function shown in is considered as an example.
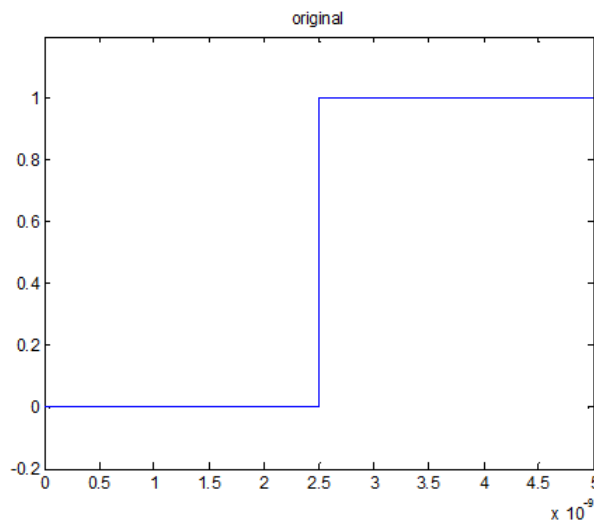
Figure 23. Example waveform to recover

The waveform shown in Figure 23 is recovered using 50, 500, 5000, and 50000 basis functions with the time scale factor $s = 1e10$, as shown in Figure 24, Figure 25, and Figure 26, respectively.
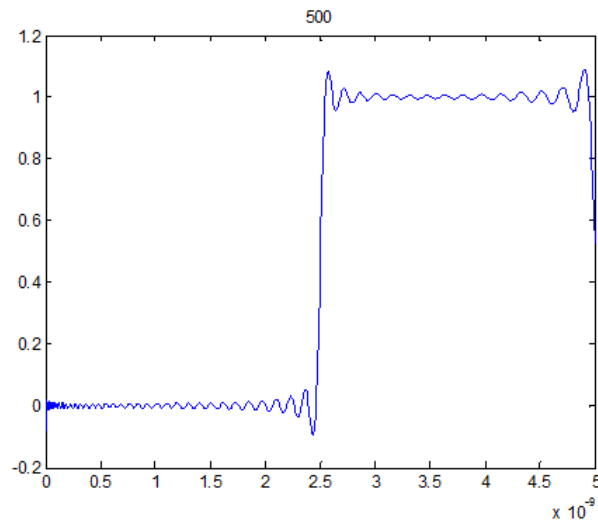
Figure 24. Recovered waveform using 500 basis functions.
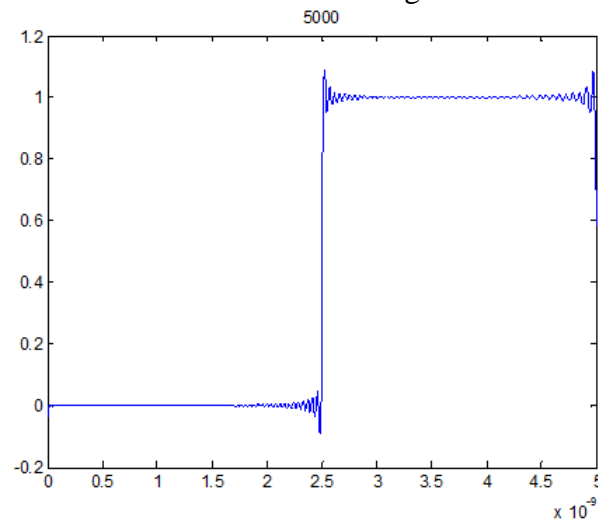
Figure 25. Recovered waveform using 5000 basis functions.
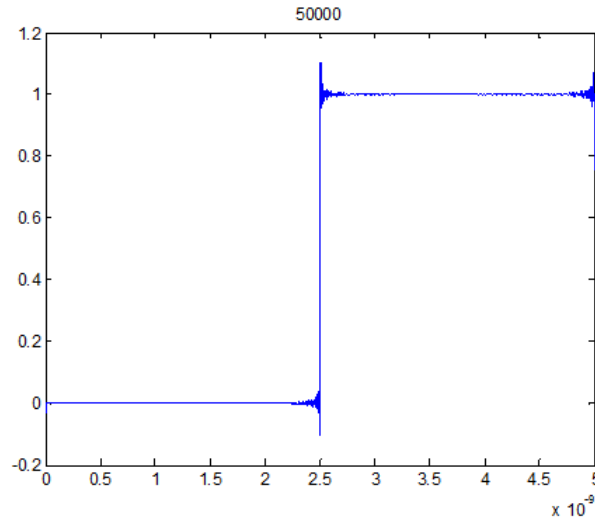
Figure 26. Recovered waveform using 50000 basis functions.

Figure 24, Figure 25, and Figure 26 show that the magnitude and frequency of spurious oscillations decreases and increases respectively as the number of basis functions increases. Such trend eliminates the probability that the spurious oscillations come from computational errors. Also, the trend is the same as Gibbs effect in Fourier series. It is worthwhile to note that error near the sharp transition point is not easily dampened just by increasing the number of basis functions. Quantitative analysis of the spurious oscillations is left for future work.

4.2 New Method for Obtaining Accurate Transient Waveform

As the number of basis functions goes to infinity, the approximated solution with the finite number of basis functions converges to its original solution. At a fixed time $t = t_{\text{fixed}}$, during the process of the time-domain solution converging to the original solution as the number of basis function increases, the solution fluctuates near the original solution with decaying magnitude of the fluctuation as shown in Figure 27. Therefore, the application of a low-pass filter to the converging process enhances the accuracy of the solution by removing the fluctuations. Also,

45

compared to the unfiltered case, low-pass filtering provides faster convergence to the original solution, resulting in a smaller number of basis functions to achieve the desired accuracy. The following infinite-impulse-response (IIR) filter is chosen to wipe out the fluctuations:

$$W(N, t) \cong \sum_{p=0}^{N} W_p \varphi_p(t), \tag{78}$$

$$W_1(N, t) = \sigma_1 W_1(N-1, t) + \frac{1}{1-\sigma_1} W(N, t), \tag{79}$$

$$W_2(N, t) = \sigma_2 W_2(N-1, t) + \frac{1}{1-\sigma_2} W_1(N, t). \tag{80}$$

where W is a raw waveform, W_1 is the intermediate waveform in the filtering, W_2 is the filtered solution, and σ_1 and σ_2 are related to the strength of the filtering whose values are between 0 and 1. Both σ_1 and σ_2 are empirically chosen to be 0.95 in the example in this chapter. As shown in Figure 28, the filtered solution converges more quickly and smoothly than the unfiltered solution without fluctuations.
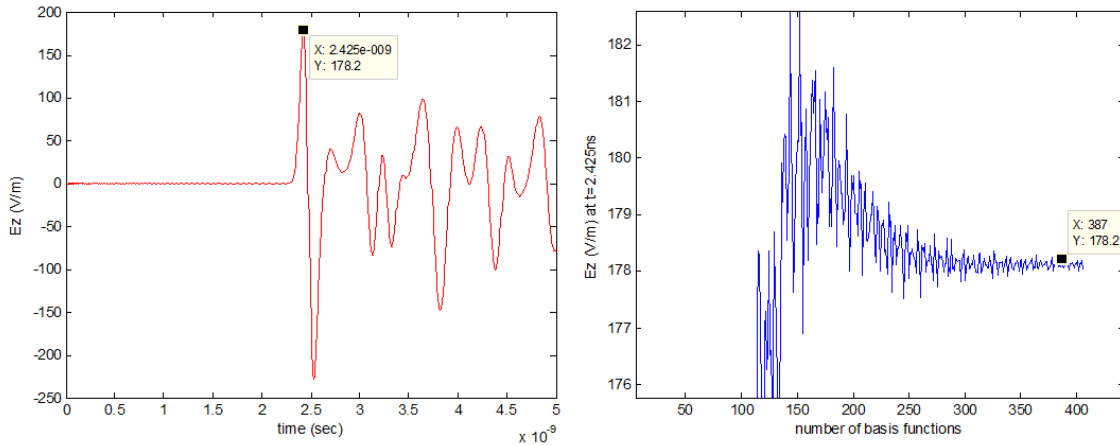
Figure 27. Converging trend. (Left: the time-domain solution, right: the time-domain solution at time t=2.425ns as function of the number of basis functions)

Since the filtered solution converges more quickly to the solution than the unfiltered solution, the number of basis functions required to ensure a certain level of accuracy can be significantly reduced. As the simulation run time is directly proportional to the number of basis

functions in the Laguerre-FDTD, the use of fewer basis functions results in reduced simulation time. On the other hand, by filtering the solution at each time point, error is minimized for the overall simulated time duration. Therefore, spurious oscillations in early time disappear as shown in Figure 29.
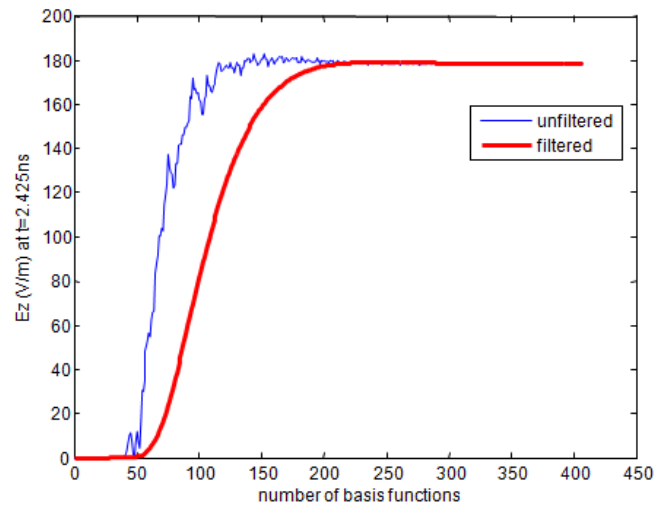
Figure 28. Convergence of the filtered solution.
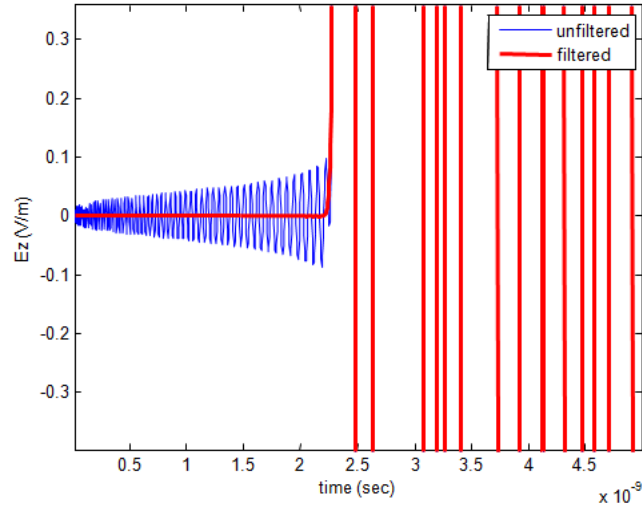
Figure 29. Removal of spurious oscillations by filtering.

4.3 Numerical Results

A bird's-eye view of the modeled structure is shown in Figure 30 (a). The on-chip structures along with the interface between the chip and the package are shown in Figure 30 (b). The magnified view of the region marked by the circle in Figure 30 (b) is shown in Figure 30 (c). The structure has on-chip interconnects in the metal layers M1 and M2, connected by vias and routed on the redistribution layer, through the solder pads, to the package and routed as package-level interconnects. The on-chip structures in Figure 30 (c) represent the interconnections in the M1 and M2 layers of an SRAM cell. A cross-sectional view of the structure is given in Figure 31.

One of the important features of the chip-package structure is the multiscale dimensions from the nanometer (*nm*) range to the millimeter (*mm*) range, resulting in a scale ratio of 1:50,000 in this example. The on-chip structures that are in the *nm* scale require a very fine mesh, and therefore the simulation time becomes prohibitively large using the conventional FDTD scheme because of the CFL condition. The time-domain response of the electric field at the

48

location marked by 'probe' in Figure 30 (a) up to 5 *ns* is computed. The modulated Gaussian current source is used to excite the structure at the end of the package trace as shown in Figure 30 (a).

The structure has been simulated using the conventional FDTD, Laguerre-FDTD method without filtering, and Laguerre-FDTD method with the proposed filtering method. The normal SLeEC scheme without filtering requires 502 Laguerre basis functions while the Laguerre-FDTD scheme with the proposed filtering process needs only 368 basis functions, which speeds up the simulation by 33%, from 9 minutes to 6 minutes. The simulation results show very good correlation between Laguerre-FDTD and FDTD as shown in Figure 32. Since the simulated waveforms from Laguerre-FDTD with and without filtering are overlapped, they are indistinguishable in the figure. Spurious oscillations in early time are suppressed by filtering as shown in Figure 33. While it takes 30 hours using FDTD, the Laguerre-FDTD method with the proposed filtering scheme in this chapter takes only 6 minutes to complete the simulation for the same structure with the same number of cells. This represents a $300\times$ speed up over the conventional FDTD scheme. The simulations were run on a Pentium quad core, 2.4GHz processor with 4GB RAM.
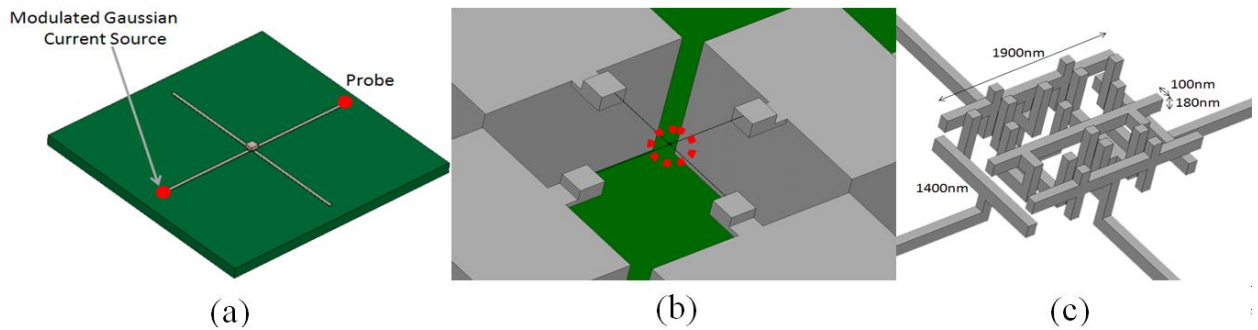
Figure 30. The bird's-eye view of a test chip-package structure.
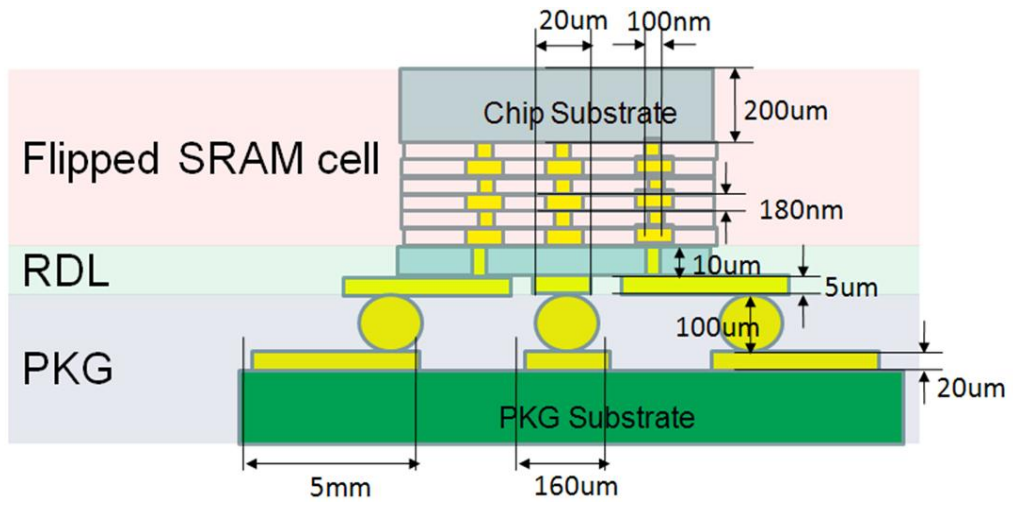
Figure 31. Cross section of the test structure.
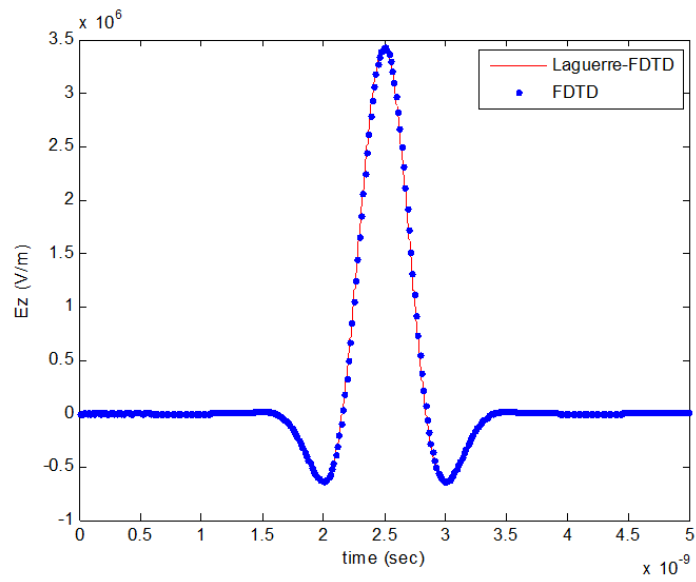
Figure 32. Simulated time-domain waveform using Laguerre-FDTD and FDTD.
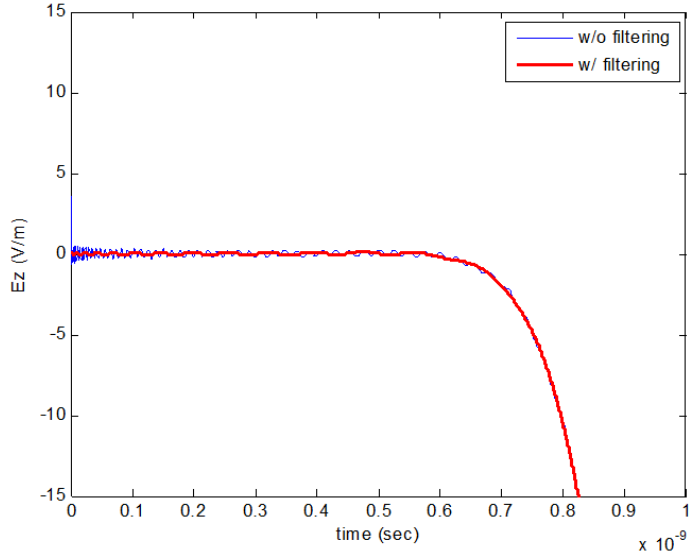
Figure 33. Reduction of spurious oscillations in early time.

4.4 Summary

In the Laguerre-FDTD approach, a time-domain problem is converted into the Laguerre-domain and solved in the Laguerre-domain. Since it is impossible to use an infinite number of Laguerre basis functions in the calculation, a proper approximation with a finite number of Laguerre basis functions is needed for the accuracy of the simulation. The SLeEC methodology provides a method to find the optimal number of basis functions. However, the resulting time-domain waveform is not globally optimal regarding the accuracy.

In this chapter, a method for maximizing the accuracy with the minimum number of basis functions has been proposed, which reduces the simulation running time and increases the accuracy of Laguerre-FDTD. The proposed method removes spurious oscillations in early time as well. The proposed method has been verified through a chip-package co-simulation example. The simulation result of the example shows that the transient simulation using the proposed method is 300 times faster than FDTD while maintaining the accuracy.

51

CHAPTER V

SIMULATION FOR LONG TIME DURATION

Due to the behavior of Laguerre polynomials, the Laguerre-FDTD method has a limitation on the maximum time duration over which the structure can be simulated [2]. Although the SLeEC scheme proposed in [2] overcomes such limitation on the maximum time duration by dividing total simulation time into different time intervals, it has a drawback that error is accumulated as the number of time intervals increases. Hence, obtaining the low frequency response using SLeEC is a challenge.

In this chapter, a method for simulating long time intervals using the Laguerre-FDTD scheme is presented that can be used to compute the low frequency response in addition to the high frequency response. The proposed method is applied to a multiscale structure example for verification.

5.1 Difficulty in Calculation of Laguerre Basis Functions

The first five Laguerre basis functions are plotted in Figure 34. Since the Laguerre basis function's fluctuation is too slow to describe the time-domain behavior of interest in the range of nanoseconds or microseconds, time t is transformed into a scaled time $\bar{t}$ using a time-scale factor s and $\bar{t}$ is used instead of t in the actual simulation:

$$\bar{t} = s \cdot t. \tag{81}$$

However, in this section, the use of the time-scale factor is omitted for simplicity.
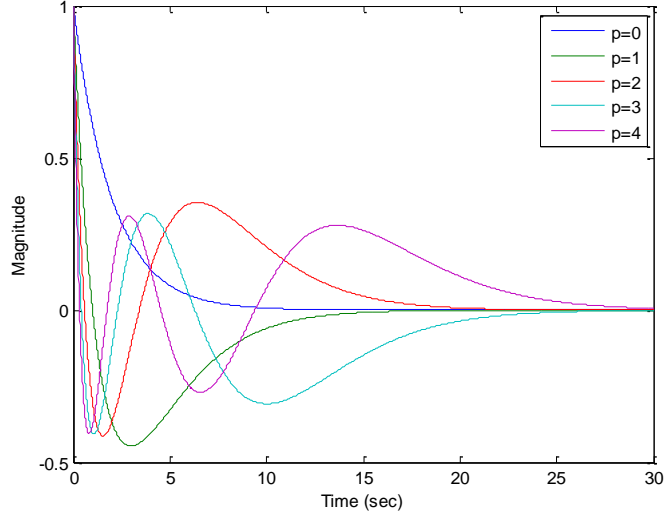
Figure 34. Weighted Laguerre polynomials for orders $p = 0$ to $p = 4$.

As shown in Figure 34, Laguerre basis function $\varphi_p(t)$ decays to 0 as t increases where $\varphi_p(t)$ decays slower as its order p is higher. Therefore, as the time duration gets longer, higher order Laguerre basis functions are required for accurate result in the approximation in (81). However, it is difficult to compute Laguerre basis functions with higher order for a long time interval. The Laguerre basis function is represented as the product of an exponentially decaying function and the Laguerre polynomial. The nth Laguerre basis function $\varphi_n(t)$ can be represented by multiplying the Laugerre polynomial with an exponential function as:

$$\varphi_n(t) = L_n(t) \cdot e^{-\frac{t}{2}}, \tag{82}$$

where $L_n(t)$ stands for nth Laguerre polynomial.

Figure 35 (a) shows a flowchart of the approach used in [2] to compute $\varphi_n(t)$. The Laguerre polynomial of order p can be calculated by using the following recurrence relation:

$$L_0(t) = 1, \tag{83}$$

$$L_1(t) = 1 - t, \tag{84}$$

53

$$pL_p(t) = (2p - 1 - t)L_{p-1}(t) - (p - 1)L_{p-2}(t), \text{ for } p \geq 2. \qquad (85)$$

By following the recurrence loop in Figure 35 (a), the Laguerre polynomial $L_n(t)$ becomes very large as the order n increases. Beyond a large enough order number, the basis functions become too large to be represented using IEEE-754 floating-point standard, and therefore are computed as *Inf* in the digital computer. On the other hand, as is well known, the exponential function $e^{-t/2}$ decays to zero rapidly and therefore the exponential function is treated as absolute zero in the computer beyond a certain time point. Therefore, after some time, the basis function no longer has any meaningful value and is represented as *Inf*×0 or *NaN* (not a number), as shown in Figure 36. In Figure 36, the graph terminates abruptly around $t = 1440$ when the computer cannot determine the value of the basis functions.

Therefore, because of the difficulty in computing Laguerre basis functions of high order for long time interval, the Laguerre-FDTD method proposed in [24] has the limitation that simulation can only be performed for a limited time duration and cannot be performed for all time. The SLeEC scheme proposed in [27] overcomes such a limitation on the maximum time duration by dividing total simulation time into different time intervals. However, it has a drawback that error is accumulated as the number of time intervals increases. Hence, obtaining the low frequency response using SLeEC is still a challenge. The ultimate solution for the limitation on time duration is to enable the calculation of Laguerre basis functions with sufficiently high order and long time durations.

(a)   (b)
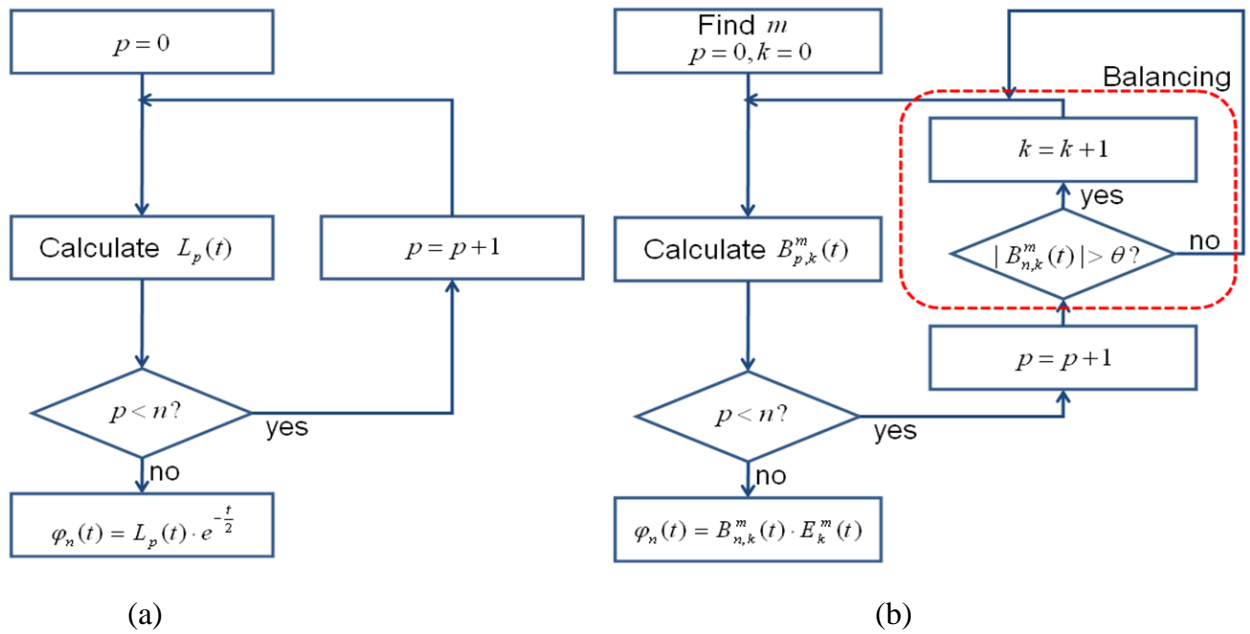
Figure 35. Algorithm to compute the Laguerre basis function.
(a): algorithm in the prior work, (b): proposed algorithm
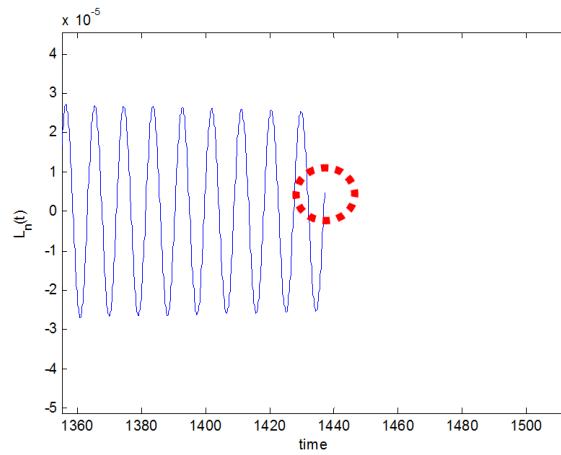
Figure 36. Calculated 1000th Laguerre basis function by the prior method.

5.2 Introduction of Balanced Laguerre Polynomial and Balanced Exponential Function

The previous limitation can be overcome by introducing a balancing process in the recurrence loop as shown in Figure 35 (b). For the description of the balancing process in the proposed algorithm, $\varphi_n(t)$ is represented as follows:

$$\varphi_n(t) = B_{n,k}^m(t) \cdot E_k^m, \tag{86}$$

where

$$B_{n,k}^m(t) = L_n(t) \cdot e^{-\frac{k}{m}\cdot\frac{t}{2}}, \tag{87}$$

$$E_k^m = e^{-(1-\frac{k}{m})\cdot\frac{t}{2}}. \tag{88}$$

$B_{n,k}^m(t)$ and $E_k^m(t)$ in (87) and (88) are called the balanced Laguerre polynomial and balanced exponential function, respectively. Variable $B_{n,k}^m(t)$ can be calculated using (83)-(85) and (87). New parameters and variables such as θ, m, and k are introduced related to the balancing process. θ is a threshold value that limits the magnitude of the balanced Laguerre polynomial in the recurrence loop. Parameters m and k represent the strength of balancing process and the degree of balancing, respectively. A relation between the balanced Laguerre polynomials before and after the increment of degree of balancing is given by

$$B_{p,k}^m(t) = B_{p,k-1}^m(t)e^{-\frac{1}{m}\cdot\frac{t}{2}}. \tag{89}$$

where m should be selected to ensure $e^{-\frac{1}{m}\cdot\frac{t}{2}}$ is large enough to handle in the IEEE-754 floating-point standard. For large t, $e^{-\frac{1}{m}\cdot\frac{t}{2}}$ can be too small to be represented as non-zero value in the computer. It should be avoided since $B_{p,k}^m(t)$ goes to zero by the increment in the degree of balancing k in that case. Therefore, m needs to be sufficiently large to make $e^{-\frac{1}{m}\cdot\frac{t}{2}}$ treatable in the IEEE-754 floating-point standard.

A rule of thumb for representing m in terms of the threshold value θ is the following:

$$m \approx \frac{t}{2\ln\theta}. \qquad (90)$$

It is required to make the threshold value θ as follows in terms of m:

$$\theta \approx e^{\frac{1}{m}\cdot\frac{t}{2}}. \qquad (91)$$

If (91) is satisfied, by (89), the magnitude of the balanced Laguerre polynomial becomes approximately 1 as the degree of balancing increases.

The balancing process prevents the magnitude of balanced Laguerre polynomials from being too large. If the magnitude of a balanced Laguerre polynomial gets larger than the threshold value θ, the balancing process is performed by increasing the degree of balancing k. Since m and t have positive values, the magnitude of the balanced Laguerre polynomial reduces as the degree of balancing k increases, as shown in (89). Therefore, the balanced Laguerre polynomial will always remain less than θ in the recurrence loop, which circumvents the *NaN* problem.

After the computation of $B_{n,k}^{m}(t)$ is completed, the Laguerre basis function can be calculated using (86). Hence, this formulation enables the application of the Laguerre-FDTD method for computing the response over long time duration.

The computation of the 1000th Laguerre basis function $\varphi_n(t)$ by the proposed method and the prior method used in [27] is plotted in Figure 37. The method in [27] cannot calculate the basis function $\varphi_n(t)$ when t is larger than 1440, which is equivalent to 20 *ns* when the time-scale factor is 7×10^8. However, the proposed method successfully obtains the value of Laguerre basis function at time t greater than 1440, as shown in Figure 37.
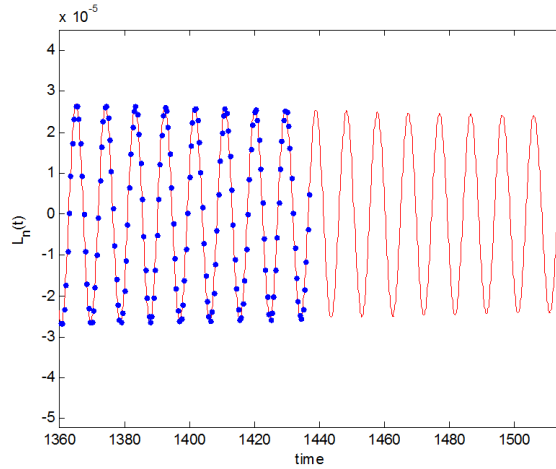
Figure 37. Calculated 1000th Laguerre basis function.
Red: proposed method, blue dots: prior method

5.3 Numerical Results

As shown in Figure 38, a coplanar transmission line in the package is connected to on-chip coplanar line through solder bumps. Two ports are defined at each end of the package trace. The structures are assumed to be lossless in this example. This structure has a scale ratio of 1:100,000, which is from 200 *nm* of the on-chip via's diameter to 20 *mm* of the package interconnection's length. Due to the very fine mesh required for the on-chip structure and the very small time step based on the CFL condition, the estimated simulation time for 1 *us* long simulation is approximately 212 days. This structure was simulated using Laguerre-FDTD with the proposed method for calculating Laguerre basis functions, which took 36 hours. In this example, Laguerre-FDTD showed $100 \times$ speed up over FDTD.

58
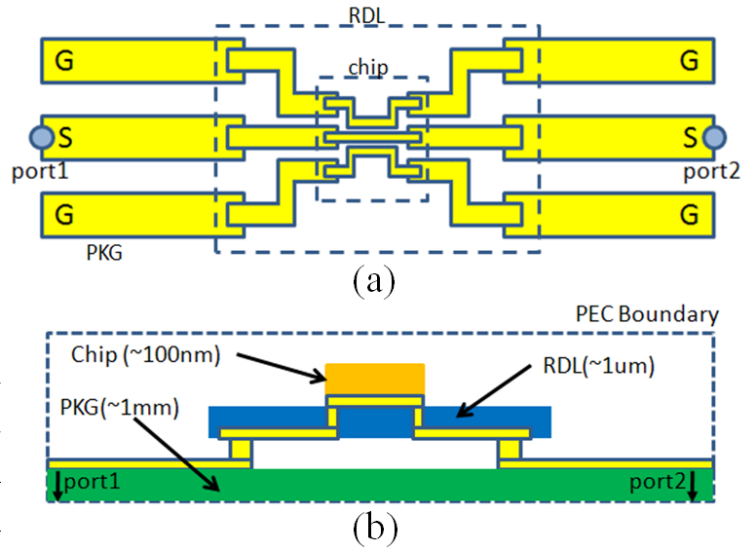
Figure 38. Coplanar transmission line structure from PKG to chip.
(a): top view (b): cross-sectional view

Since the transient response was computed for 1 *us* duration as shown in Figure 39, the insertion loss (s21) from 1MHz to 10GHz could be extracted from the simulated time-domain waveform using an FFT, as shown in Figure 40.
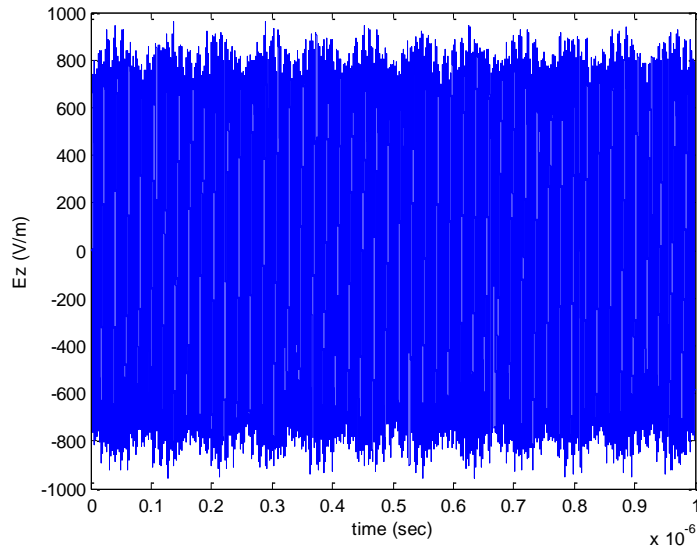
Figure 39. Simulated time-domain waveform at Port 1.
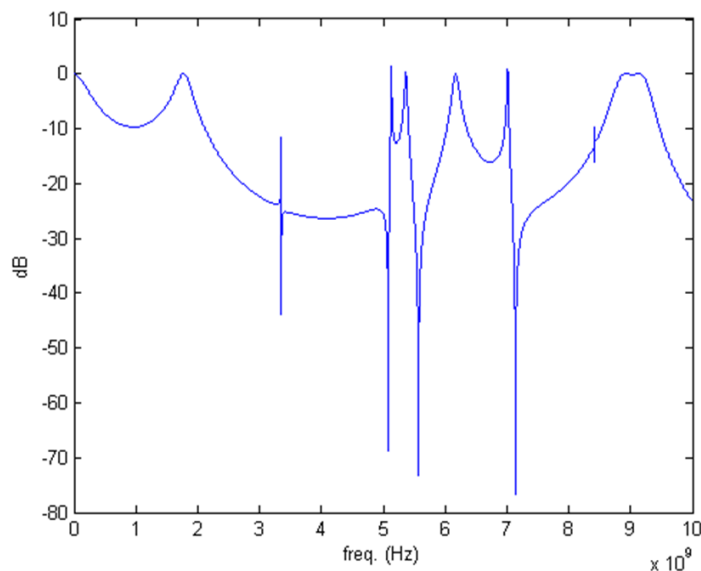
Figure 40. Insertion loss (s21) of the coplanar transmission line structure.

5.4 Summary

Due to the difficulty in calculating Laguerre basis functions for long time intervals, Laguerre-FDTD has a limitation on the maximum time duration over which the structure can be simulated. The SLeEC method uses a technique that enables simulation for long time intervals by dividing, the total simulation time into different time intervals. However, it still has a drawback that error accumulates as the number of time intervals increase. Hence, obtaining the low frequency response using SLeEC has been a challenge.

This chapter has described a method to compute the transient response for long time intervals using the Laguerre-FDTD method. To enable simulation from DC to high frequency, the basis function representations have been modified in this chapter by introducing balanced Laguerre polynomials and balanced exponential functions. A simulation result using the proposed method has shown 100x speed up over the FDTD scheme, making it a viable candidate for the co-simulation of chip-package interconnect structures.

60

CHAPTER VI

EFFICIENT FREQUENCY-DOMAIN ANALYSIS USING TIME-DOMAIN SIMULATIONS

A methodology for obtaining frequency-domain parameters from time-domain simulations is discussed in this chapter. If the time-domain response does not sufficiently decay to zero before the end of the time duration of interest, due to spectral leakage, its discrete Fourier transform has a series of lobes, which results in inaccurate frequency-domain parameters. To avoid the special leakage problem, there are two solutions: run a time-domain simulation until the transient response decays to zero, or apply a windowing function to the transient response which forces the transient response to decay before the time duration ends. In this chapter, a time-domain simulation technique to accelerate the damping which may reduce the simulation run time is presented. Especially in low-frequency analysis, the time-domain simulation needs to be performed for a long time. In the conventional FDTD method, since the size of the time step is limited, simulation for long times requires a large number of iterations, resulting in an increased run time. However, utilizing Laguerre-FDTD's marching-on-in-degree nature, a time-domain simulation for low-frequency analysis can be performed without the consumption of additional resources compared to mid or high frequency analysis. This is shown in this chapter, followed by a numerical example.

6.1 Time-domain to Frequency-domain Transformation

Consider a two-port network as shown in Figure 41. A method introduced in this section for the two-port network example can be easily extended to a multi-port network. For a two-port network, Z_{11} and Z_{21} can be obtained from the following equations:

$$Z_{11} = \frac{F\{V_1(t)\}}{F\{I_1(t)\}} \big| I_2 = 0, \tag{92}$$

$$Z_{21} = \frac{F\{V_2(t)\}}{F\{I_1(t)\}} \big| I_2 = 0, \tag{93}$$

where F is the Fourier transform operator, V_i and I_i are the voltage and current at port i, respectively. Z_{12} and Z_{22} can be calculated similarly.
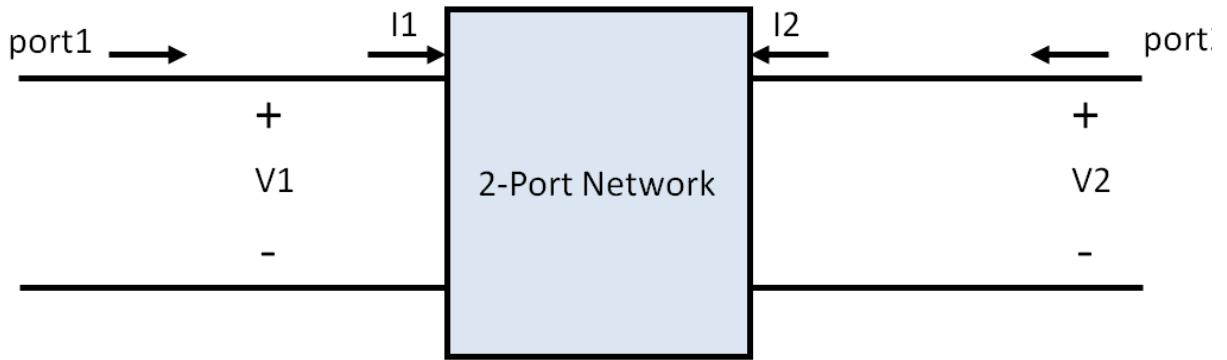
Figure 41. Two-port network.

Voltage at a port is defined using the integral of electric field as follows:

$$V = - \int_C \bar{E} \cdot d\bar{l}, \tag{94}$$

where C is an arbitrary path connecting both ends of the port.

Once Z parameters are calculated from the time-domain simulation, S parameters can be calculated from the Z parameters using the following equations [33]:

$$S_{11} = \frac{(Z_{11} - Z_0)(Z_{22} + Z_0) - Z_{12}Z_{21}}{\Delta}, \tag{95}$$

$$S_{12} = \frac{2Z_0 Z_{12}}{\Delta}, \tag{96}$$

62

$$S_{21} = \frac{2Z_0 Z_{21}}{\Delta}, \tag{97}$$

$$S_{22} = \frac{(Z_{11} + Z_0)(Z_{22} - Z_0) - Z_{12}Z_{21}}{\Delta}, \tag{98}$$

where $\Delta = (Z_{11} + Z_0)(Z_{22} + Z_0) - Z_{12}Z_{21}$.

In a general multi-port network, the relation between S parameters and Z parameters is given by

$$[S] = ([Z] + Z_0 \mathrm{I}_n)^{-1}([Z] - Z_0 \mathrm{I}_n). \tag{99}$$

where $[S]$ and $[Z]$ represents the S and Z parameter matrix, respectively, and I_n is the identity matrix of size n.

6.2 Efficient Time-domain Simulation for Frequency-domain Analysis

As discussed in the previous section, frequency-domain analysis can be done using a time-domain simulation. Since only a finite-length transient response can be performed, if the transient response does not decay to zero within the simulated time duration, some energy leaks out of the original spectrum into other frequencies, which is called "spectral leakage." The spectral leakage results in a series of lobes in the frequency domain and inaccurate frequency-domain parameters. To avoid the special leakage problem, there are two solutions: run a time-domain simulation until the transient response decays to zero, or apply a windowing function to the transient response which forcefully makes the transient response decay before the time duration ends. However, the second option which applies a windowing function may introduce error in the calculation of frequency-domain parameters because it distorts the original transient response. In this chapter, a time-domain simulation technique to accelerate the damping is presented, which can reduce the required length of a time-domain simulation compared to the first option to run a time-domain simulation until the transient response decays.

To make the transient response decay rapidly, use of a resistive source has been presented in [34] [35] [36] [37]. However, none of these authors de-embedded the effect of the resistance at the source location. In order to accelerate the decay of transient response for the frequency-domain analysis of the two-port network shown in Figure 41, additional shunt resistors are attached at each port as shown in Figure 42.
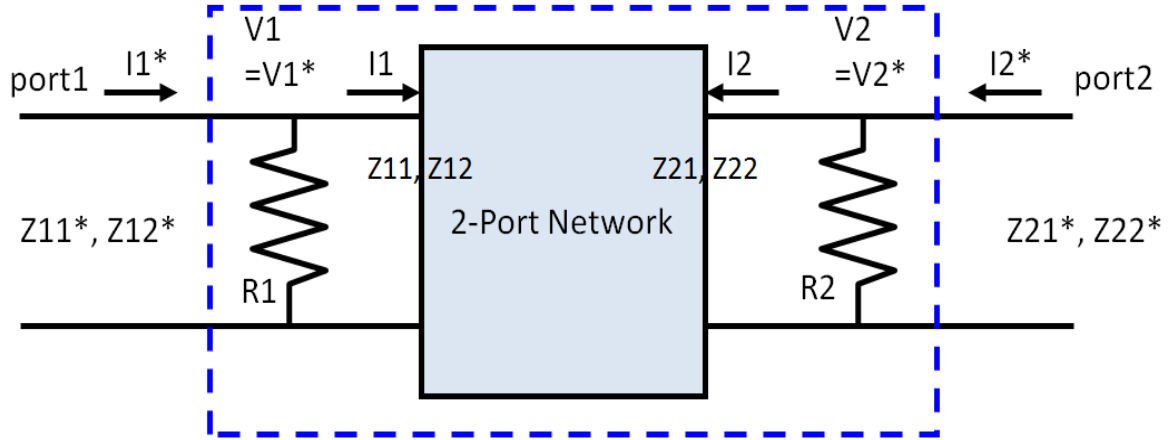
Figure 42. Two-port network with additional resistances at port locations.

When the resistances at the ports are sufficiently small, the resistors make the time-domain waveform decay quickly after its excitation using the source current. In Figure 42, the network with resistors outlined by dashed lines shows the modified network containing the original two-port network. The relationship between the original network and the modified network can be expressed as follows:

$$[V^*] = [V],$$ (100)

$$[I^*] = [I] + [R]^{-1}[V],$$ (101)

$$[Z^*][I^*] = [V^*],$$ (102)

where $[V] = \begin{bmatrix} V_1 \\ V_2 \end{bmatrix}$, $[I] = \begin{bmatrix} I_1 \\ I_2 \end{bmatrix}$, $[Z] = \begin{bmatrix} Z_{11} & Z_{12} \\ Z_{21} & Z_{22} \end{bmatrix}$, $[R] = \begin{bmatrix} R_1 & 0 \\ 0 & R_2 \end{bmatrix}$. Variables with an asterisk represent respective variables in the modified network.

Inserting (100) and (101) into (102), we get:

$$[Z^*]([I] + [R]^{-1}[V]) = [V], \tag{103}$$

$$((I - [Z^*][R]^{-1})^{-1} [Z^*])[I] = [V]. \tag{104}$$

Therefore, the Z parameters of the original network can be represented in terms of the modified network's Z parameters as

$$[Z] = (I - [Z^*][R]^{-1})^{-1} [Z^*]. \tag{105}$$

Solving the modified network instead of the original network, the simulation run time can be significantly reduced as the transient responses rapidly decay. By de-embedding the effect of the additional resistances at ports in the modified network using (105), accurate frequency-domain responses can be calculated using a time-domain simulation over a short time period. This method can be extended to a multi-port network easily, if necessary.

6.3 Efficient Laguerre-FDTD Simulation for Low Frequency Analysis

Analysis of low frequency behavior using time-domain simulation requires the transient response for a long time regardless of how quick the transient response reaches the steady state. When the lower bound of the frequency range of interest is f_L, the required length of the time-domain simulation T_f is given by

$$T_f = \frac{1}{f_L}. \tag{106}$$

In the FDTD method, the time step is restricted by the CFL limit as stated earlier. Therefore, for low frequency analysis, numerous iterations are needed using the FDTD scheme, resulting in a fairly long computation time. For example, if the required frequency range is halved, then the time duration of the time-domain simulation should be doubled, which requires twice the computation time.

However, in the Laguerre-FDTD's scheme, there is a time-scale factor and the time step is not restricted. Because of the time-scale factor, as long as the percent bandwidth of the transient

65

response stays constant, computation time does not increase by adjusting the time-scale factor in the case that the frequency range of interest is lowered.

For example, let us consider two cases for a given structure: (1) transient simulation for 5 *ns* with a frequency range of interest from 500 MHz to 1 GHz, and (2) transient simulation for 5 u*s* with a frequency range of interest from 500 kHz to 1 MHz. If the FDTD method is used, Case (2) requires 1000 times more computation time than Case (1) because the number of iterations is 1000 times larger. However, analysis of Case (2) using the Laguerre-FDTD method can be performed with almost the same computation time required for Case (1) using the Laguerre-FDTD by adjusting the time-scale factor and source's frequency in Case (2) by 1/1000 compared to Case (1).

6.4 Numerical Results

The test structure is a 2.4 GHz band-pass filter structure shown in Figure 43. It is a 4-layer structure in a homogeneous medium of relative dielectric constant 3.48. The filter dimensions are 3200 *um* $\times$ 3000 *um* $\times$ 16 *um*. The entire structure is enclosed in a PEC box and discretized into $72 \times 68 \times 15 = 73{,}440$ cells. The conductor material is PEC. The dielectric material is assumed to be lossless and non-dispersive. A modulated Gaussian source current is excited at each port in the time-domain simulations. Since the structure is lossless and has a resonance near 2.4 GHz, transient responses oscillate forever without damping, as shown in Figure 44. However, for the case where resistors of 50 ohm are attached at all ports, the transient responses decay quickly as shown in Figure 45. Figure 45 shows the electric field in the z direction at Port 1 after the excitation of the source current at Port 1. Calculated S parameters are shown in Figure 46 and compared with S parameters from a frequency-domain commercial tool Sonnet, which uses method-of-moment analysis [38]. Comparison with the commercial tool shows good correlation in this example.

66
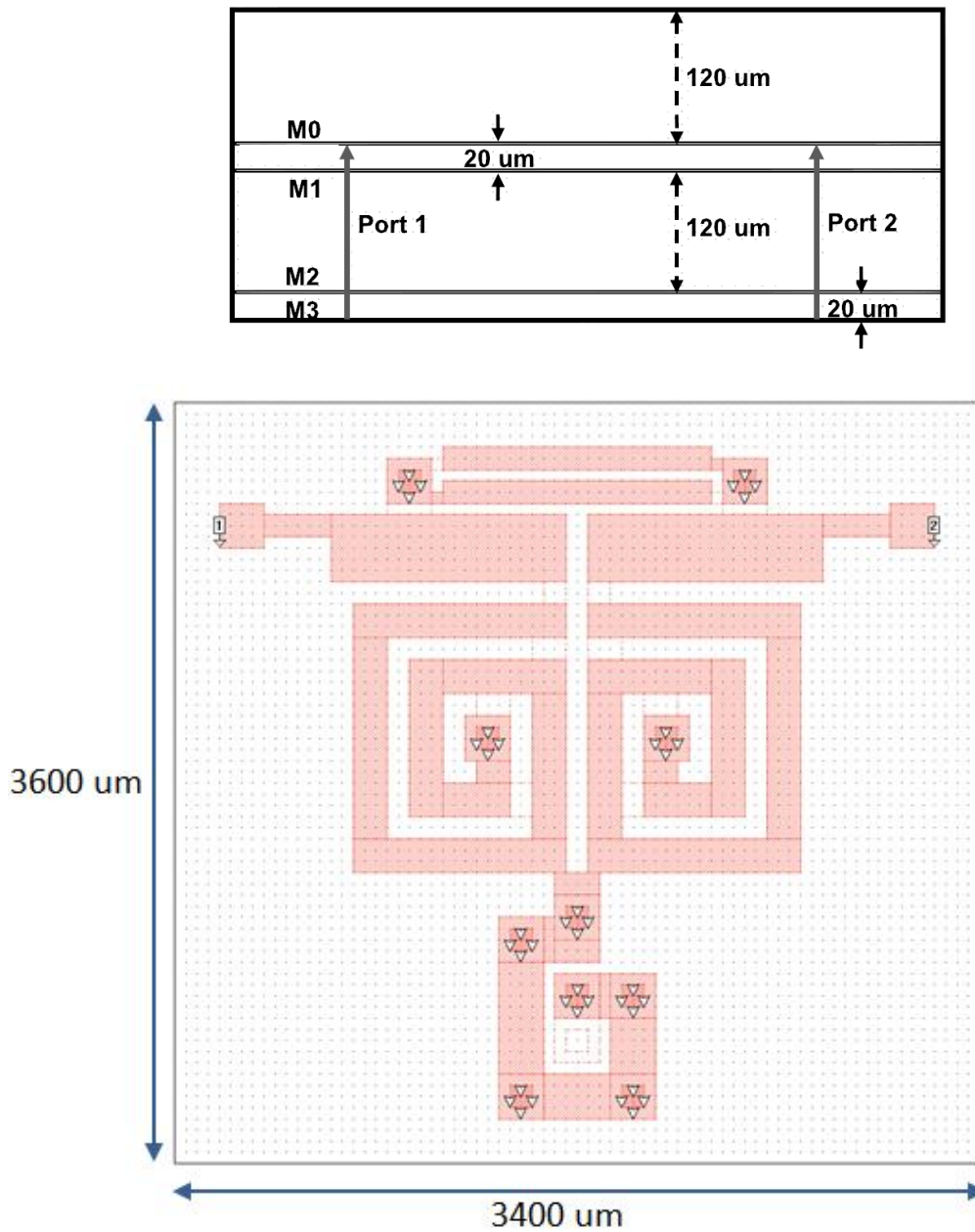
Figure 43. 2.4GHz band-pass filter. (top: cross-sectional view, bottom: top view of the layout of the M0 layer. Dots are separated by 50 *um*)
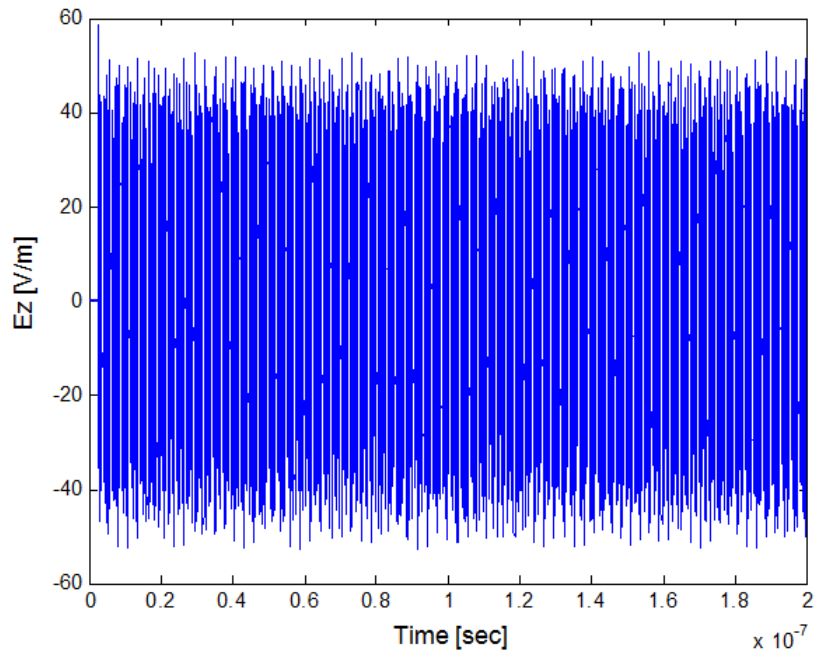
Figure 44. Oscillatory transient response.
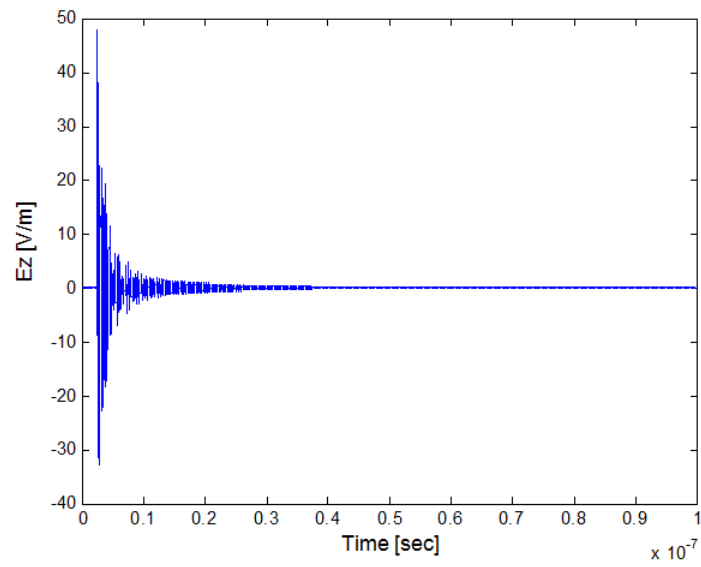
Figure 45. Rapidly decaying transient response.

68
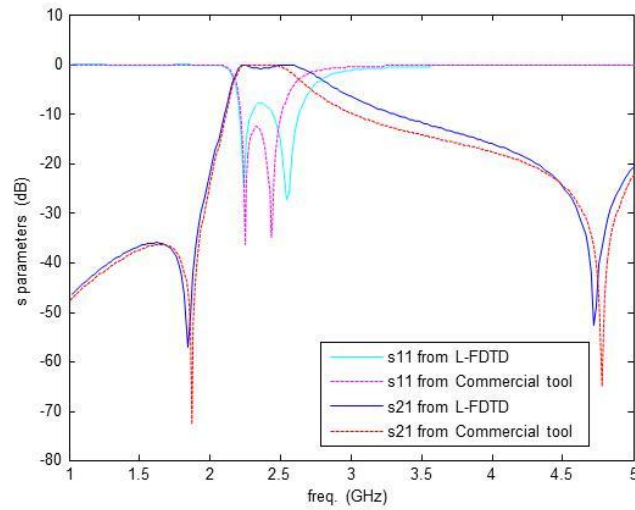
Figure 46. Calculated S parameters.

6.5 Summary

Frequency-domain analysis can be performed from time-domain simulations using an FFT. For efficient time-domain simulations for frequency-domain analysis, a method that attaches resistors at each port has been proposed, which dampens the transient responses. A relation between the original network and the modified network with port resistors has been derived. Therefore, the resistors can be de-embedded after the calculation of frequency-domain parameters. For low-frequency results, being a marching-on-in-degree method, the Laguerre-FDTD has an advantage in that the low-frequency response can be calculated efficiently without consumption of considerable additional resources while the FDTD method suffers from large numbers of iterations which consumes more run time.

CHAPTER VII

MODELING OF DISPERSIVE AND CONDUCTIVE MATERIAL IN 3-D STRUCTURES

Luebbers introduced a frequency-dependent FDTD formulation for dispersive materials in 1990 [39]. In this chapter, a Laguerre-FDTD formulation to model wave propagation is introduced using the Laguerre transform of the convolution operator. The proposed formulation is verified with a numerical example and compared with the results from the FDTD formulation. The comparison reveals that the frequency-dependent FDTD formulation for dispersive material is properly implemented in the Laguerre domain so that frequency-dependent dispersive materials can be analyzed using the Laguerre-FDTD simulation method.

7.1 Time-domain Formulation for Frequency-dependent Materials

In this section, materials are assumed to be linear and isotropic. The frequency-domain information (such as permittivity and permeability) is Fourier transformed to a time-domain susceptibility function [40]. For simplicity, only the permittivity (electric susceptibility) is discussed in this section. The extension to magnetic permeability is similar. In the time domain, we have

$$\bar{D}(t) = \varepsilon_\infty \varepsilon_0 \bar{E}(t) + \varepsilon_0 \int_0^t \bar{E}(t-\tau)\chi(\tau)d\tau, \qquad (107)$$

where $\chi(\tau)$, ε_0 and ε_∞ represent the time-domain electric susceptibility function, permittivity of free space, and infinite frequency relative permittivity, respectively.

7.2 Transformation of Convolution Operation from Time-domain to Laguerre-domain

In order to represent (107) in the Laguerre domain, transformation of the convolution term in (107) to the Laguerre domain is required. The Laguerre domain is based on orthonormal Laguerre basis functions. As stated in the earlier sections, the ith Laguerre basis function $\varphi_i(t)$ is defined as the product of the ith Laguerre polynomial and an exponential function [24], given by

$$\varphi_i(st) = L_i(st) \cdot e^{-\frac{st}{2}}, \tag{108}$$

where $L_i(t)$ is the ith Laguerre polynomial and s is the time-scaling constant.

Let $X(t)$ and $Y(t)$ be arbitrary time-domain waveforms defined for $t > 0$. They can be represented in the Laguerre domain as a sum of Laguerre basis functions scaled by Laguerre basis coefficients X_i and Y_i, as shown in (109) and (110):

$$X(t) = \sum_{i=0}^{\infty} X_i \varphi_i(st), \tag{109}$$

$$Y(t) = \sum_{i=0}^{\infty} Y_i \varphi_i(st). \tag{110}$$

Their convolution $Z(t)$ can be written as

$$Z(t) = X(t) * Y(t) = \int_0^{\infty} X(t - \tau)Y(\tau)d\tau. \tag{111}$$

The Laguerre-domain representation of $Z(t)$ can be written as

$$Z(t) = \sum_{i=0}^{\infty} Z_i \varphi_i(st). \tag{112}$$

Applying the temporal testing procedure with $\varphi_i(t)$, $Z(t)$'s ith Laguerre basis coefficients can be obtained as follows:

$$Z_i = \int_0^\infty \varphi_i(st)Z(t)dt$$

$$= \int_0^\infty \varphi_i(st) \int_0^\infty X(t - \tau)Y(\tau)d\tau \, dt. \tag{113}$$

Summation of Z_i from $i = 0$ to n is given by

$$\sum_{i=0}^n Z_i = \sum_{i=0}^n \int_0^\infty \varphi_i(st)Z(t)dt$$

$$= \int_0^\infty \sum_{i=0}^n \varphi_i(st) \int_0^\infty X(t - \tau)Y(\tau)d\tau dt$$

$$= \int_0^\infty \sum_{i=0}^n L_i(st)e^{-\frac{st}{2}} \int_0^\infty X(t - \tau)Y(\tau)d\tau dt$$

$$= \int_0^\infty (\sum_{i=0}^n L_i\big(s(t - \tau)\big)L_{n-i}(s\tau)e^{-\frac{s(t-\tau)}{2}} e^{-\frac{s\tau}{2}} \tag{114}$$

$$\cdot \int_0^\infty X(t - \tau)Y(\tau)d\tau)dt$$

$$= \sum_{i=0}^n \int_0^\infty \int_0^\infty \left(L_i(sk)e^{-\frac{sk}{2}}X(k) \cdot L_{n-i}(s\tau)e^{-\frac{s\tau}{2}}Y(\tau) \right) d\tau dk,$$

where $k=t-\tau$.

In (114), the following property of Laguerre polynomials has been used:

$$\sum_{i=0}^n L_i(x + y) = \sum_{i=0}^n L_i(x)L_{n-i}(y). \tag{115}$$

Since k and τ are independent variables, separating terms of k and terms of τ in (114), we get

$$\sum_{i=0}^n Z_i = \sum_{i=0}^n \int_0^\infty L_i(sk)e^{-\frac{sk}{2}}X(k)dk \int_0^\infty L_{n-i}(s\tau)e^{-\frac{s\tau}{2}}Y(\tau)d\tau \tag{116}$$

72

$$= \sum_{i=0}^{n} \int_{0}^{\infty} \varphi_i(sk) X(k) dk \int_{0}^{\infty} \varphi_{n-i}(s\tau) Y(\tau) d\tau$$

$$= \sum_{i=0}^{n} X_i Y_{n-i} .$$

From the summation of Z_i in (116), the nth order Laguerre basis coefficient for the convolution of $X(t)$ and $Y(t)$ is obtained as follows:

$$Z_n = \sum_{i=0}^{n} X_i Y_{n-i} - \sum_{i=0}^{n-1} Z_i$$

$$= \sum_{i=0}^{n} X_i Y_{n-i} - \sum_{i=0}^{n-1} X_i Y_{n-1-i}. \tag{117}$$

7.3 Laguerre-domain Formulation for Frequency-Dependent Materials

Under the assumption that $\bar{E}(t)$ is defined only for $t > 0$, (107) can be rewritten using the infinite integral as

$$\bar{D}(t) = \varepsilon_\infty \varepsilon_0 \bar{E}(t) + \varepsilon_0 \int_{0}^{\infty} \bar{E}(t - \tau) \chi(\tau) d\tau. \tag{118}$$

This assumption is reasonable since the Laguerre transform is for functions of t defined for $0 \leq t \leq \infty$. The Laguerre-domain representation of (118) can be written as

$$\bar{D}_n = \varepsilon_\infty \varepsilon_0 \bar{E}_n + \varepsilon_0 \left(\sum_{i=0}^{n} \bar{E}_i \chi_{n-i} - \sum_{i=0}^{n-1} \bar{E}_i \chi_{n-1-i} \right)$$

$$= \varepsilon_0 (\varepsilon_\infty + \chi_0) \bar{E}_n + \varepsilon_0 \sum_{i=0}^{n-1} \bar{E}_i (\chi_{n-i} - \chi_{n-i-1}) \tag{119}$$

$$= \varepsilon_0 (\varepsilon_\infty + \chi_0) \bar{E}_n + \varepsilon_0 \sum_{i=0}^{n-1} \bar{E}_i \Delta \chi_{n-i},$$

where

73

$$\bar{D}_i = \int_0^\infty \varphi_i(t)\bar{D}(t)dt, \tag{120}$$

$$\bar{E}_i = \int_0^\infty \varphi_i(t)\bar{E}(t)dt, \tag{121}$$

$$\chi_i = \int_0^\infty \varphi_i(t)\chi(t)dt, \tag{122}$$

$$\Delta\chi_i = \chi_i - \chi_{i-1}. \tag{123}$$

Maxwell's curl equations in differential form are

$$\nabla \times \bar{H} = \frac{\partial \bar{D}}{\partial t} + \bar{J} + \sigma\bar{E}, \tag{124}$$

$$\nabla \times \bar{E} = -\frac{\partial \bar{B}}{\partial t}. \tag{125}$$

In (125), we assume that $\bar{B} = \mu\bar{H}$ for linear and isotropic media.

By applying the curl operation to (125) and substituting (124), we get

$$\nabla \times \nabla \times \bar{E} = -\mu\frac{\partial^2 \bar{D}}{\partial t^2} - \mu\frac{\partial(\bar{J} + \sigma\bar{E})}{\partial t}. \tag{126}$$

The first and second derivative with respect to time can be expressed as [24]

$$\frac{\partial \bar{U}(t)}{\partial t} = s \sum_{i=0}^\infty \left[\frac{1}{2}\bar{U}_i + \sum_{j=0,i>0}^{i-1} \bar{U}_j \right] \varphi_i(st), \tag{127}$$

$$\frac{\partial^2 \bar{U}(t)}{\partial t^2} = s^2 \sum_{i=0}^\infty \left[\frac{1}{4}\bar{U}_i + \sum_{j=0,i>0}^{i-1} (i-j)\bar{U}_j \right] \varphi_i(st). \tag{128}$$

Now (126) is transformed into the Laguerre domain with consideration of the frequency-dependent behavior of dispersive material using (127), and (128), which results in

$$\nabla \times \nabla \times \bar{E}_n = -\mu s^2 \left[\frac{1}{4}\bar{D}_n + \sum_{j=0,n>0}^{n-1} (n-j)\bar{D}_j \right]$$

$$- \mu s \left[\frac{1}{2}(\bar{J}_n + \sigma\bar{E}_n) + \sum_{j=0,n>0}^{n-1} (\bar{J}_j + \sigma\bar{E}_j) \right].$$

(129)

Using (119), (129) can be rewritten as follows:

$$\nabla \times \nabla \times \bar{E}_n + \frac{\mu\varepsilon_0 s^2}{4}(\varepsilon_\infty + \chi_0)\bar{E}_n + \frac{\mu s\sigma}{2}\bar{E}_n$$

$$= -\mu s^2 \left[\frac{1}{4}\varepsilon_0 \sum_{i=0}^{n-1} \bar{E}_i \Delta\chi_{n-i} \right.$$

$$+ \sum_{j=0,n>0}^{n-1} (n-j)\varepsilon_0(\varepsilon_\infty + \chi_0)\bar{E}_j$$

(130)

$$\left. + \sum_{j=0,n>0}^{n-1}\sum_{i=0}^{j-1} (n-j)\varepsilon_0\bar{E}_i\Delta\chi_{j-i} \right]$$

$$- \mu s \left[\frac{1}{2}\bar{J}_n + \sum_{j=0,n>0}^{n-1} (\bar{J}_j + \sigma\bar{E}_j) \right].$$

The double curl on the left side in (130) can be represented in discretized form using Yee's space lattice and the central difference scheme.

It is important to note that the right side of (130) consists of Laguerre basis coefficients up to $(n-1)$th order for E and Laguerre basis coefficients for the source current J, while the left side has only nth order Laguerre basis coefficients for the electric field E. Therefore, (130) enables a

recursive calculation of Laguerre coefficients using previous coefficients for the electromagnetic waves within structures containing dispersive material.

7.4 Customized Formulation for Dispersion Model

The frequency domain information is Fourier transformed to a time-domain susceptibility function $\chi(t)$ [39]. A Laguerre-domain susceptibility function χ_i is calculated by transforming the time-domain susceptibility function into the Laguerre domain. Using the Laguerre-domain susceptibility function, the electric flux density $\overline{D}_n$ can be represented in the Laguerre domain as shown in the previous section:

$$\overline{D}_n = \varepsilon_\infty \varepsilon_0 \overline{E}_n + \varepsilon_0 \left(\sum_{i=0}^{n} \overline{E}_i \chi_{n-i} - \sum_{i=0}^{n-1} \overline{E}_i \chi_{n-1-i} \right), \tag{131}$$

where ε_0 and ε_∞ represent the electric permittivity of free space, and the infinite frequency relative permittivity, respectively.

Using (131), the frequency-dependent dispersion can be incorporated in the Laguerre-FDTD simulations. However, due to the summation terms in (131), all previous solutions from order $i = 0$ to n - 1 are required to calculate $\overline{D}_n$, the nth order Laguerre basis coefficient for the electric flux density. Therefore, as order increases in the Laguerre-FDTD computation steps, a significant amount of memory is needed to store all solutions in the previous orders. Such a large memory consumption for dispersion introduces inefficiency to the Laguerre-FDTD method in solving practical problems containing dispersive materials.

7.4.1 Debye model

The Debye model satisfies the Kramers-Kronig relationship and results in an efficient model for the frequency-dependent complex permittivity, given by

$$\varepsilon(\omega) = \varepsilon_\infty + (\varepsilon_s - \varepsilon_\infty) \sum_{i=1}^{N} \frac{a_i}{1 + j\omega\tau_i},\tag{132}$$

where a_i and τ_i represent the strength and time constants of various relaxation processes, ε_s is the static permittivity, and ε_∞ is the permittivity at infinite frequency. To maintain an approximately constant loss tangent over a bandwidth of a few decades, $N > 1$ is required. However, for simplicity, the case with $N = 1$ is discussed in this section. It can be easily extended to $N > 1$ in a similar fashion. The frequency-domain susceptibility function is

$$\chi(\omega) = (\varepsilon_s - \varepsilon_\infty) \frac{a}{1 + j\omega\tau},\tag{133}$$

where a and τ are the strength and time constant of the first-order Debye relaxation process. The fourier transform of (133) is given by

$$\chi(t) = (\varepsilon_s - \varepsilon_\infty) \frac{a}{\tau} e^{-\frac{t}{\tau}} U(t),\tag{134}$$

where $U(t)$ is the unit step function. The time-domain susceptibility function for the Debye model is represented in the Laguerre domain as follows:

$$\chi_i = \alpha_D p_D^i,\tag{135}$$

where

$$\alpha_D = (\varepsilon_s - \varepsilon_\infty) \frac{2a}{2 + s\tau}, \quad p_D = \frac{2 - s\tau}{2 + s\tau},\tag{136}$$

and s is a time-scaling factor in the Laguerre-FDTD.

Equation (131) can be rewritten as follows:

$$\bar{D}_n = \varepsilon_\infty \varepsilon_0 \bar{E}_n + \varepsilon_0 \bar{Z}_n\tag{137}$$

where

$$\bar{Z}_n = \sum_{i=0}^{n} \bar{E}_i \chi_{n-i} - \sum_{i=0}^{n-1} \bar{E}_i \chi_{n-1-i}.\tag{138}$$

Inserting (135) into (137), we have

77

$$\bar{Z}_n = \alpha \left(\sum_{i=0}^{n} \bar{E}_i p_D^{n-i} - \sum_{i=0}^{n-1} \bar{E}_i p_D^{n-1-i} \right), \tag{139}$$

By subtracting $p\bar{Z}_{n-1}$ from $\bar{Z}_n$, we get

$$
\begin{aligned}
\bar{Z}_n - p_D \bar{Z}_{n-1} &= \alpha_D \left(\sum_{i=0}^{n} \bar{E}_i p_D^{n-i} - \sum_{i=0}^{n-1} \bar{E}_i p_D^{n-1-i} \right) \\
&\quad - \alpha_D p_D \left(\sum_{i=0}^{n-1} \bar{E}_i p_D^{n-1-i} - \sum_{i=0}^{n-2} \bar{E}_i p_D^{n-2-i} \right) \\
&= \alpha_D \left(\sum_{i=0}^{n} \bar{E}_i p_D^{n-i} - \sum_{i=0}^{n-1} \bar{E}_i p_D^{n-1-i} \right) \\
&\quad - \alpha_D \left(\sum_{i=0}^{n-1} \bar{E}_i p_D^{n-i} - \sum_{i=0}^{n-2} \bar{E}_i p_D^{n-1-i} \right) \\
&= \alpha_D (\bar{E}_n - \bar{E}_{n-1}).
\end{aligned}
\tag{140}
$$

Using (140), $\bar{Z}_n$ can be calculated recursively as follows:

$$\bar{Z}_n = p_D \bar{Z}_{n-1} + \alpha_D (\bar{E}_n - \bar{E}_{n-1}), \text{ for } n>0, \tag{141}$$

$$\bar{Z}_0 = \alpha_D \bar{E}_0. \tag{142}$$

Therefore, using (137), (141), and (142), the Laguerre-FDTD formulation for the electric flux density $\bar{D}_n$ in the Debye media can be calculated recursively without storing all previous solutions.

7.4.2 Lorentz model

The lorentz model is another commonly used mathematical model to account for the dispersion. The Nth-order Lorentz dispersion model is given by

$$\varepsilon(\omega) = \varepsilon_\infty + (\varepsilon_s - \varepsilon_\infty) \sum_{i=1}^{N} \frac{a_i \omega_i^2}{\omega_i^2 + 2j\omega\delta_i - \omega^2}, \tag{143}$$

78

where a_i is the pole amplitude, ω_i is the pole location, and δ_i is the damping factor. For simplicity, the case with $N = 1$ is discussed in this section. The frequency-domain susceptibility function for the Lorentz model is

$$\chi(\omega) = (\varepsilon_s - \varepsilon_\infty) \frac{a\omega_0^2}{\omega_0^2 + 2j\omega\delta - \omega^2}, \tag{144}$$

where a is the pole amplitude, ω_0 is the pole location, and δ is the damping factor. The susceptibility in the time domain is obtained from (144) as follows:

$$\chi(t) = \frac{(\varepsilon_s - \varepsilon_\infty)a\omega_0^2}{\sqrt{\omega_0^2 - \delta^2}} \, e^{-\delta t} \sin\left(\sqrt{\omega_0^2 - \delta^2}\right) U(t). \tag{145}$$

Introducing complex numbers, (145) can be rewritten as

$$\chi(t) = \mathrm{Im}\left(\frac{(\varepsilon_s - \varepsilon_\infty)a\omega_0^2}{\sqrt{\omega_0^2 - \delta^2}} e^{-\left(\delta - j\sqrt{\omega_0^2 - \delta^2}\right)t}\right) U(t). \tag{146}$$

where $\mathrm{Im}(\cdot)$ represents the imaginary part of a complex number.

Transforming (146) to the Laguerre domain, we have

$$\chi_i = \mathrm{Im}(a_L p_L^i), \tag{147}$$

where

$$\alpha_L = \frac{(\varepsilon_s - \varepsilon_\infty)a\omega_0^2}{\sqrt{\omega_0^2 - \delta^2}} \frac{2}{2(\delta - j\sqrt{\omega_0^2 - \delta^2}) + s}, \tag{148}$$

$$p_L = \frac{2(\delta - j\sqrt{\omega_0^2 - \delta^2}) - s}{2(\delta - j\sqrt{\omega_0^2 - \delta^2}) + s}. \tag{149}$$

Equation (147) has the same form as (135) with different constants which are complex numbers. Therefore, similar to the Debye model, the electric flux density $\bar{D}_n$ in the Lorentz media also can

be calculated recursively as follows:

$$\bar{D}_n = \varepsilon_\infty \varepsilon_0 \bar{E}_n + \varepsilon_0 \mathrm{Im}(\bar{Z}_n), \tag{150}$$

where

$$\bar{Z}_n = p_L \bar{Z}_{n-1} + \alpha_L(\bar{E}_n - \bar{E}_{n-1}), \text{ for } n{>}0, \tag{151}$$

$$\bar{Z}_0 = \alpha_L \bar{E}_0. \tag{152}$$

7.5 Numerical Results

The proposed formulation is applied to an example containing a simple microstrip transmission line, as shown in Figure 47. Two ports are defined at both ends of the microstrip line whose length is 90 *mm* with conductor width and thickness of 3 *mm* and 10 *um*, respectively. Dielectric thickness is 200 *um*. The substrate material is FR-4 and it is assumed to be dispersive and modeled using a 1st order Debye model. Parameters for the Debye model are $\varepsilon_s{=}4.301$, $\varepsilon_\infty{=}4.096$, and $\tau{=}2.294{\cdot}10^{-11}$s [39].
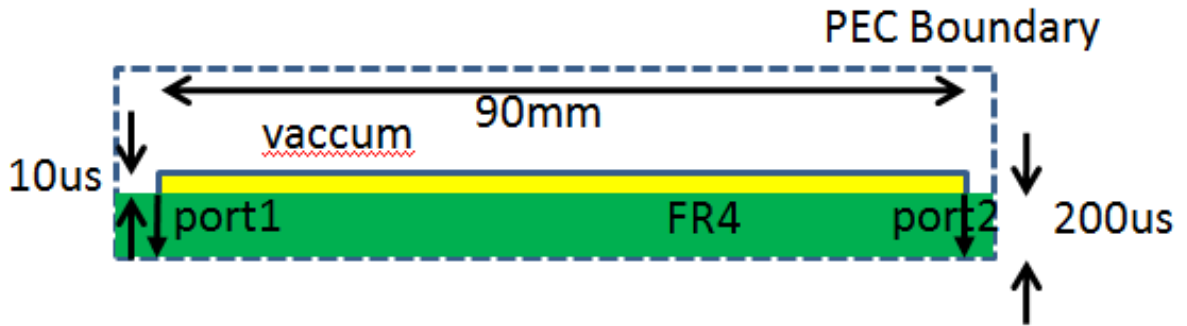
Figure 47. Test structure: Microstrip transmission line.

Thin conductor thickness results in very long simulation time of 11 hours using FDTD because of the small time step size of 33 *fs,* which comes from CFL limit determined by the smallest mesh size of 1 *mm* $\times$ 1 *mm* $\times$ 10 *us*. However, Laguerre-FDTD could be used to solve the same structure in 8 minutes on the same computer. In this example, Laguerre-FDTD showed

$80\times$ speed up over FDTD. The simulated time-domain waveforms of the electric field at the ports show very good agreement between FDTD and Laguerre-FDTD, as shown in Figure 48.

Contrary to 1.3GB of memory consumption when the general Laguerre-FDTD formulation for dispersion is used, the customized Debye formulation consumes 730MB as shown in Table 2.

Table 2. Memory consumption of general and customized formulation for Debye model.

	Memory Consumption
General formulation	1.3GB
Customized formulation for Debye model	730MB

To see the effect of material's dispersion on the transient response, the same structure has been simulated without the frequency-dependent dispersive material property using a frequency-independent permittivity of 4.301 with no loss. Figure 49 shows the time-domain waveform variation as the material property changes from dispersive to non-dispersive.
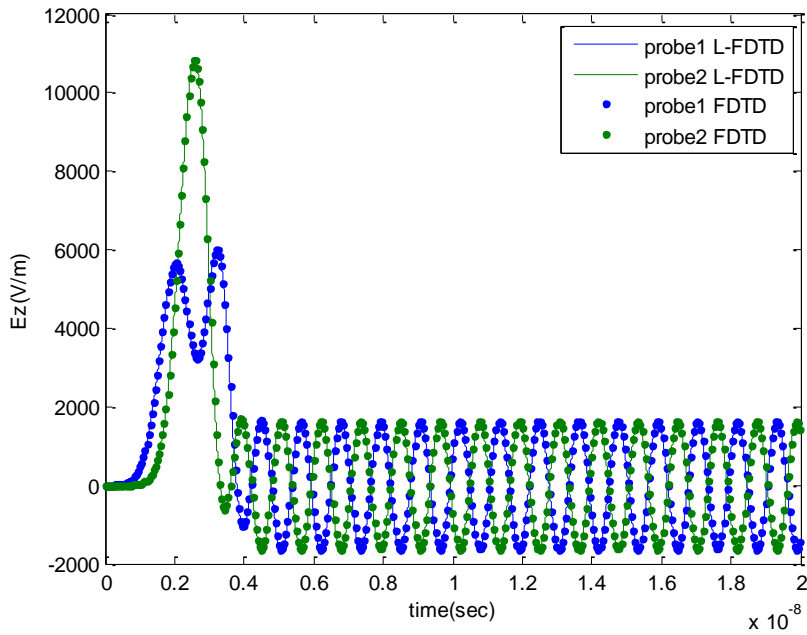
Figure 48. Simulated time-domain waveforms.
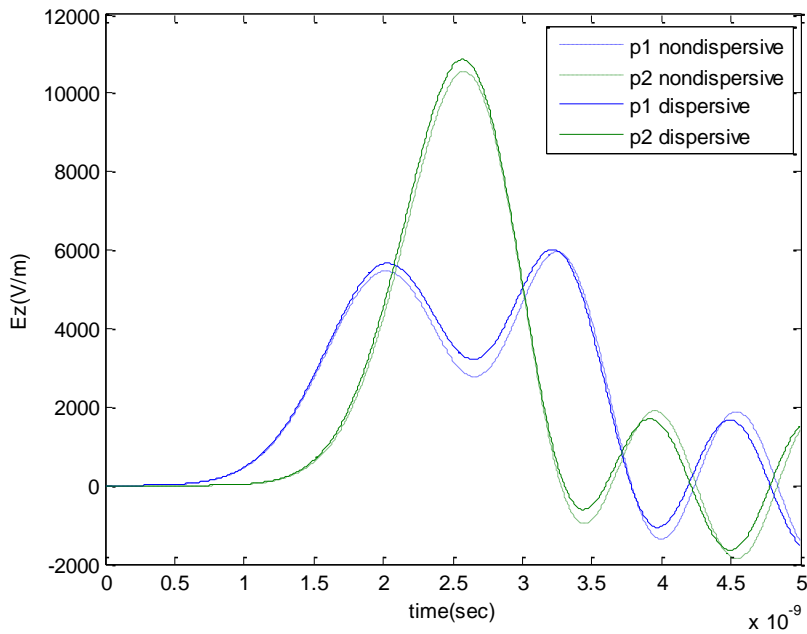
Figure 49. Comparison between simulated time-domain waveforms with dispersive and non-dispersive FR-4 model.

82

7.6 Summary

A Laguerre-FDTD formulation for frequency-dependent dispersive materials has been presented and has been improved in terms of memory efficiency for Debye and Lorentz media. Enabling recursive calculation of the electric flux density, the proposed formulation avoids storing all previous solutions which leads to significantly reduced memory consumption. The proposed formulation has been verified using a test example. Simulation results show that Laguerre-FDTD with the proposed formulation solves the example structure with dispersive material properties more efficiently than the general Laguerre-FDTD dispersion formulation in terms of memory while maintaining the accuracy.

CHAPTER VIII

TEST CASES

To increase 3-D integration density, TSV interconnections are emerging as major interconnection elements. Through fabrication in silicon substrate, TSV interconnections reduce interconnection pitch compared to bonding wires. In addition, the direct vertical connection by TSVs shortens electrical length, especially for communication between stacked chips. With these features, the use of TSV interconnections can be extended to various integrated mixed-signal system designs.

However, full-wave analysis of the TSV interconnections is challenging. The challenge comes from thin oxide region around relatively thick and long conductor of the TSV. Due to the CFL condition and thin oxide thickness, the time step in the conventional FDTD method needs to be very small when a given structure contains TSV. Laguerre-FDTD has an advantage in the simulation of such multiscale structures. Using the improvements of Laguerre-FDTD made in this thesis, 3-D multiscale structures containing TSVs can be solved efficiently and accurately, as shown in the following sections. In addition, non-multiscale structures have also been simulated and correlated with measurement. All simulations in this chapter have been done on a 64-bit machine with a 12 core Intel Xeon CPU and 48 GB RAM.

8.1 TSV Array

Usually, TSV interconnections are fabricated as an array in a silicon carrier and stacked vertically to construct a system-in-package (SiP). Therefore, a TSV array is a basic structure in 3-D integrated systems and needs to be well-analyzed. In this section, a 3-by-3 TSV array is analyzed in the frequency domain to compute S parameters using the Laguerre-FDTD method and the problem has been extended to a 5-by-5 array to show scalability. Comparison of the

simulation results of the 3-by-3 TSV array with results from a commercial solver shows good correlation, which confirms the accuracy of the Laguerre-FDTD.

8.1.1 3-by-3 TSV Array

The first test case is a 3-by-3 TSV array. A single-layered 3-by-3 TSV array is embedded into a silicon substrate with dielectric constant and conductivity of 11.9 and 10 S/m, respectively. TSV's copper diameter is 30 *um* with oxide thickness of 0.1 *um*. TSV's length is 100 *um*. TSVs are separated from adjacent TSVs by 30 *um* in the array, as shown in Figure 50. The TSV array structure is enclosed by a PEC boundary. 18 ports are defined between the ends of each TSV and the closest PEC boundary, as shown in Figure 51. From TSV's oxide thickness of 0.1 *um* to TSV's length of 100 *um*, the scale difference is 1:1000. The structure is discretized into 104 × 104 × 15 = 162,240 cells as shown in Figure 51. The cell dimension varies from 0.1 *um* to 5 *um* in the x and y directions. The cell dimension in the z direction is fixed at 20 *um*. TSV's circular cross-section is discretized into 24 × 24 cells using a rectangular mesh, as shown in Figure 52. S parameters are calculated from a set of time-domain simulations for 20 *ns* using the Laguerre-FDTD method.
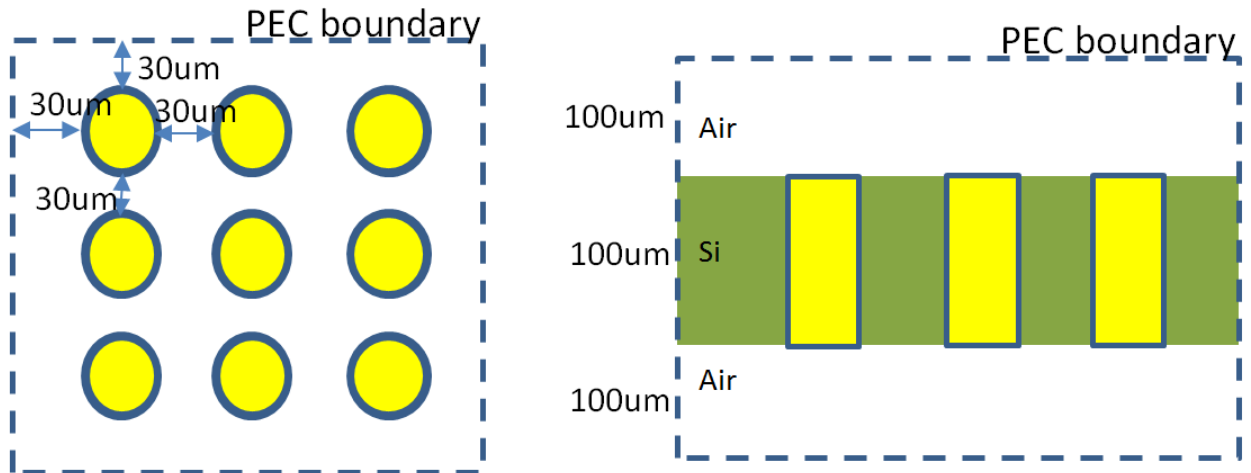
Figure 50. 3-by-3 TSV array. (left: top view, right: side cross-sectional view)
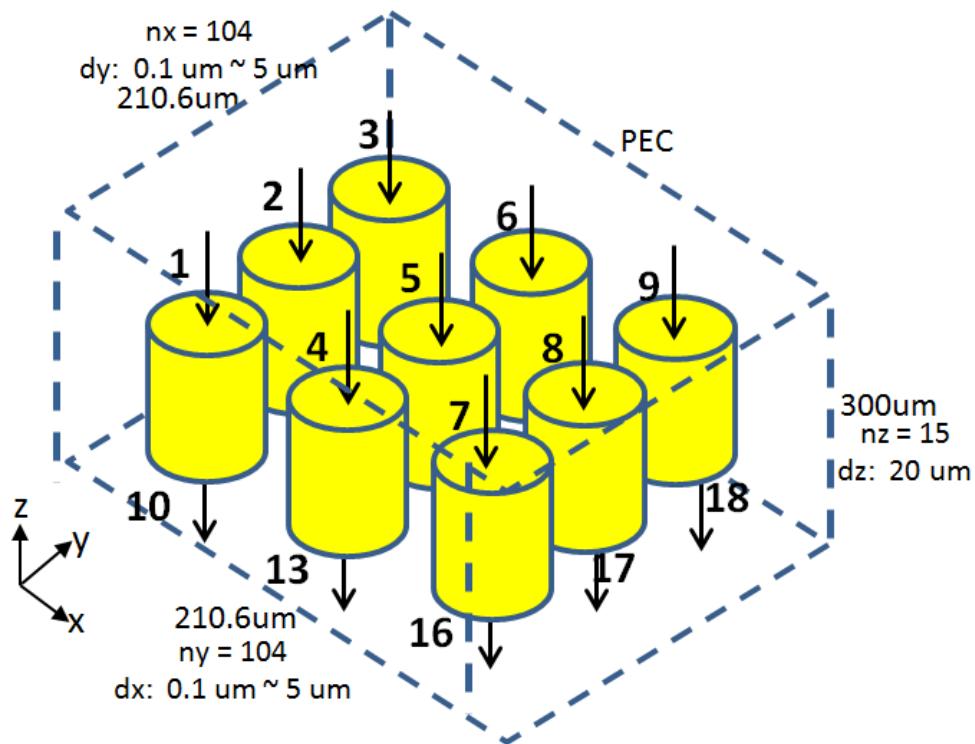
Figure 51. Ports definition on TSV array.
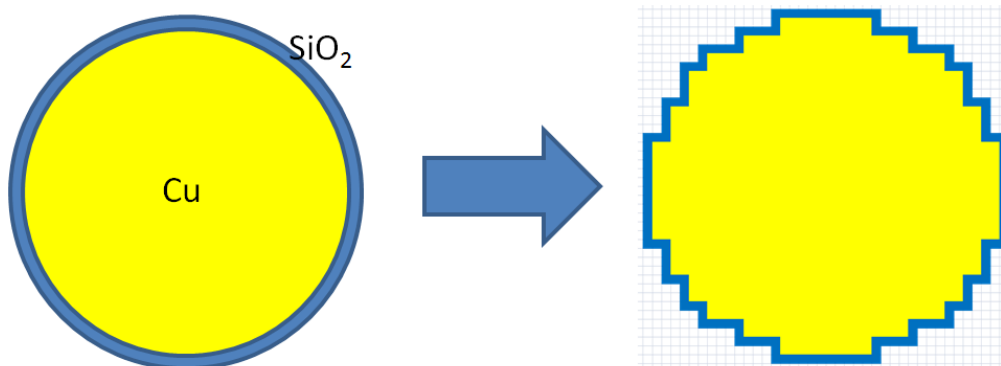
Figure 52. Discretization of circular cross section of TSV.

Some of the calculated S parameters using Laguerre-FDTD are plotted with S parameters calculated using a commercial solver [41] in Figure 53. Excellent correlation is shown between the Laguerre-FDTD and the commercial solver in Figure 53. For calculation of 18-port S

86

parameters, 18 time-domain simulations are required, with a separate source current excited at each of the 18 ports. For each time-domain simulation, it takes 19 minutes to finish the simulation using only one core of the multicore CPU and a memory consumption of 4.8 GB. Therefore, total $18 \times 19 = 342$ minutes are required to perform frequency-domain analysis. On the other hand, the commercial solver consumed 260 minutes and 3.5 GB of memory to calculate the 18-port S parameters using four cores.

18 time-domain simulations using Laguerre-FDTD are independent of each other. Therefore, they can be parallelized utilizing multicore CPU. If the Laguerre-FDTD simulations are optimally parallelized, CPU time of 342 minutes using one core can be reduced to 85.5 minutes using 4 cores.
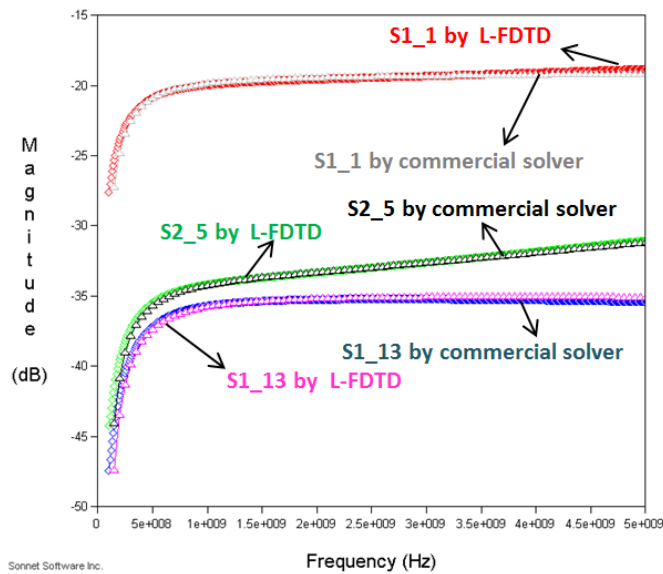
Figure 53. Calculated S parameters of 3-by-3 TSV array.

8.1.2 5-by-5 TSV Array

The TSV array structure in the previous subsection is extended to a 5-by-5 TSV array as shown in Figure 54. The top view and the cross-sectional view are similar to the previous

example's top and cross-sectional views shown in Figure 50. Dimensions of the structure are similar to the previous 3-by-3 TSV array example. TSV's copper diameter and length are 30 *um* and 100 *um*, respectively. Oxide thickness of the TSV is 0.1 *um*. Distance between adjacent TSVs is 30 *um*. The structure is enclosed by a PEC boundary. The structure is discretized into $164 \times 164 \times 15 = 403{,}440$ cells as shown in Figure 54. The Circular TSV geometry is discretized into 24×24 cells similar to the previous 3-by-3 TSV array example, as shown in Figure 52. 50 ports were defined at each end of the TSV, as shown in Figure 54.
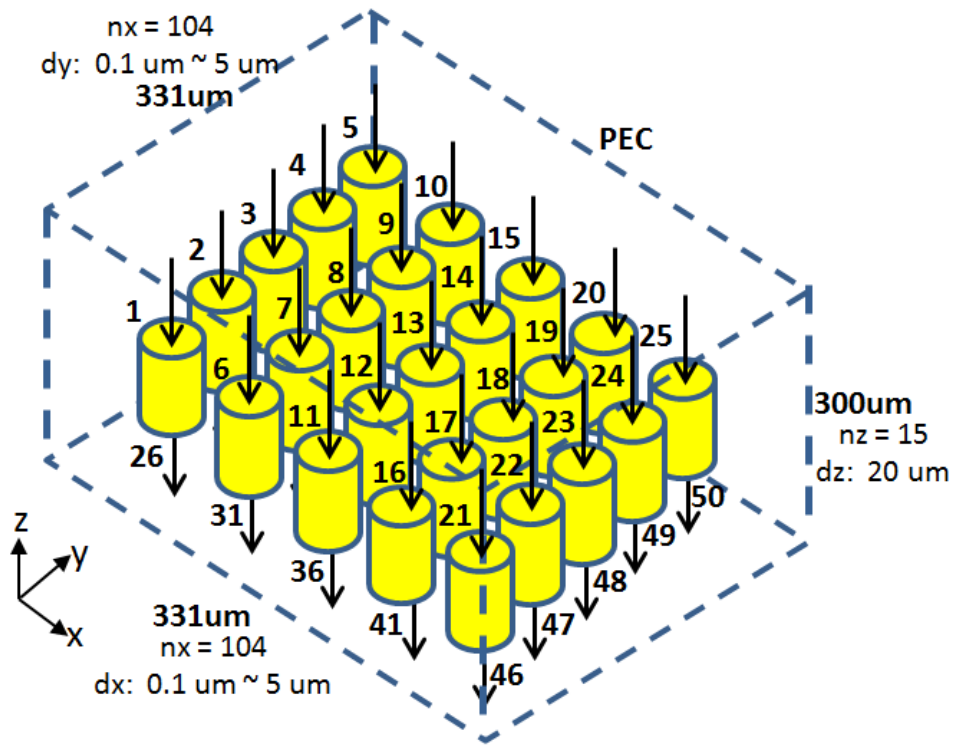
Figure 54. 5-by-5 TSV array.

Figure 55 shows calculated S parameters. For the calculation of 50-port S parameters, 50 time-domain simulations are required to excite all 50 ports. It takes 90 minutes and 10.5 GB to perform one time-domain simulation. Therefore, $50 \times 90 = 4500$ minutes are required to perform all 50 time-domain simulations. However, using the symmetry of the structure, only 6 time-

domain simulations can represent 50 time-domain simulations, as shown in Figure 56. Time-domain simulations with excited TSVs marked by the same number can be reduced to one representative time-domain simulation. For example, from the structure's symmetry, S11_1 is the same as S3_1, S3_5, S15_5, S11_21, S23_21, S23_25, and S15_25. Therefore, time-domain simulations with a current source at Port 5, 21, and 25 can be derived from a time-domain simulation with current source at Port 1 by re-ordering ports.
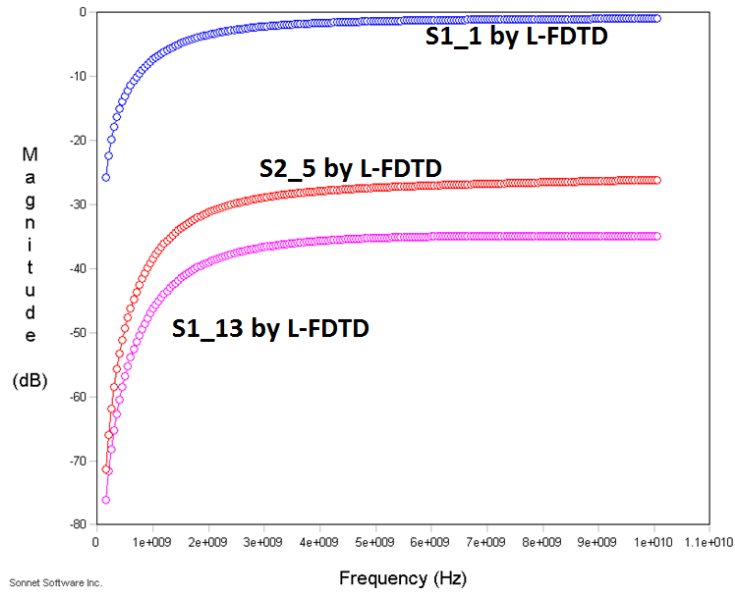
Figure 55. Calculated S parameters of 5-by-5 TSV array.
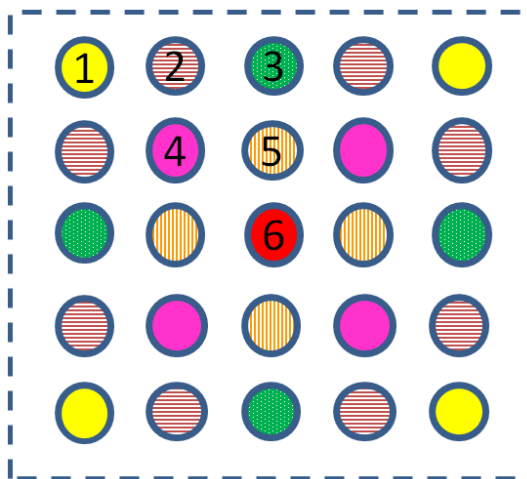
Figure 56. Categorization of TSVs in 5-by-5 TSV array using symmetry.

Unfortunately, the commercial solver [41] was not able to solve the 5-by-5 TSV array example on the machine with 48 GB RAM because of insufficient memory. Therefore, comparison of the calculated S parameters using Laguerre-FDTD with the commercial solver was not possible.

8.2 TSV-TSV Coupling

TSV noise coupling is expected to be a major concern for 3D-IC system design. With TSV coupled noise, the system noise reliability decreases, RF sensitivity decreases, and the bit error rate (BER) of a high-speed signal increases. To protect sensitive active circuits from TSV coupling noise, it is important to estimate the noise transfer function between the TSVs. In [42], a test vehicle for TSV-TSV coupling has been fabricated and coupling between TSVs has been measured in the time domain. In this section, the test vehicle for TSV-TSV coupling is analyzed using the Laguerre-FDTD and compared with the measurement data in [42], which ensures the accuracy of the Laguerre-FDTD method for this example.

Figure 57 illustrates the structure of the TSV-TSV coupling test vehicle. Conductor material for TSV and RDL is copper whose conductivity is 5.69e7 S/m. Oxide thickness of the TSV is 0.52 *um* while the diameter of the TSV conductor is 33 *um*. The structure is enclosed by a PEC boundary with 100 *um* margin between the structure and boundary in each direction in the Laguerre-FDTD simulation. The structure is discretized into $94 \times 94 \times 19 = 167,884$ cells as shown in Figure 58. Similar to the TSV array cases, the circular TSV cross-section is discretized into 24×24 cells, as shown in Figure 52.
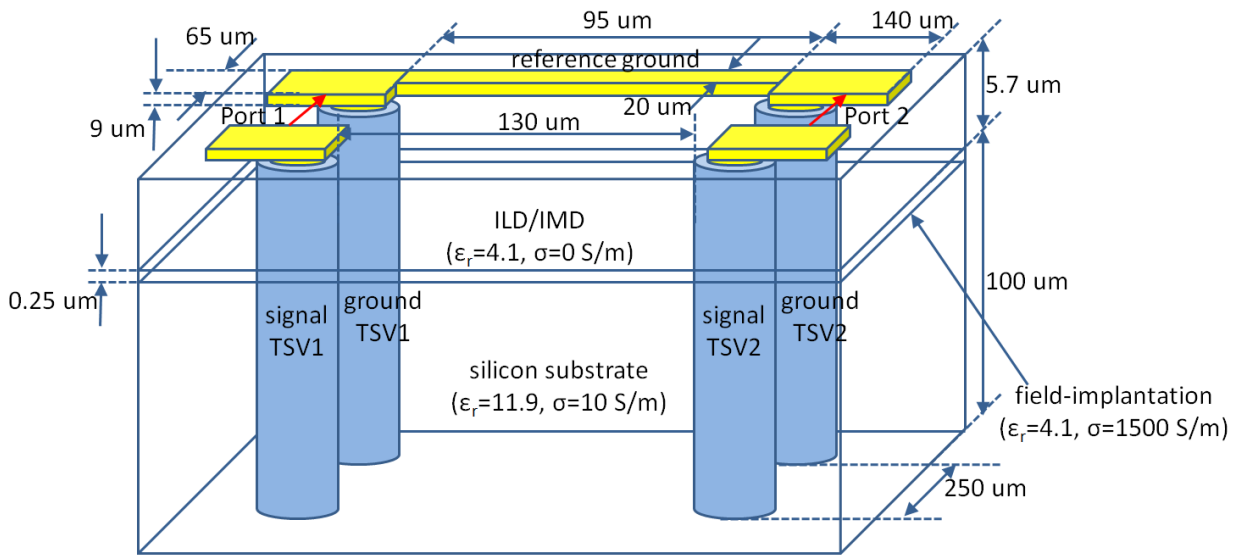
Figure 57. TSV-TSV coupling test vehicle.
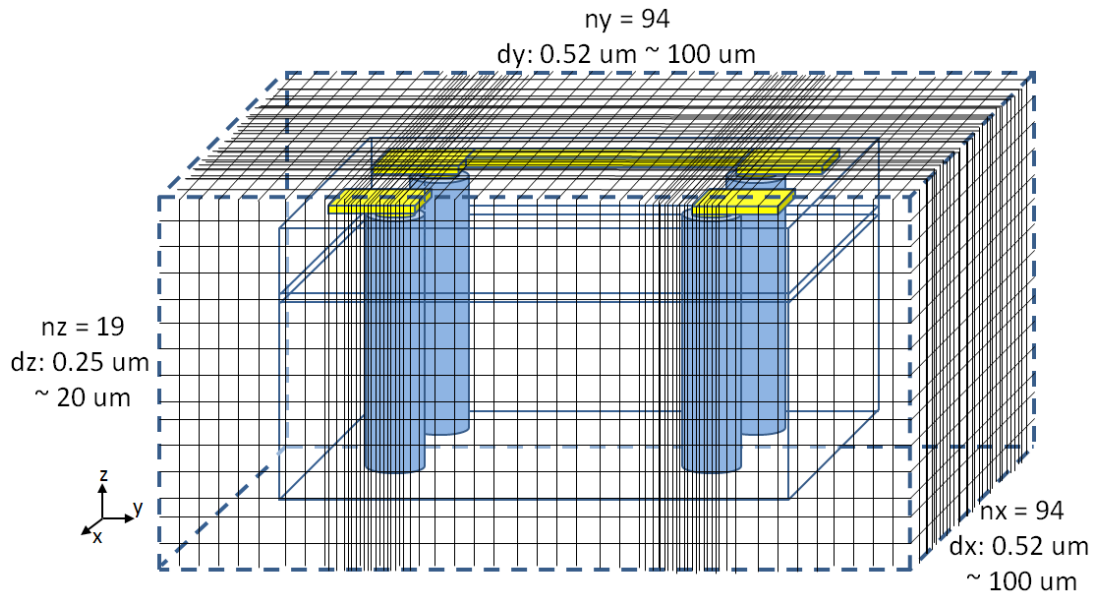
Figure 58. Meshing of test vehicle.

A rectangular clock signal, which switches between 0 and 1 V with a rising/falling time of 40 *ps* and source resistance of 50 Ω, is injected into Port 1. The measurements have been performed with the source at Port 1 with clock frequency of 100 MHz and 10 GHz.

Laguerre-FDTD simulation of the structure took 24 minutes and 5.3 GB of RAM. S parameters were calculated from the Laguerre-FDTD simulation. Since a voltage source with a source impedance is not implemented in the Laguerre-FDTD code, transient responses could not be directly calculated using the Laguerre-FDTD. Therefore, S parameters of the structure were extracted using the Laguerre-FDTD. 4 ports are defined in the S parameter calculation between each TSV's end and PEC boundary. Transient responses were calculated in ADS [43] using the extracted 4-port S parameters, as shown in Figure 59 and Figure 60. Calculated transient responses at Port 2 for clock's frequency of 100 MHz and 10 GHz are shown in Figure 61. Compared to the measured data, results using Laguerre-FDTD show good correlation.
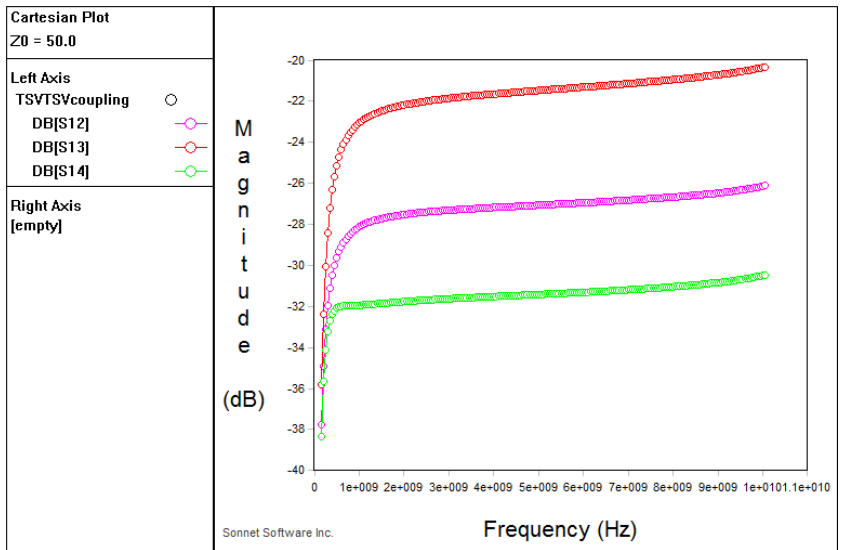
Figure 59. Calculated S parameters
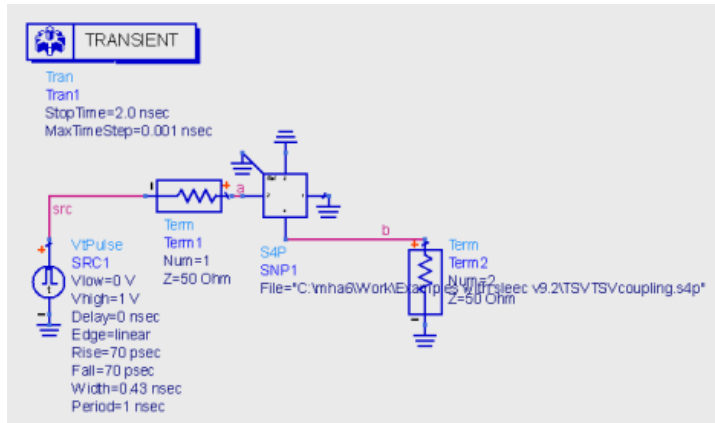
Figure 60. Simulation setup in ADS.

100MHz Clock 1GHz Clock
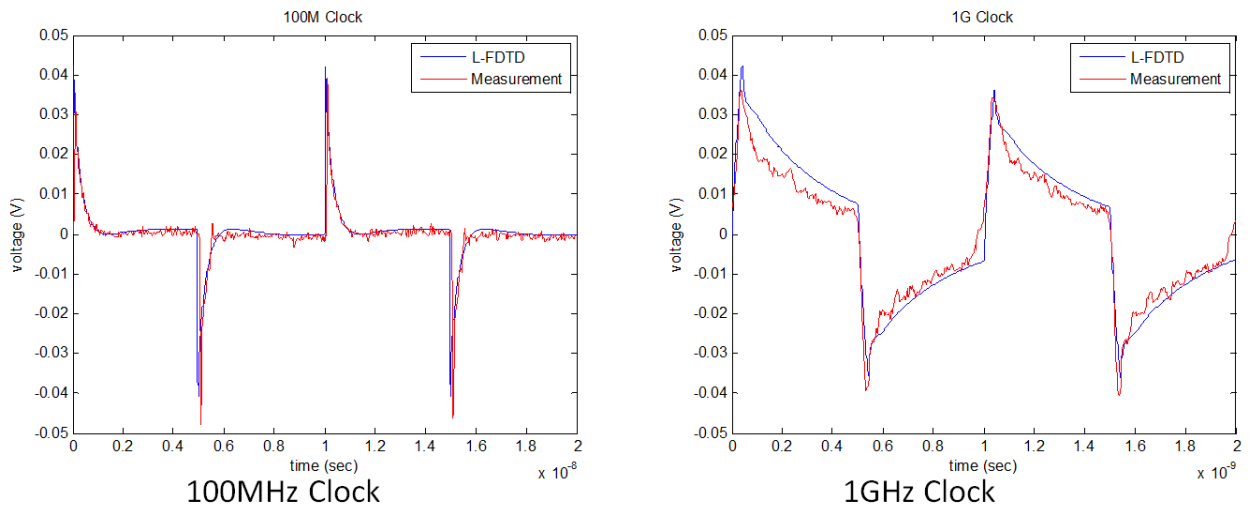
Figure 61. Coupled noise at Port 2. (left: 100 MHz clock, right: 1 GHz clock)

8.3 Microstrip Line with Return Path Discontinuity

Microstrip lines are key components to transmit high speed signals in electronic systems. Therefore, the propagation characteristics of the microstrip line structures need to be carefully studied and investigated. For model-to-hardware correlation, microstrip line structures are fabricated, measured, and compared with the Laguerre-FDTD simulation. Since dielectric material is not ideal, accurate modeling of dielectric material's dispersion is essential to obtain good correlation to measurements.

In this section, three microstrip line structures are simulated and compared with the measurements. This structure's physical dimensions are not small enough for Laguerre-FDTD to show the advantage in the simulation time over the conventional FDTD method. Therefore, the main purpose of the test cases in this section is to show model-to-hardware correlation and prove the accuracy of modeling using the Laguerre-FDTD method.

94

8.3.1 Simple Microstrip Line

Figure 62 and Figure 63 show the cross-sectional side view and top view of the test case, respectively. The structure has 4 metal layers. The microstrip transmission line is located on the top layer, while the second layer is a solid ground plane. The dielectric material is FR-4 whose relative dielectric constant is 4.5 and loss tangent is 0.025. The conductor material is copper whose conductivity is 5.69e7 S/m. GSG500 microprobes have been used in the measurement.

In the Laguerre-FDTD simulation, the structure is surrounded by a PEC boundary with a 5 *mm* margin between the structure and the boundary in each direction, and is discretized into 29 × 79 × 23 = 52,693 cells, as shown in Figure 64. The smallest and the largest mesh sizes in lateral direction are 0.17 *mm* and 1.5 *mm,* respectively. The scale difference is 1:3200 (from 30 *um* conductor thickness to 95.5 *mm* transmission line length). Ports are defined at both ends of the transmission line.
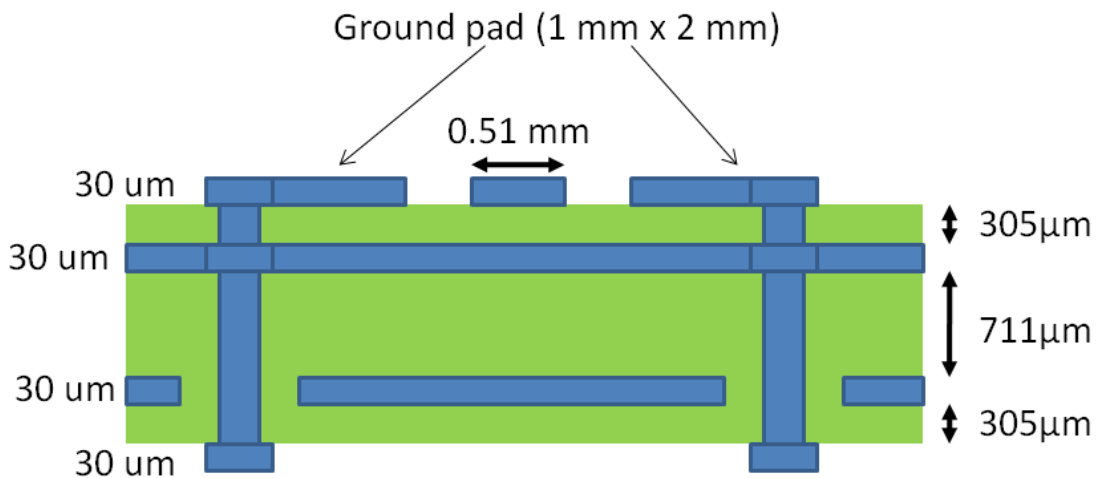
Figure 62. Side cross-sectional view of microstrip line test case.
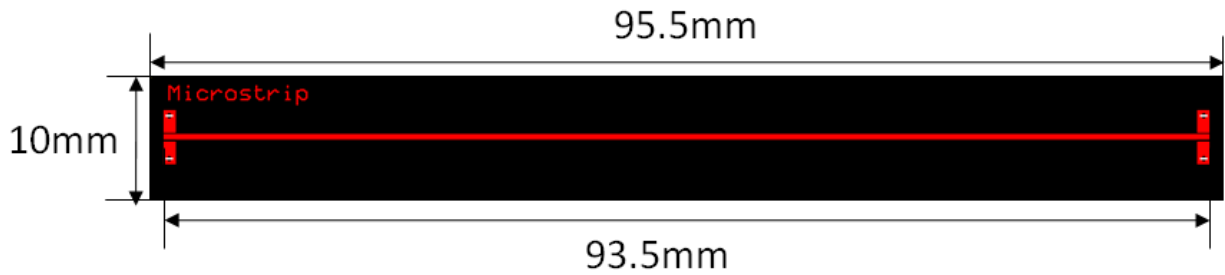
Figure 63. Top view of microstrip line test case.
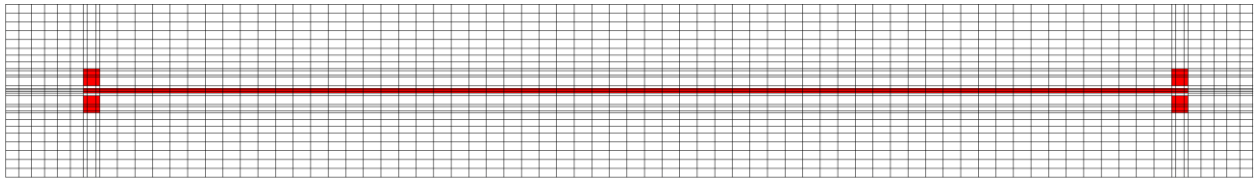
Figure 64. Meshing of structure. (top view)

Time-domain simulation for 20 *ns* was performed to calculate the frequency-domain S parameters, which consumed 30 minutes CPU time and 1.2 GB of memory. The calculated insertion loss is plotted in Figure 65 with measurements, showing good correlation between them. Oscillations in the calculated insertion loss is due to interaction between the microstrip line structure and PEC boundary, which can be resolved by providing wider margin between the structure and PEC boundary.
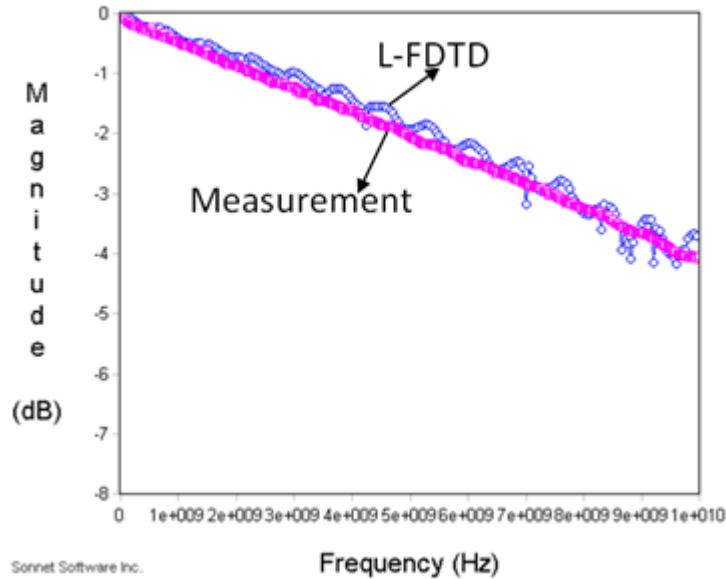
Figure 65. Calculated and measured insertion losses of microstrip-line test case.

8.3.2 Microstrip Line over Slot

This structure is similar to the previous test case. However, the ground plane at the second layer has a slot, as shown in Figure 66. The length and width of the slot are 30.5 *mm* and 4.81 *mm*, respectively. The structure is also enclosed by a PEC boundary with a 5 *mm* margin and discretized into $38 \times 135 \times 23 = 117{,}990$ cells. The top view of the mesh is shown in Figure 67. The smallest and largest lateral mesh sizes are 0.17 *mm* and 2 *mm,* respectively. The scale difference is the same as the previous test case 1:3200, which is from 30 *um* conductor thickness to 95.5 *mm* transmission line length. For 20 *ns* simulation, 3.4 GB of memory and 70 minutes of CPU time were required using the Laguerre-FDTD approach. The calculated insertion loss is shown in Figure 68 and compared with the measured insertion loss. Reasonably good agreement between the Laguerre-FDTD simulation and the measurement is observed.
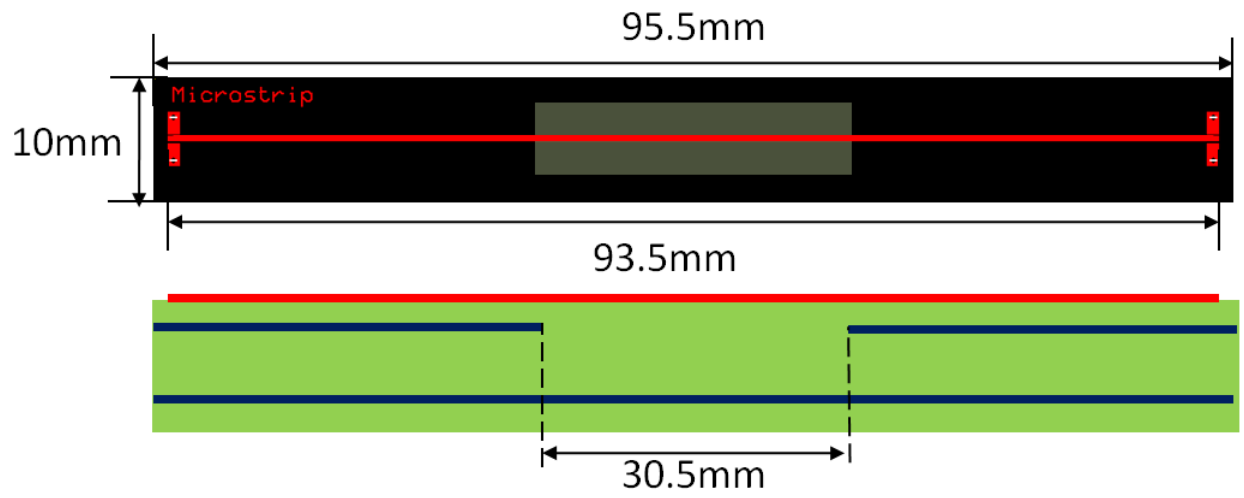
Figure 66. Top view (top) and side cross-sectional view (bottom) of test case.
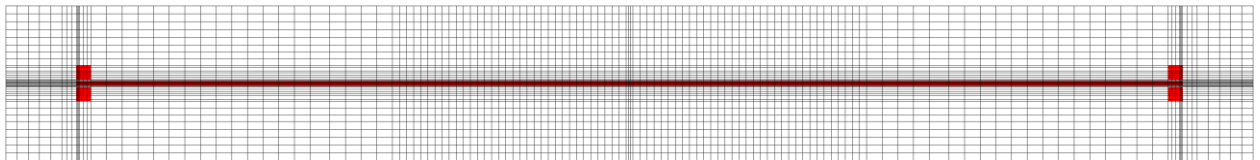
Figure 67. Meshing of structure. (top view)
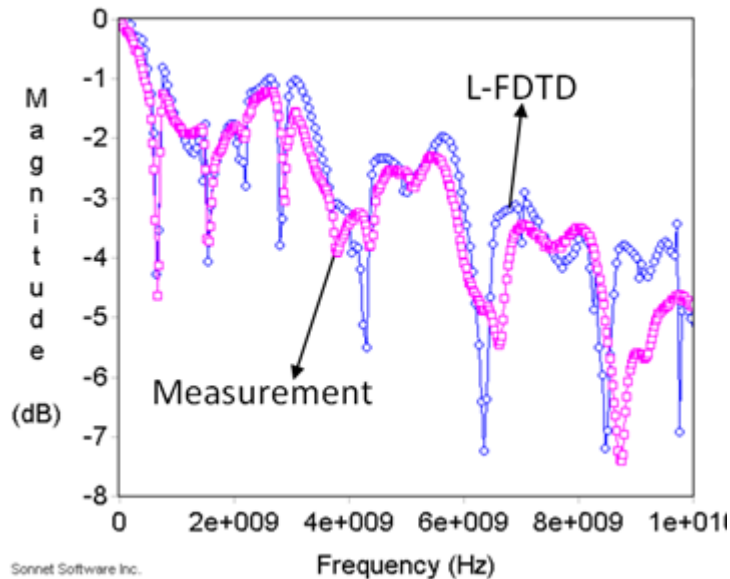
Figure 68. Calculated and measured insertion losses of the microstrip-line-over-a-slot test case.

8.3.3 Microstrip Line over Small Holes

This test case is also similar to the previous one. However, there are 10 small holes on the ground plane instead of a large slot, as shown in Figure 69. The holes have the same size of 0.76 $\times$ 0.76 *mm*. The spacing between holes is 2.54 *mm*. In the Laguerre-FDTD simulation, the structure is enclosed by a PEC boundary with a 5 *mm* margin, and is discretized into $37 \times 127 \times 23 = 108,077$ cells. The way the structure is discretized is shown in Figure 70. The smallest and largest lateral mesh sizes are 0.15 *mm* and 2 *mm,* respectively. The scale difference is the same as the previous test case 1:3200, which is from 30 *um* conductor thickness to 95.5 *mm* transmission line length, 1:3200.
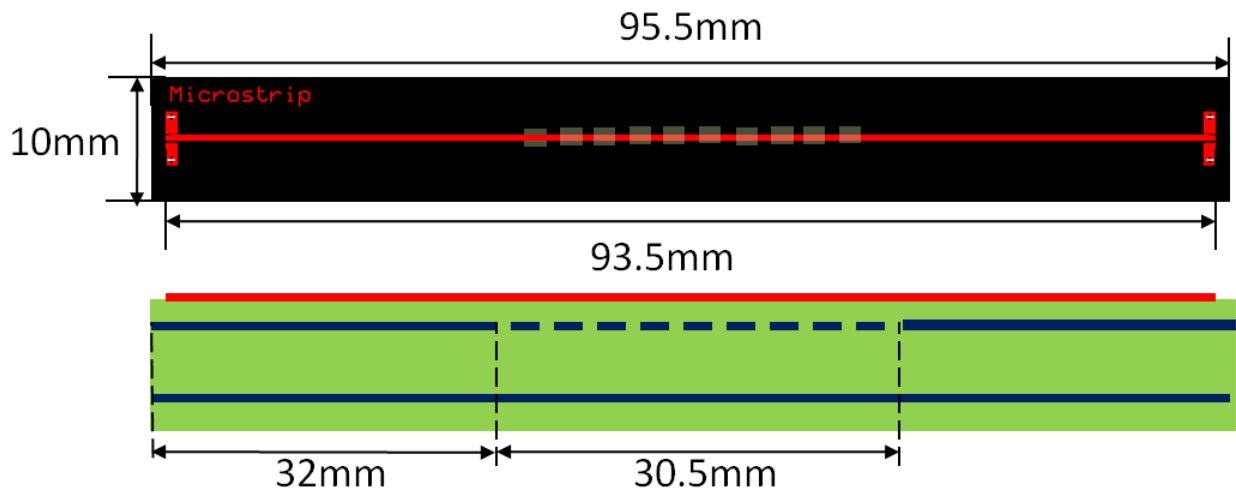
Figure 69. Top view (top) and side cross-sectional view (bottom) of test case.
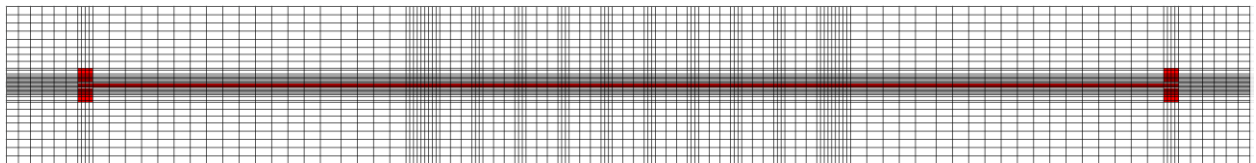
Figure 70. Meshing of structure. (top view)

It takes 3.1 GB of memory and 60 minutes of CPU time to solve the structure for 20 *ns* using the Laguerre-FDTD method. From the time-domain simulation, frequency-domain S parameters can be calculated. The calculated insertion loss is shown in Figure 71. Both the simulated and the measured insertion loss show similar trend. However, the correlation does have discrepancy.
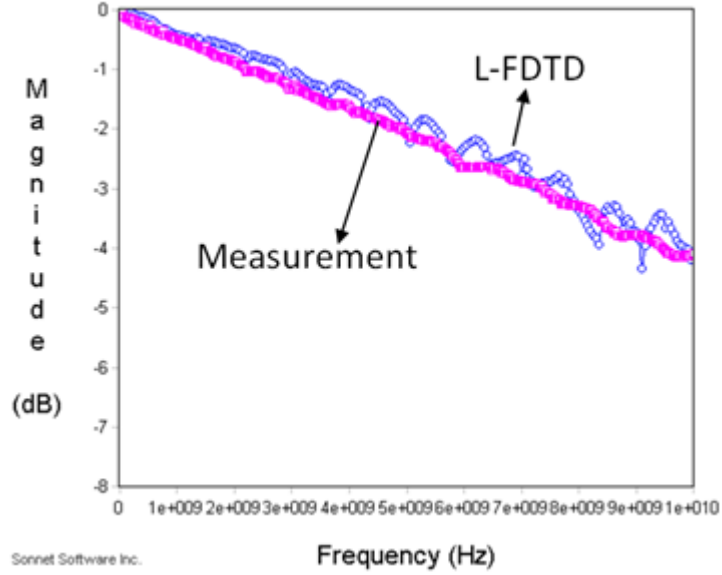
Figure 71. Calculated and measured insertion losses of microstrip-line-over-small-holes test case.

8.3.4 Importance of Modeling Dispersion

In real world, most dielectric materials are dispersive. Therefore, accurate modeling of dispersion is important to make model-to-hardware correlation. Test cases shown in this section contain dispersive FR-4 material. The effect of inaccurate modeling of dielectric loss is investigated using the test cases in this subsection.

The Debye model can represent frequency-dependent material effectively and is given by

$$\varepsilon(\omega) = \varepsilon_\infty + (\varepsilon_s - \varepsilon_\infty) \sum_{i=1}^{N} \frac{a_i}{1 + j\omega\tau_i}, \tag{153}$$

where a_i and τ_i represent the strength and time constants of various relaxation processes, ε_s is the static permittivity, and ε_∞ is the permittivity at infinite frequency. To obtain constant loss tangent for wide range of frequency, the order of Debye model N needs to be sufficiently large. The frequency range of interest in the test cases of this section is from 50 MHz to 10 GHz. FR-

101

4's loss tangent is given as 0.025 in these test cases. The Debye model with $N = 1$ cannot provide constant loss tangent over the frequency range of interest, as shown in Figure 72.
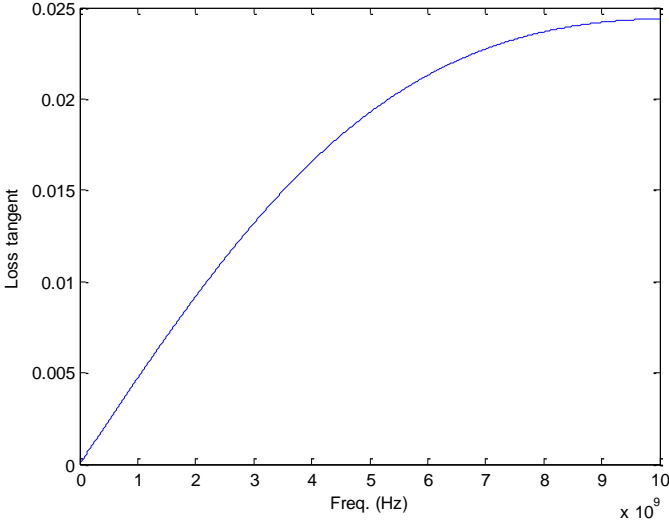
Figure 72. 1st order Debye model for tan δ = 0.025 at 10GHz

Using a 4th order Debye model ($N = 4$), almost constant loss tangent can be obtained for the frequency range of interest as shown in Figure 73.
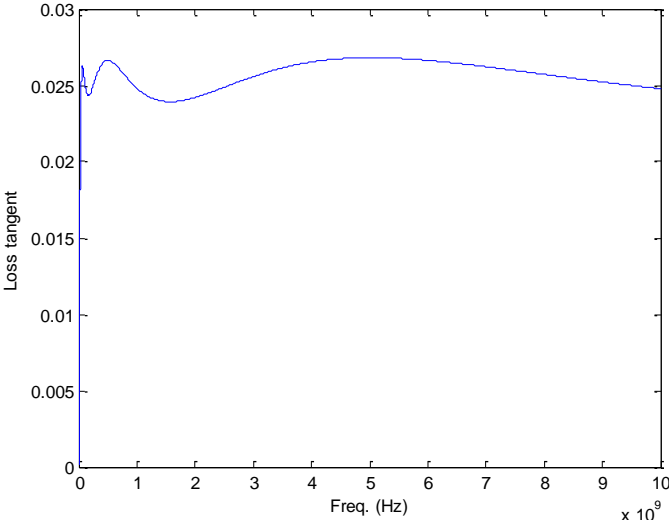
Figure 73. 4th order Debye model for tan δ = 0.025 at 50MHz ~ 10GHz

102

Differences in calculated S parameters using a 1st order Debye model and a 4th order Debye model for microstrip line structures tested in this section are shown in Figure 74 - Figure 76. The simple microstrip line shown in Figure 63 has no return path discontinuity, and the microstrip line over small holes shown in Figure 69 does not have severe return path discontinuity. Therefore, insertion loss is mainly determined by the material's loss. Consequently, an inaccurate modeling of FR-4's dispersive property worsens the accuracy of the calculated insertion loss for the test cases as shown in Figure 74 and Figure 76, where deviations between measurement and calculated insertion loss using the 1st order Debye model are more than 1 dB. Therefore, the effective modeling of dispersion is important for obtaining accuracy. In the case of the microstrip line over a slot, as shown in Figure 75, the effect of inaccuracy in the loss tangent modeling is not as obvious as other test cases with no and little return path discontinuity. It is because the insertion loss of the structure is dominated by the geometry of the structure, due to its return path discontinuity.
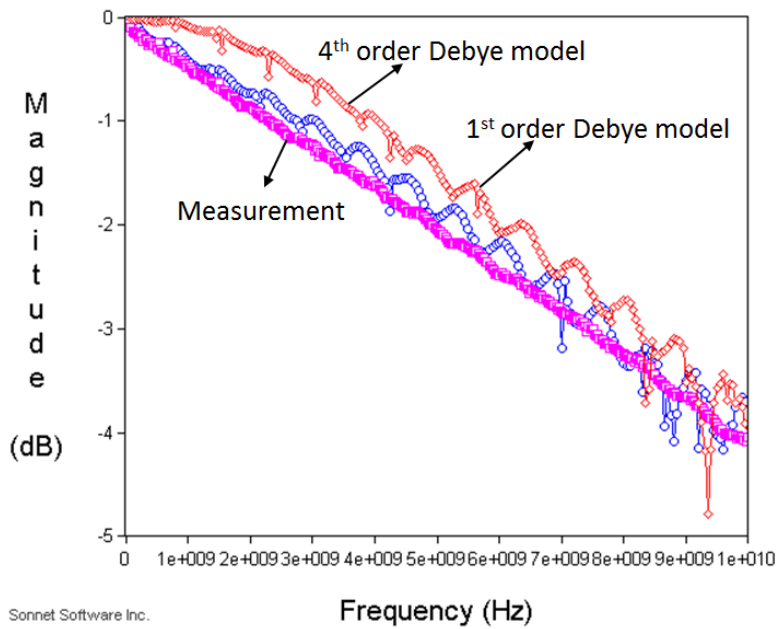
Figure 74. Insertion of loss of simple microstrip line using a 1st order Debye model and a 4th order Debye model.
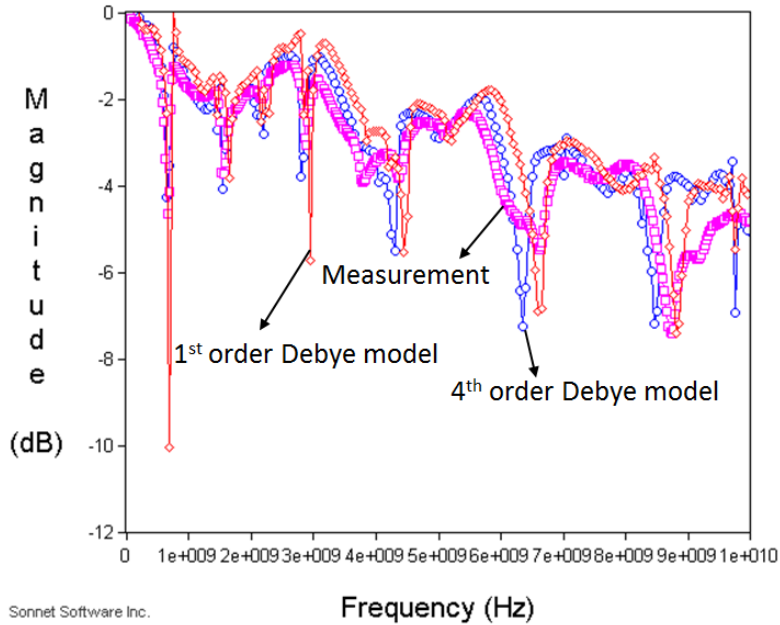
Figure 75. Insertion of loss of microstrip line over a slot using a 1st order Debye model and a 4th order Debye model.
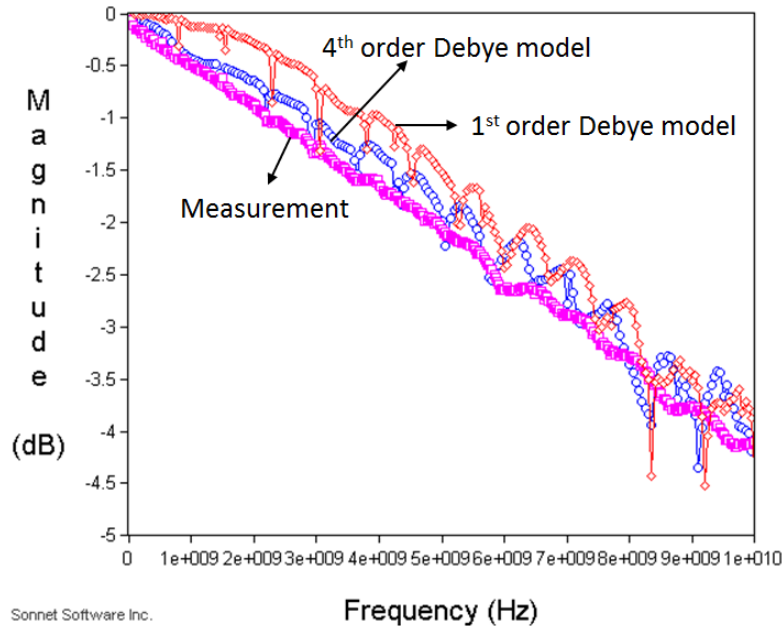
Figure 76. Insertion of loss of microstrip line over small holes using a 1st order Debye model and a 4th order Debye model.

8.4 Microstrip Line with TSV on Silicon Carrier

As stated in the previous section, a microstrip transmission line is a key component for transmitting high-speed signals in electronic systems. As 3-D integration using TSV interconnections emerges, microstrip lines with TSV interconnections on a silicon carrier also need to be analyzed. Due to oxide's very thin thickness compared to TSV's diameter and length, microstrip lines with TSVs are challenging structures to be analyzed using the conventional FDTD method because of the CFL limit, whereas Laguerre-FDTD is advantageous in the simulation of such multiscale structures.

8.4.1 Microstrip Line with Return Path Discontinuity I

Figure 77 shows a front cross-sectional view and a top view of the test case. The structure contains 4 metal layers. A microstrip line starts on the top layer with TSV transitions to the

bottom layer and from the bottom layer to the top layer. The second and third layers are not connected. Therefore, a return path discontinuity occurs at the TSV transition.
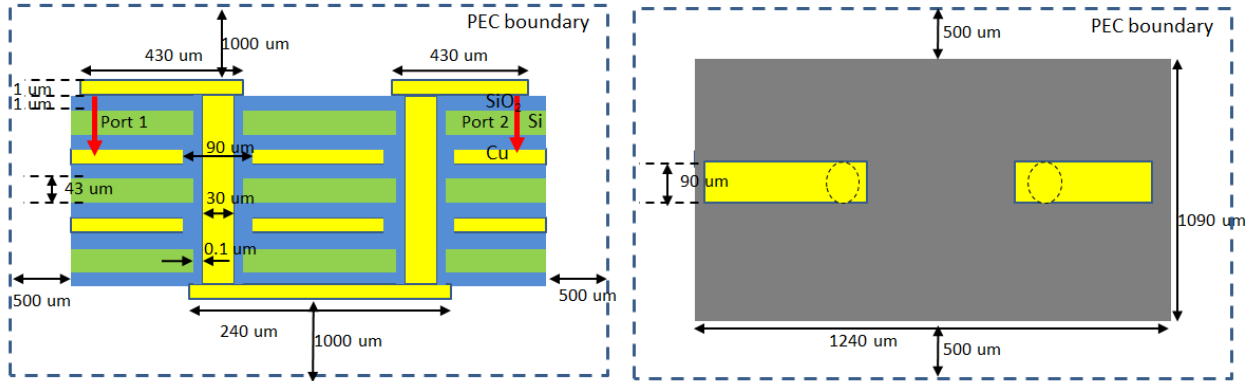
Figure 77. Front cross-sectional view and top view of test case.

The conductor material is copper whose conductivity is 5.69e7 S/m. Silicon's dielectric constant and conductivity are 11.9 and 10 S/m, respectively. The TSV's copper diameter is 30 um and its oxide thickness is 0.1 um. The metal layer's thickness is 1 um. The dielectric layer's thickness is 45 um which consists of 43 um of silicon and 1 um of oxide at the top and bottom of the dielectric layer to insulate the conductive silicon layer from conductors. From 0.1 um of TSV's oxide thickness to 430 um of transmission line's length on the top layer, the scale difference is 1:4300 in this structure. The structure is discretized into $104 \times 152 \times 29 = 458{,}432$ cells as shown in Figure 78. Due to TSV's circular geometry and thin oxide, the mesh for the region occupied by TSV is very fine, as small as 0.1 um. The circular geometry of the TSV is discretized into 24×24 cells as shown in Figure 79. Similar to the TSV array cases, the circular cross-section of the TSV is discretized into 24×24 cells as shown in Figure 52. Two ports are defined at both ends of the microstrip line. Transient simulation for 20 ns is performed to calculate S parameters using the Laguerre-FDTD method, which takes 150 minutes and 23 GB of RAM. If the structure was simulated using the conventional FDTD, because of CFL limit, the

time step needs to be as small as 0.16 *fs*, resulting in 268 days to solve the structure only for 20 *ns*. Memory consumption of FDTD is 38.4 MB. Therefore, Laguerre-FDTD shows 2500× faster simulation than the conventional FDTD in this test case while the memory consumption of the Laguerre-FDTD is 600× larger than FDTD.
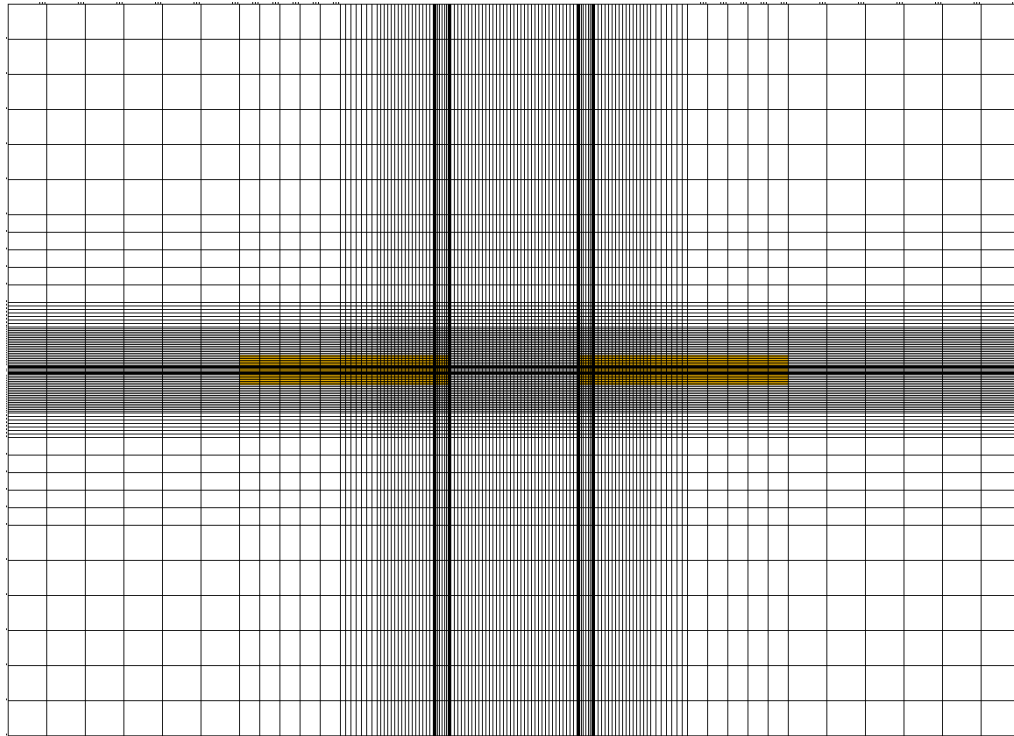
Figure 78. Meshing of structure. (top view)
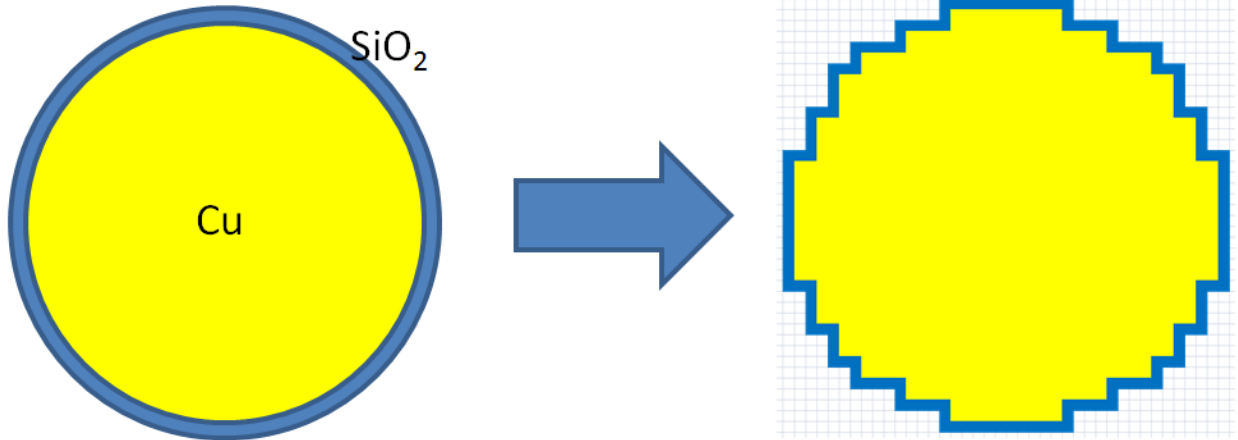
Figure 79. Discretization of circular cross section of TSV

Calculated insertion loss is shown in Figure 80. Unfortunately, the result cannot be compared since both FDTD method and commercial tools cannot solve the structure due to time and memory limitations, respectively.
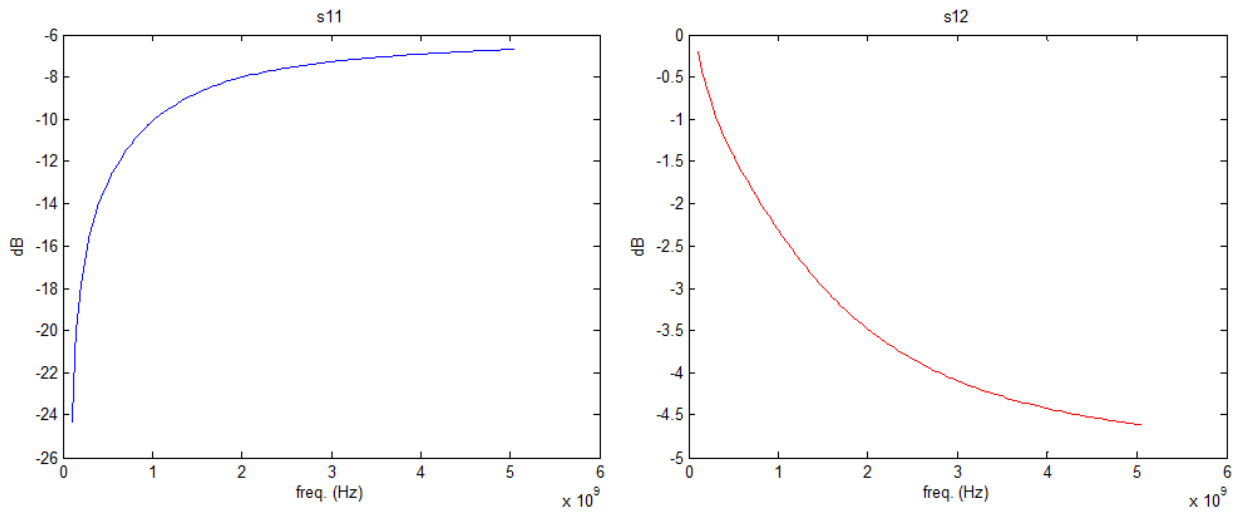
Figure 80. Calculated return loss (left) and insertion loss (right).

8.4.2 Microstrip Line with Return Path Discontinuity II

This test case is introduced in [44] and shown in Figure 81. The test case in this subsection is similar to the previous one in 8.4.1. The dimensions and composition of layers are different from the test structure in 8.4.1. Two ports are defined at both ends of microstrip line between microstrip line's conductor on the top layer and the solid plane on the second layer. The structure is discretized into $94 \times 263 \times 31 = 766,382$ cells. The lateral mesh is shown in Figure 82. As shown, the mesh near the TSV structures is very dense. The smallest mesh size is 1 *um*, and the largest mesh size is 800 *um*. The scale difference in this structure is from 1 um of TSV's oxide thickness to 20 *mm* of bottom layer's conductor's length, 1:20000. Laguerre-FDTD simulation of the structure takes 319 minutes and 44 GB of memory. If the structure were simulated using the conventional FDTD method, the estimated CPU time is 22 days, which is $100 \times$ longer than the Laguerre-FDTD. From the transient simulation using the Laguerre-FDTD method, S parameters can be calculated. The insertion loss is plotted in Figure 83 and compared to the result in [44], which is calculated using a commercial time-domain solver. Reasonably good agreement is observed in the comparison.
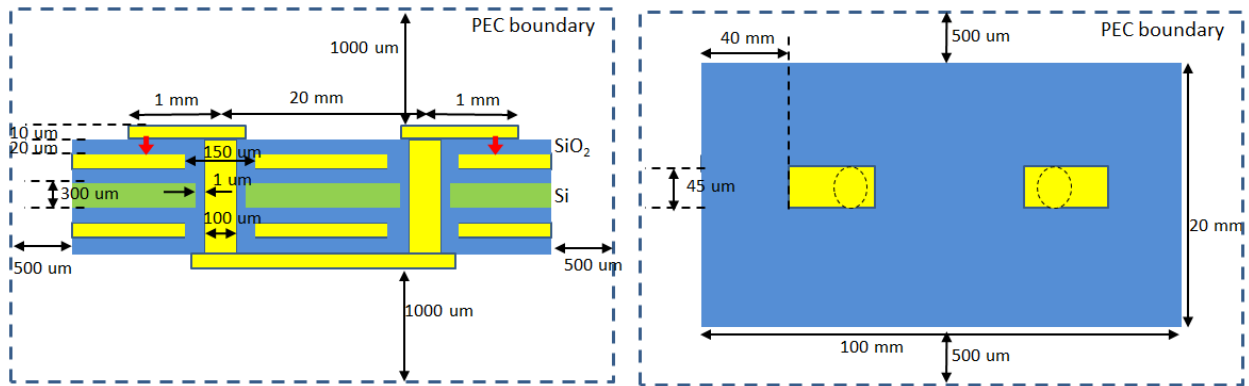
Figure 81. Front cross-sectional view and top view of test case.
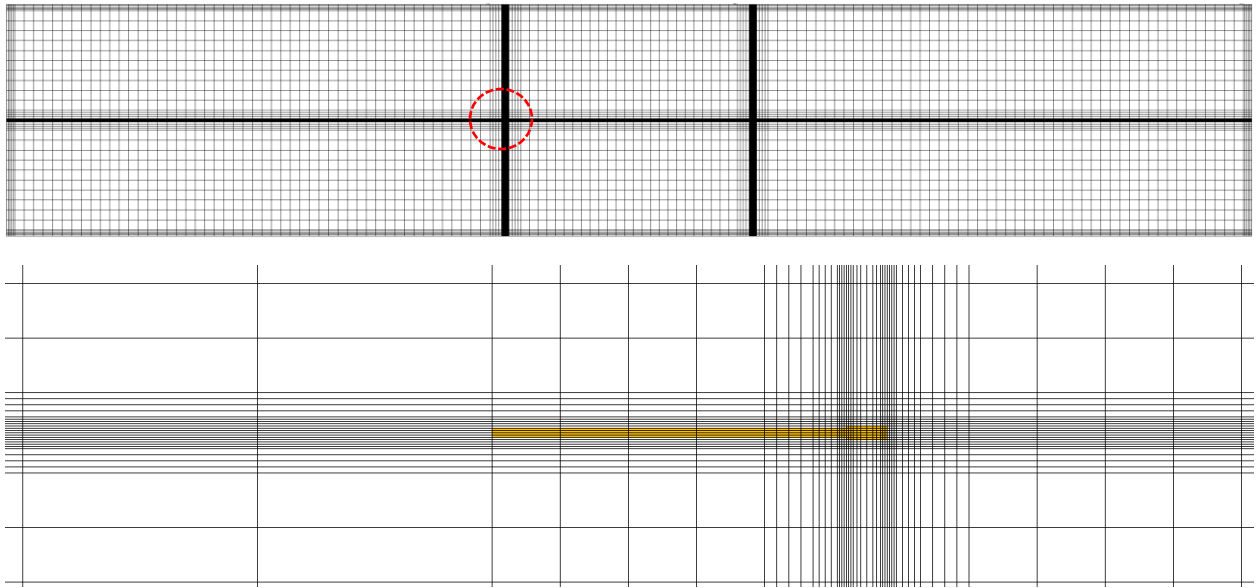
Figure 82. Meshing of structure.
(top: whole structure, bottom: enlarged view of red-circled area)
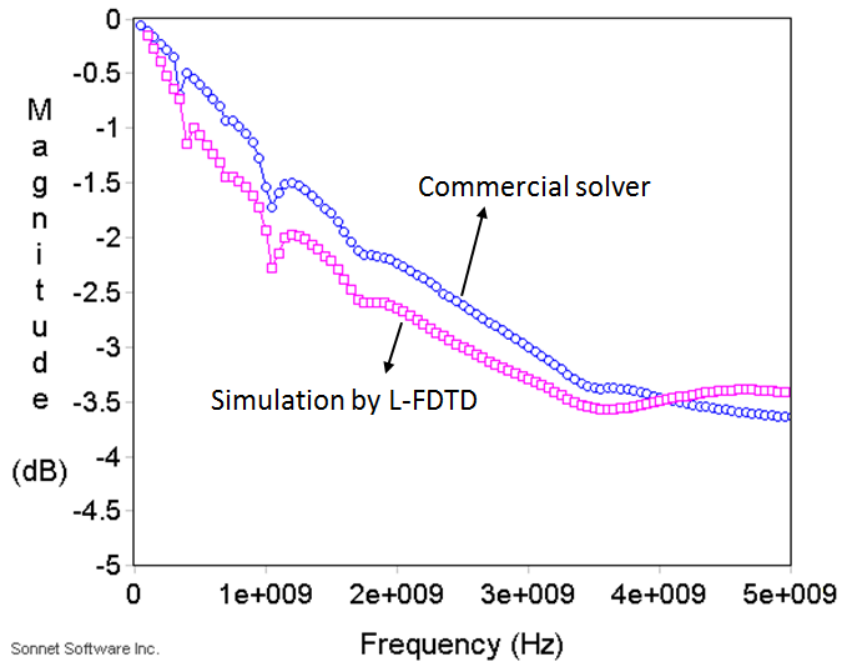
Figure 83. Calculated insertion loss.

8.4.3 Microstrip Line with TSV transition and no Return Current Discontinuity

Figure 84 illustrates the test case in this subsection. The structure consists of 4 metal layers. A microstrip line runs on the top and bottom layers with a TSV transition. The second and third layers are connected by 8 TSVs near the signal TSV from the top layer to the bottom layer. The materials and layer composition are the same as the test case in 8.4.1. Two ports are defined at ends of the transmission line. The structure is surrounded by a 500 *um* air margin and a PEC boundary.
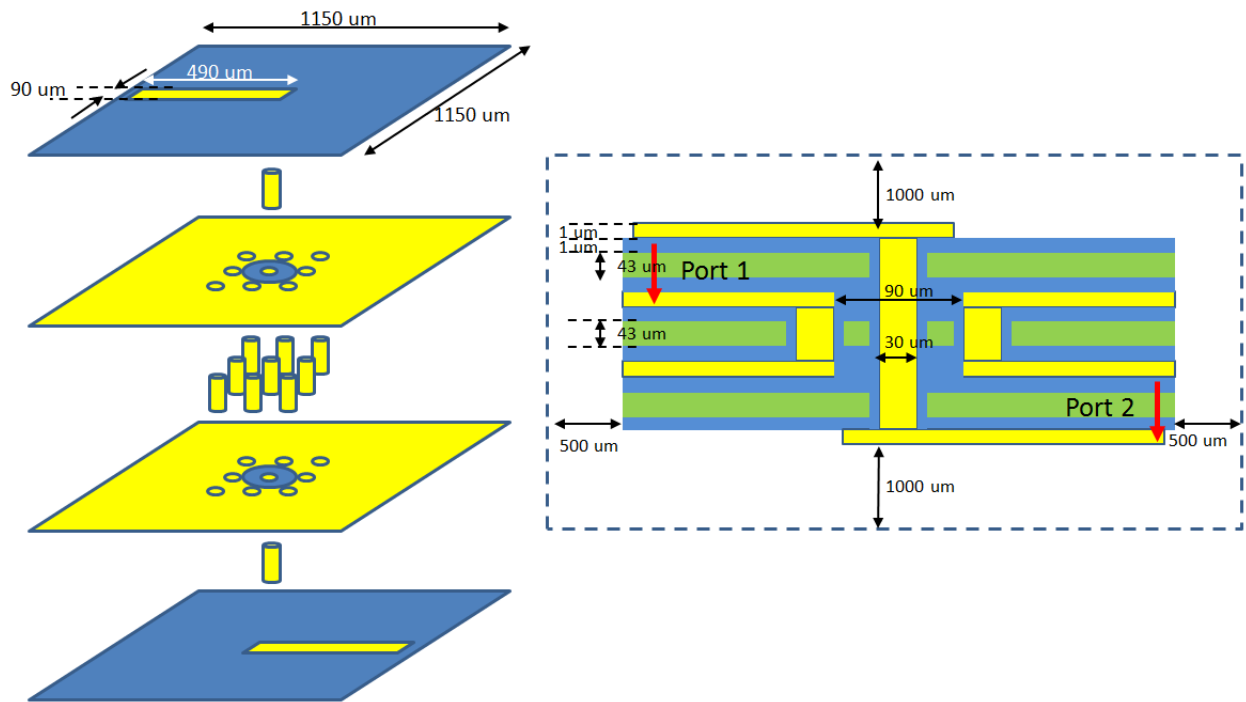
Figure 84. Expanded bird's-eye view and front cross-sectional view of test case.

After discretizing the structure into $152 \times 152 \times 29 = 670,016$ cells, Laguerre-FDTD simulation was performed. The lateral mesh between the second and third layers near the TSVs is shown in Figure 85. The very fine mesh for capturing the thin oxide of the TSV is too fine to

be distinguished in the figure. The smallest and largest sizes of the lateral mesh are 0.1 *um* and 0.1 *mm*, respectively. The scale difference in the physical dimensions is from 0.1 *um* of the TSV's oxide thickness to the 490 *um* of the microstrip line's length, 1:4900. Laguerre-FDTD takes 40 GB of memory and 280 minutes of CPU time to solve the structure in the time domain for 20 *ns*. However, the thin thickness of the TSV's oxide compared to the microstrip line's lateral dimension results in a very long simulation time of 400 days using FDTD because of the small CFL time step size of 0.16 *fs*. In this example, Laguerre-FDTD shows 2000× speed up over FDTD while consuming 720× more memory. The calculated insertion loss is plotted in Figure 86. Similar to the previous test case, the result could not be compared because both FDTD method and commercial tools have difficulty in solving the structure.
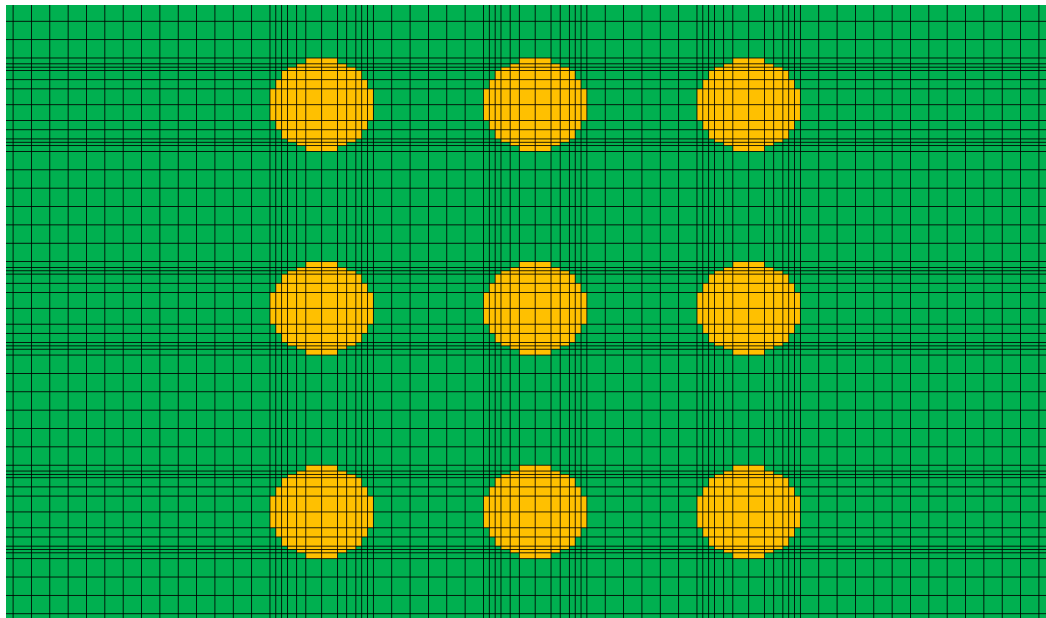
Figure 85. Lateral mesh near TSVs between second and third metal layer.
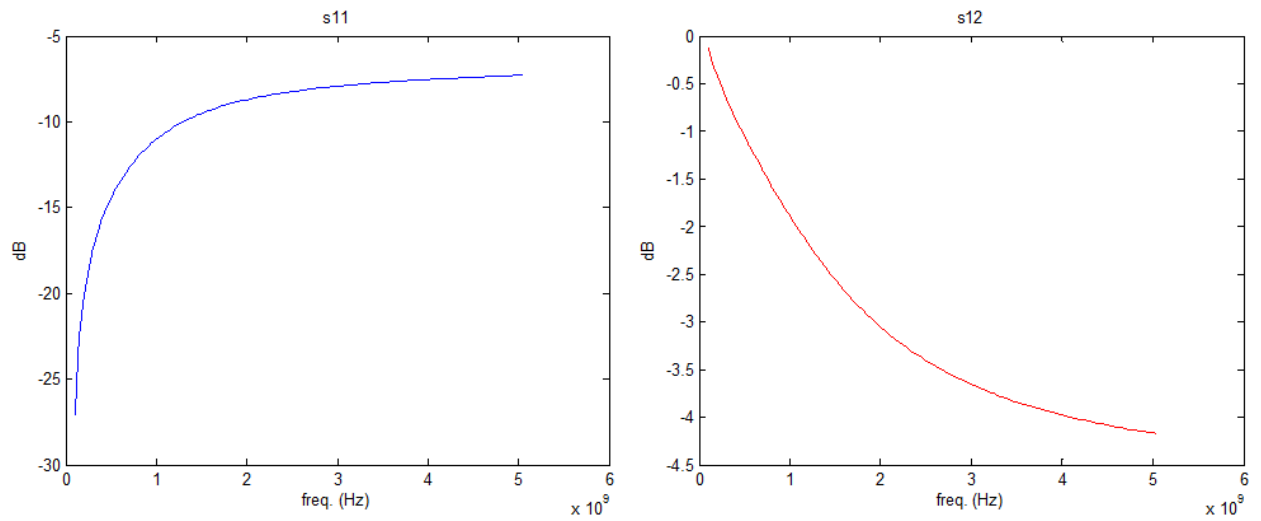
Figure 86. Calculated return loss (left) and insertion loss (right).

8.5 Complexity Scaling

Complexity analysis for the Laguerre-FDTD method has been studied. The memory complexity of the process is $O(N^{4/3})$, where N is the number of unknowns. The computational complexity of the process is also $O(N^{4/3})$. PARDISO solver in Intel's math kernel library [45] has been used to solve matrix equations resulted from the Laguerre-FDTD method. Results of the complexity analysis has been done on a 32-bit machine with 2 GB RAM with an Intel Core 2 Duo E4500 processor are shown in Figure 87.

113
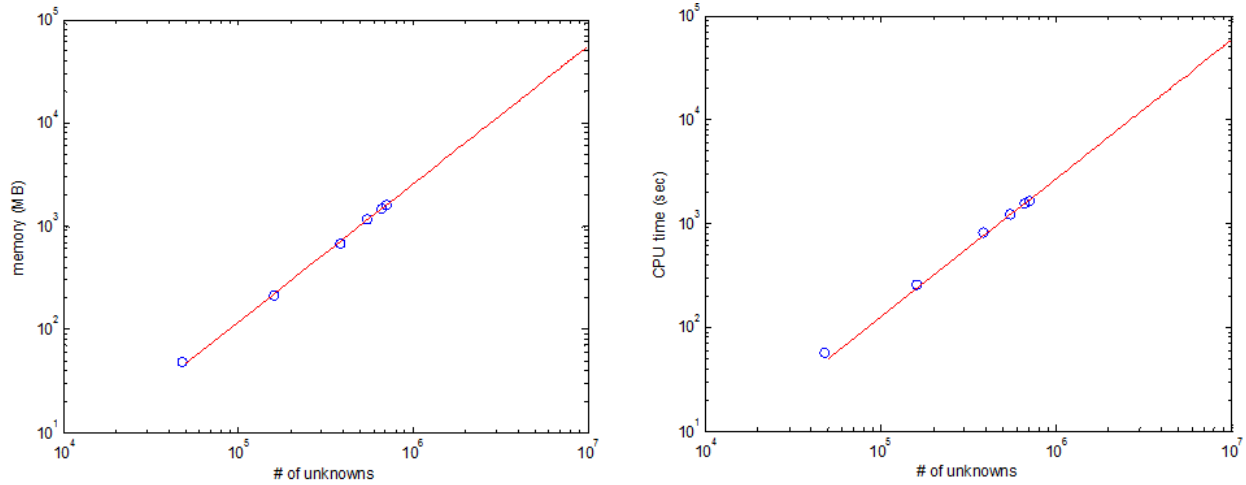
Figure 87. The scaling of memory complexity (left) and computational complexity (right).

8.6 Summary

In this chapter, the Laguerre-FDTD introduced and improved in this thesis has been applied to various practical examples. Successful model-to-hardware correlation has been shown as well as correlation with a commercial solver [41].

In the TSV array test cases, Laguerre-FDTD has shown excellent correlation to the commercial solver. The computation time is also competitive compared to the commercial solver's computation time. Excellent agreement has been shown in the TSV-TSV coupling example between the Laguerre-FDTD simulation and the time-domain measurement. It affirms the accuracy and the validity of the modeling of multiscale structures using Laguerre-FDTD. Additional model-to-hardware correlations also have been made in the microstrip line examples in 8.3. Three microstrip line test cases show good correlations to the measured S parameters. Through examples containing both microstrip lines and TSVs in Section 8.4, Laguerre-FDTD's scalability and advantage in the simulation of multiscale structure have been shown. Over $2000\times$

114

speed up is possible by using the Laguerre-FDTD method compared to conventional FDTD. Examples shown in this chapter are summarized in Table 3. Finally, the scaling of complexity has been performed. Both the memory complexity and the computational complexity of the Laguerre-FDTD are $O(N^{4/3})$ when PARDISO solver is used.

Table 3. Summary of test cases

Test case	# of cells	CPU time (mins)	Memory (GB)	Remark
3-by-3 TSV array	162k	342	4.8	Correlation with commercial tool
5-by-5 TSV array	403k	4500	10.5	Commercial tool was unable to solve
TSV-TSV coupling	168k	24	5.3	Correlation with measurement
Simple ML	53k	30	1.2	Correlation with measurement
ML over a slot	118k	70	3.4	Correlation with measurement
ML over small holes	108k	60	3.1	Correlation with measurement
ML on Si carrier with RPD I	458k	150	23	$2500 \times$ speed up compared to FDTD
ML on Si carrier with RPD II	766k	319	44	$100 \times$ speed up compared to FDTD, Correlation with commercial tool
ML on Si carrier with no RPD	670k	280	40	$2000 \times$ speed up compared to FDTD

CHAPTER IX

CONCLUSION

The need for high performance, small size, and low cost solutions for functional integration is becoming more significant for the semiconductor industry. To satisfy this need, 3-D integration is an unavoidable option to increase the required integration density. As more functionality is integrated in the package, the electromagnetic interactions within the package pose a significant problem. It requires a tool for design and analysis of ICs and the package structures together at the same time, which is also called chip-package co-simulation and co-design.

In the chip-package co-simulation and analysis of 3-D interconnection structures, large scale differences in physical dimensions of the structure should be dealt with. EM simulation of such multiscale structures using conventional FDTD is challenging because of CFL condition that limits the time step. Laguerre-FDTD and SLeEC methodologies have been proposed to overcome the limitation on the time step. However, they still have limitations for practical 3-D integration problems, e.g., difficulty to obtain the low-frequency response and to treat lossy materials. This provides motivation for research on the improvement of the Laguerre-FDTD to make it applicable for practical problems arising in 3-D integration. The following section clarifies the major contributions in this dissertation, emphasizing the usefulness of the proposed method for the electrical design of 3-D integrated systems.

9.1 Contribution

9.1.1   Generating time-domain waveforms from solutions in Laguerre domain

A method to efficiently convert solutions from the Laguerre domain into the time domain has been proposed. Applying a filter in the construction of the transient waveform from the

116

solutions in the Laguerre domain, a smaller number of Laguerre basis functions can be used in the simulation while maintaining or even enhancing the accuracy compared to the conversion scheme in the prior work [46].

9.1.2 Simulation for Long Time Intervals

The limited time duration for which the Laguerre-FDTD could be simulated has been resolved by the introduction of the balanced Laguerre basis function and the balanced exponential function. The Laguerre-FDTD method can now be executed for any length of time, enabling the computation of the low frequency response.

9.1.3 Frequency-domain Analysis Method using Laguerre-FDTD

An efficient time-domain simulation methodology for frequency-domain analysis has been proposed. By attaching shunt resistors at ports, the time-domain response decays quickly so that time-domain simulation can be completed in a short time duration. The effect of the additional resistances is de-embedded after the calculation of frequency-domain parameters. An efficient low-frequency analysis methodology using the Laguerre-FDTD approach also has been presented. By adjusting the time-scale factor in the Laguerre-FDTD, long-time transient simulations can be performed with no additional effort compared to short-time transient simulation for high-frequency analysis.

9.1.4 Modeling of Dispersive and Conductive Materials

A Laguerre-FDTD formulation for frequency-dependent dispersive materials has been proposed. Inclusion of dispersive materials in the simulation is critical to solving practical problems. For Debye and Lorentz media, the proposed formulation has been improved by enabling a recursive calculation of the electric flux density, which results in a significant reduction of the memory consumption.

117

9.2 Publications (from This Work)

- Myunghyun Ha, and Madhavan Swaminathan, "Memory-Efficient Laguerre-FDTD Formulation for Debye and Lorentz Media," submitted to *IEEE Microwave and Wireless Components Letters*.

- Myunghyun Ha, and Madhavan Swaminathan, "Minimizing the Number of Basis Functions in Chip-Package Co-Simulation Using Laguerre-FDTD," *IEEE International Symposium on Electromagnetic Compatibility,* Pages: 905-909, Long Beach, CA, Aug. 2011.

- Myunghyun Ha, and Madhavan Swaminathan, "A Laguerre-FDTD Formulation for Frequency-Dependent Dispersive Materials," *IEEE Microwave and Wireless Components Letters,* Page(s):225-227, Volume 21, Issue 5, May 2011.

- Myunghyun Ha, Joong-Ho Kim, Dan Oh, and Madhavan Swaminathan, "A Study of Reduced-terminal Models for System-level SSO Noise Analysis," *IEEE 19th Conference on Electrical Performance of Electronic Packaging*, Pages: 49-52, Austin, TX, Oct. 2010.

- Myunghyun Ha, Krishna Srinivasan, and Madhavan Swaminathan, "Transient Chip-Package Co-simulation Using the Laguerre-FDTD Scheme," *IEEE Transactions on Advanced Packaging*, Page(s):816-830, Volume 32, Issue 4, Nov. 2009.

- Krishna Srinivasan, Pradeep Yadav, Ege Engin, Madhavan Swaminathan, and Myunghyun Ha, "Fast EM/Circuit Transient Simulation Using Laguerre Equivalent Circuit (SLeEC)," *IEEE Transactions on Electromagnetic Compatibility*, Page(s):756-762, Volume 51, Issue 3, Part 2, Aug. 2009.

- Myunghyun Ha, Krishna Srinivasan, and Madhavan Swaminathan, "Chip-Package Co-Simulation with Multiscale Structures," *IEEE 17th Conference on Electrical Performance of Electronic Packaging*, Page: 339-342, San Jose, CA, Oct. 2008.

9.3 Publications (from Past Work)

- Jiwoo Pak, Myunghyun Ha, Jaemin Kim, Donghee Kang, Ho Choi, Seyoung Kwon, Keunsoo La, and Joungho Kim, "Design of a 3-D SiP for T-DMB with Improvement of Sensitivity and Noise Isolation," *IEEE Electronics Packaging Technology Conference*, Page(s) 1387-1392, 2008.

- Gawon Kim, Dong Gun Kam, Seung Jae Lee, Jaemin Kim, Myunghyun Ha, Kyoungchoul Koo, Jun So Pak, and Joungho Kim, "Modeling of Eye-Diagram Distortion and Data-Dependent Jitter in Meander Delay Lines on High-Speed Printed Circuit Boards (PCBs) Based on a Time-Domain Even-Mode and Odd-Mode Analysis," *IEEE Transactions on Microwave Theory and Techniques,* Page(s) 1962-1972, Volume 56 , Issue 8, 2008.

CHAPTER X

FUTURE WORK

The current contributions of this dissertation can be improved in their applicability to analysis of practical 3-D integrated systems by completing the following future work. The future work is specified for modeling of nonlinear phenomena and modeling of skin effect.

10.1 Modeling of Nonlinear Phenomena

In 3-D-integrated systems, the semiconductor's nonlinear property plays an important role. For example, the TSV's effective capacitance depends on bias voltage between the TSV and the silicon substrate. Such characteristics cannot be described with linear equations. In addition, modeling of a channel in a system requires the accurate model of receivers and transmitters which are connected at the end of the channel. Those receivers and transmitters consist of nonlinear devices such as transistors. Therefore, to describe such nonlinear properties, inclusion of nonlinear phenomena in the interconnection modeling is required.

However, it is not easy to incorporate nonlinear phenomena in the Laguerre-FDTD method since the Laguerre transform of a nonlinear operation is very difficult. Therefore, proper and clever approximations are needed to model the nonlinear phenomena in the Laguerre-FDTD method.

10.2 Modeling of Skin Effect

Conductor losses result in skin effect. Conductivity is already taken into account in the current Laguerre-FDTD formulation. However, to capture the skin effect accurately, very fine meshes near the surfaces of conductors are required because the electric field inside the conductor exponentially decreases as fields penetrate into the conductor from its surface, which increases the number of unknowns. If a proper skin effect model can be derived for the Laguerre-

FDTD method, the skin effect can be incorporated without using a fine mesh near the conductor surface.

Due to the skin effect, the effective thickness of conductors varies with frequency, which results in the change of effective resistance of a conductor with respect to frequency. In CHAPTER VII, it has been shown how to formulate a material's frequency-dependent dielectric constant in Laguerre-FDTD. Similarly, a frequency-dependent resistivity can be formulated in Laguerre-FDTD.

APPENDIX A: DERIVATION OF COMPLETE 3-D MODEL OF SLEEC

Consider the following six Maxwell's differential equations [12]:

$$\frac{\partial E_x}{\partial t} = \frac{1}{\epsilon}\left(\frac{\partial H_z}{\partial y} - \frac{\partial H_y}{\partial z} - J_x\right), \tag{154}$$

$$\frac{\partial E_y}{\partial t} = \frac{1}{\epsilon}\left(\frac{\partial H_x}{\partial z} - \frac{\partial H_z}{\partial x} - J_y\right), \tag{155}$$

$$\frac{\partial E_z}{\partial t} = \frac{1}{\epsilon}\left(\frac{\partial H_y}{\partial x} - \frac{\partial H_x}{\partial y} - J_z\right), \tag{156}$$

$$\frac{\partial H_x}{\partial t} = \frac{1}{\mu}\left(\frac{\partial E_y}{\partial z} - \frac{\partial E_z}{\partial y}\right), \tag{157}$$

$$\frac{\partial H_y}{\partial t} = \frac{1}{\mu}\left(\frac{\partial E_z}{\partial x} - \frac{\partial E_x}{\partial z}\right), \tag{158}$$

$$\frac{\partial H_z}{\partial t} = \frac{1}{\mu}\left(\frac{\partial E_x}{\partial y} - \frac{\partial E_y}{\partial x}\right). \tag{159}$$

Consider the standard FDTD Yee cell [11] shown in Figure 88. The cross sections of the FDTD cell at the locations marked by the dotted lines in Figure 88 are shown in Figure 89. The cross sections in Figure 8 are viewed by standing on the $+\infty$ of y, x, and z axis and facing the Yee cell, respectively.
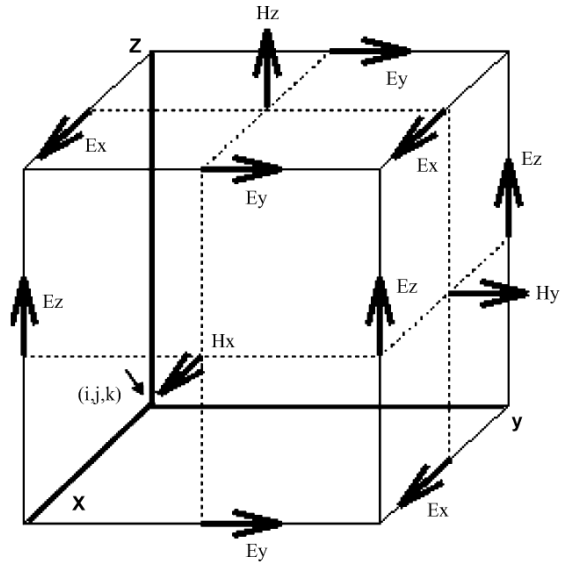
Figure 88. Standard Yee cell.
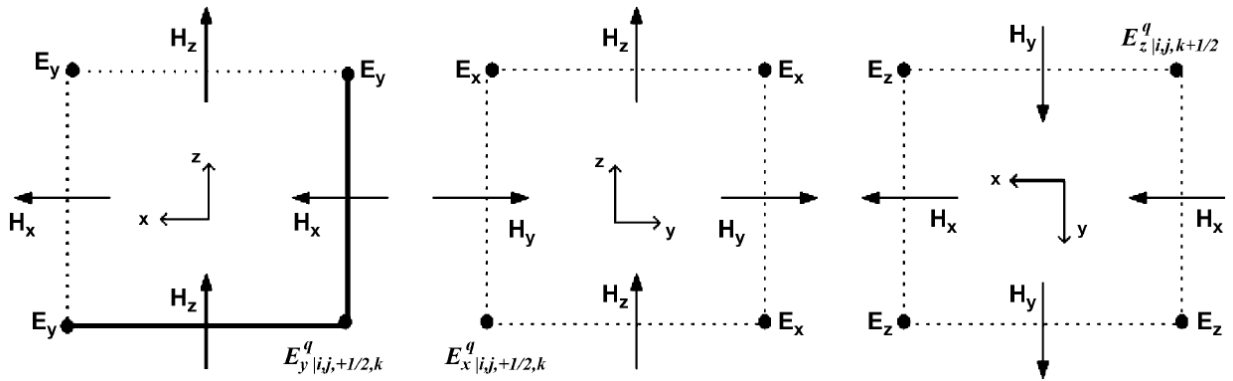
Figure 89. Sections of the Yee cell marked by the dotted lines in Figure 7 parallel to the *xz*, *yz*, and *xy* planes, respectively. Dots indicate direction of the fields pointing out of the page.

Converting (154)-(159) into the Laguerre-domain and rewriting them in a matrix form in after discretization using the central-difference scheme in space as shown in Figure 88 and Figure 89, we have

123

$$E_x^q \big|_{i+\frac{1}{2},j,k} = -C_z^E \big|_{i,j,k} \left(H_y^q \big|_{i+\frac{1}{2},j,k+\frac{1}{2}} - H_y^q \big|_{i+\frac{1}{2},j,k-\frac{1}{2}} \right)$$

$$+ C_y^E {}_{i,j,k} \left(H_z^q \big|_{i+\frac{1}{2},j+\frac{1}{2},k} - H_z^q \big|_{i+\frac{1}{2},j-\frac{1}{2},k} \right)$$

$$+ 2E_x^{init} \big|_{i+\frac{1}{2},j\frac{1}{2},k} - \frac{2}{s\varepsilon} J_x^q \big|_{i+\frac{1}{2},j,k}$$

$$- 2 \sum_{l=0,q>0}^{q-1} E_x^l \big|_{i+\frac{1}{2},j,k\prime} \tag{160}$$

$$E_y^q \big|_{i,j+\frac{1}{2},k} = -C_x^E \big|_{i,j,k} \left(H_z^q \big|_{i+\frac{1}{2},j+\frac{1}{2},k} - H_z^q \big|_{i-\frac{1}{2},j+\frac{1}{2},k} \right)$$

$$+ C_z^E {}_{i,j,k} \left(H_x^q \big|_{i,j+\frac{1}{2},k+\frac{1}{2}} - H_x^q \big|_{i,j+\frac{1}{2},k-\frac{1}{2}} \right)$$

$$+ 2E_y^{init} \big|_{i,j+\frac{1}{2},k} - \frac{2}{s\varepsilon} J_y^q \big|_{i,j+\frac{1}{2},k}$$

$$- 2 \sum_{l=0,q>0}^{q-1} E_y^l \big|_{i,j+\frac{1}{2},k\prime} \tag{161}$$

$$E_z^q \big|_{i,j,k+\frac{1}{2}} = -C_y^E \big|_{i,j,k} \left(H_x^q \big|_{i,j+\frac{1}{2},k+\frac{1}{2}} - H_x^q \big|_{i,j-\frac{1}{2},k+\frac{1}{2}} \right)$$

$$+ C_x^E {}_{i,j,k} \left(H_y^q \big|_{i+\frac{1}{2},j,k+\frac{1}{2}} - H_z^q \big|_{i-\frac{1}{2},j,k+\frac{1}{2}} \right)$$

$$+ 2E_z^{init} \big|_{i,j,k+\frac{1}{2}} - \frac{2}{s\varepsilon} J_z^q \big|_{i,j,k+\frac{1}{2}}$$

$$- 2 \sum_{l=0,q>0}^{q-1} E_z^l \big|_{i,j,k+\frac{1}{2}\prime} \tag{162}$$

124

$$H_x^q \big|_{i,j+\frac{1}{2},k+\frac{1}{2}} = -C_y^H \big|_{i,j,k} \left(E_z^q \big|_{i,j+1,k+\frac{1}{2}} - E_z^q \big|_{i,j,k+\frac{1}{2}} \right)$$

$$+ C_z^H \big|_{i,j,k} \left(E_y^q \big|_{i,j+\frac{1}{2},k+1} - E_y^q \big|_{i,j+\frac{1}{2},k} \right) \qquad (163)$$

$$- 2 \sum_{l=0,q>0}^{q-1} H_x^l \big|_{i,j+\frac{1}{2},k+\frac{1}{2}},$$

$$H_y^q \big|_{i+\frac{1}{2},j,k+\frac{1}{2}} = -C_z^H \big|_{i,j,k} \left(E_x^q \big|_{i+\frac{1}{2},j,k+1} - E_x^q \big|_{i+\frac{1}{2},j,k} \right)$$

$$+ C_x^H \big|_{i,j,k} \left(E_z^q \big|_{i+1,j,k+\frac{1}{2}} - E_z^q \big|_{i,j,k+\frac{1}{2}} \right) \qquad (164)$$

$$- 2 \sum_{l=0,q>0}^{q-1} H_y^l \big|_{i+\frac{1}{2},j,k+\frac{1}{2}},$$

$$H_z^q \big|_{i+\frac{1}{2},j+\frac{1}{2},k} = -C_x^H \big|_{i,j,k} \left(E_y^q \big|_{i+1,j+\frac{1}{2},k} - E_y^q \big|_{i,j+\frac{1}{2},k} \right)$$

$$+ C_y^H \big|_{i,j,k} \left(E_x^q \big|_{i+\frac{1}{2},j+1,k} - E_x^q \big|_{i+\frac{1}{2},j,k} \right) \qquad (165)$$

$$- 2 \sum_{l=0,q>0}^{q-1} H_z^l \big|_{i+\frac{1}{2},j+\frac{1}{2},k},$$

where

$$C_x^E{}_{i,j,k} = \frac{2}{s\varepsilon_{i,j,k}\Delta x_i}, \qquad (166)$$

$$C_y^E{}_{i,j,k} = \frac{2}{s\varepsilon_{i,j,k}\Delta y_j}, \qquad (167)$$

$$C_z^E{}_{i,j,k} = \frac{2}{s\varepsilon_{i,j,k}\Delta z_k}, \qquad (168)$$

$$C_x^H{}_{i,j,k} = \frac{2}{s\mu_{i,j,k}\Delta x_i}, \qquad (169)$$

125

$$C_y^H\Big|_{i,j,k} = \frac{2}{s\mu_{i,j,k}\Delta y_j}, \tag{170}$$

$$C_z^H\Big|_{i,j,k} = \frac{2}{s\mu_{i,j,k}\Delta z_k}. \tag{171}$$

Replacing the electric and magnetic fields in equation (160)-(165) with the nodal voltages and the branch currents, we have

$$
\begin{aligned}
V^q\Big|_{i+\frac{1}{2},j,k} &= -C_z^E\Big|_{i,j,k}\left(I^q\Big|_{i+\frac{1}{2},j,k+\frac{1}{2}} - I^q\Big|_{i+\frac{1}{2},j,k-\frac{1}{2}}\right) \\
&\quad + C_y^E\Big|_{i,j,k}\left(I^q\Big|_{i+\frac{1}{2},j+\frac{1}{2},k} - I^q\Big|_{i+\frac{1}{2},j-\frac{1}{2},k}\right) \\
&\quad + 2V^{init}\Big|_{i+\frac{1}{2},j,k} - \frac{2}{s\varepsilon}J_x^q\Big|_{i+\frac{1}{2},j,k} \\
&\quad - 2\sum_{l=0,q>0}^{q-1} V^l\Big|_{i+\frac{1}{2},j,k},
\end{aligned}
\tag{172}
$$

$$
\begin{aligned}
V^q\Big|_{i,j+\frac{1}{2},k} &= -C_x^E\Big|_{i,j,k}\left(I^q\Big|_{i+\frac{1}{2},j+\frac{1}{2},k} - I^q\Big|_{i-\frac{1}{2},j+\frac{1}{2},k}\right) \\
&\quad + C_z^E\Big|_{i,j,k}\left(I^q\Big|_{i,j+\frac{1}{2},k+\frac{1}{2}} - I^q\Big|_{i,j+\frac{1}{2},k-\frac{1}{2}}\right) \\
&\quad + 2V^{init}\Big|_{i,j+\frac{1}{2},k} - \frac{2}{s\varepsilon}J_y^q\Big|_{i,j+\frac{1}{2},k} \\
&\quad - 2\sum_{l=0,q>0}^{q-1} V^l\Big|_{i,j+\frac{1}{2},k},
\end{aligned}
\tag{173}
$$

126

$$V^q \big|_{i,j,k+\frac{1}{2}} = -C_y^E \big|_{i,j,k} \left(I^q \big|_{i,j+\frac{1}{2},k+\frac{1}{2}} - I^q \big|_{i,j-\frac{1}{2},k+\frac{1}{2}} \right)$$

$$+ C_x^E \big|_{i,j,k} \left(I^q \big|_{i+\frac{1}{2},j,k+\frac{1}{2}} - I^q \big|_{i-\frac{1}{2},j,k+\frac{1}{2}} \right)$$

$$+ 2V^{init} \big|_{i,j,k+\frac{1}{2}} - \frac{2}{s\varepsilon} J_z^q \big|_{i,j,k+\frac{1}{2}}$$

$$- 2 \sum_{l=0,q>0}^{q-1} V^l \big|_{i,j,k+\frac{1}{2}},$$

(174)

$$I^q \big|_{i,j+\frac{1}{2},k+\frac{1}{2}} = -C_y^H \big|_{i,j,k} \left(V^q \big|_{i,j+1,k+\frac{1}{2}} - V^q \big|_{i,j,k+\frac{1}{2}} \right)$$

$$+ C_z^H \big|_{i,j,k} \left(V_y^q \big|_{i,j+\frac{1}{2},k+1} - V_y^q \big|_{i,j+\frac{1}{2},k} \right)$$

$$- 2 \sum_{l=0,q>0}^{q-1} I^l \big|_{i,j+\frac{1}{2},k+\frac{1}{2}},$$

(175)

$$I^q \big|_{i+\frac{1}{2},j,k+\frac{1}{2}} = -C_z^H \big|_{i,j,k} \left(V^q \big|_{i+\frac{1}{2},j,k+1} - V^q \big|_{i+\frac{1}{2},j,k} \right)$$

$$+ C_x^H \big|_{i,j,k} \left(V^q \big|_{i+1,j,k+\frac{1}{2}} - V^q \big|_{i,j,k+\frac{1}{2}} \right)$$

$$- 2 \sum_{l=0,q>0}^{q-1} I^l \big|_{i+\frac{1}{2},j,k+\frac{1}{2}},$$

(176)

$$I^q \big|_{i+\frac{1}{2},j+\frac{1}{2},k} = -C_x^H \big|_{i,j,k} \left(V^q \big|_{i+1,j+\frac{1}{2},k} - V^q \big|_{i,j+\frac{1}{2},k} \right)$$

$$+ C_y^H \big|_{i,j,k} \left(V^q \big|_{i+\frac{1}{2},j+1,k} - V^q \big|_{i+\frac{1}{2},j,k} \right)$$

$$- 2 \sum_{l=0,q>0}^{q-1} I^l \big|_{i+\frac{1}{2},j+\frac{1}{2},k}.$$

(177)

Equation (172)-(177) can be represented in a circuit form using controlled sources as follows:

127

$$V^q \big|_{i+\frac{1}{2},j,k} = R_1 \big|_{i+\frac{1}{2},j,k} I_1 \big|_{i+\frac{1}{2},j,k} + R_2 \big|_{i+\frac{1}{2},j,k} I_2 \big|_{i+\frac{1}{2},j,k}$$
$$+ V_{src} \big|_{i+\frac{1}{2},j,k}, \tag{178}$$

$$V^q \big|_{i,j+\frac{1}{2},k} = R_1 \big|_{i,j+\frac{1}{2},k} I_1 \big|_{i,j+\frac{1}{2},k} + R_2 \big|_{i,j+\frac{1}{2},k} I_2 \big|_{i,j+\frac{1}{2},k}$$
$$+ V_{src} \big|_{i,j+\frac{1}{2},k}, \tag{179}$$

$$V^q \big|_{i,j,k+\frac{1}{2}} = R_1 \big|_{i,j,k+\frac{1}{2}} I_1 \big|_{i,j,k+\frac{1}{2}} + R_2 \big|_{i,j,k+\frac{1}{2}} I_2 \big|_{i,j,k+\frac{1}{2}}$$
$$+ V_{src} \big|_{i,j,k+\frac{1}{2}}, \tag{180}$$

$$I^q \big|_{i,j+\frac{1}{2},k+\frac{1}{2}} = \frac{1}{R_1 \big|_{i,j+\frac{1}{2},k+\frac{1}{2}}} \left(-V^q \big|_{i,j+1,k+\frac{1}{2}} + V^q \big|_{i,j,k+\frac{1}{2}} \right)$$
$$+ I_1 \big|_{i,j+\frac{1}{2},k+\frac{1}{2}} + I_2 \big|_{i,j+\frac{1}{2},k+\frac{1}{2}}, \tag{181}$$

$$I^q \big|_{i+\frac{1}{2},j,k+\frac{1}{2}} = \frac{1}{R_1 \big|_{i+\frac{1}{2},j,k+\frac{1}{2}}} \left(-V^q \big|_{i+\frac{1}{2},j,k+1} + V^q \big|_{i+\frac{1}{2},j,k} \right)$$
$$+ I_1 \big|_{i+\frac{1}{2},j,k+\frac{1}{2}} + I_2 \big|_{i+\frac{1}{2},j,k+\frac{1}{2}}, \tag{182}$$

$$I^q \big|_{i+\frac{1}{2},j+\frac{1}{2},k} = \frac{1}{R_1 \big|_{i+\frac{1}{2},j+\frac{1}{2},k}} \left(-V^q \big|_{i+1,j+\frac{1}{2},k} + V^q \big|_{i,j+\frac{1}{2},k} \right)$$
$$+ I_1 \big|_{i+\frac{1}{2},j+\frac{1}{2},k} + I_2 \big|_{i+\frac{1}{2},j+\frac{1}{2},k}, \tag{183}$$

where

$$R_1 \big|_{i+\frac{1}{2},j,k} = C_z^E \big|_{i,j,k}, \tag{184}$$

$$I_1 \big|_{i+\frac{1}{2},j,k} = -I^q \big|_{i+\frac{1}{2},j,k+\frac{1}{2}} + I^q \big|_{i+\frac{1}{2},j,k-\frac{1}{2}}, \tag{185}$$

$$R_2 \big|_{i+\frac{1}{2},j,k} = C_y^E \big|_{i,j,k}, \tag{186}$$

$$I_2 \big|_{i+\frac{1}{2},j,k} = I^q \big|_{i+\frac{1}{2},j+\frac{1}{2},k} - I^q \big|_{i+\frac{1}{2},j-\frac{1}{2},k}, \tag{187}$$

$$V_{src} \big|_{i+\frac{1}{2},j,k} = 2V^{init} \big|_{i+\frac{1}{2},j,k} - \frac{2}{s\varepsilon} J_x^q \big|_{i+\frac{1}{2},j,k} - 2 \sum_{l=0,q>0}^{q-1} V^l \big|_{i+\frac{1}{2},j,k}, \tag{188}$$

$$R_1 \big|_{i,j+\frac{1}{2},k} = C_x^E \big|_{i,j,k}, \tag{189}$$

$$I_1 \big|_{i,j+\frac{1}{2},k} = -I^q \big|_{i+\frac{1}{2},j+\frac{1}{2},k} + I^q \big|_{i-\frac{1}{2},j+\frac{1}{2},k}, \tag{190}$$

$$R_2 \big|_{i+\frac{1}{2},j,k} = C_z^E \big|_{i,j,k}, \tag{191}$$

$$I_2 \big|_{i,j+\frac{1}{2},k} = I^q \big|_{i,j+\frac{1}{2},k+\frac{1}{2}} - I^q \big|_{i,j+\frac{1}{2},k-\frac{1}{2}}, \tag{192}$$

$$V_{src} \big|_{i,j+\frac{1}{2},k} = 2V^{init} \big|_{i,j+\frac{1}{2},k} - \frac{2}{s\varepsilon} J_y^q \big|_{i,j+\frac{1}{2},k} - 2 \sum_{l=0,q>0}^{q-1} V^l \big|_{i,j+\frac{1}{2},k}, \tag{193}$$

$$R_1 \big|_{i,j,k+\frac{1}{2}} = C_y^E \big|_{i,j,k}, \tag{194}$$

$$I_1 \big|_{i,j,k+\frac{1}{2}} = -I^q \big|_{i,j+\frac{1}{2},k+\frac{1}{2}} + I^q \big|_{i,j-\frac{1}{2},k+\frac{1}{2}}, \tag{195}$$

$$R_2 \big|_{i+\frac{1}{2},j,k} = C_x^E \big|_{i,j,k}, \tag{196}$$

$$I_2 \big|_{i,j,k+\frac{1}{2}} = I^q \big|_{i+\frac{1}{2},j,k+\frac{1}{2}} - I^q \big|_{i-\frac{1}{2},j,k+\frac{1}{2}}, \tag{197}$$

$$V_{src} \big|_{i,j,k+\frac{1}{2}} = 2V^{init} \big|_{i,j,k+\frac{1}{2}} - \frac{2}{s\varepsilon} J_z^q \big|_{i,j,k+\frac{1}{2}} - 2 \sum_{l=0,q>0}^{q-1} V^l \big|_{i,j,k+\frac{1}{2}}, \tag{198}$$

$$R_1 \big|_{i,j+\frac{1}{2},k+\frac{1}{2}} = \frac{1}{C_y^H \big|_{i,j,k}}, \tag{199}$$

$$I_1\big|_{i,j+\frac{1}{2},k+\frac{1}{2}} = C_z^H\big|_{i,j,k}\left(V_y^q\big|_{i,j+\frac{1}{2},k+1} - V_y^q\big|_{i,j+\frac{1}{2},k}\right), \tag{200}$$

$$I_2\big|_{i,j+\frac{1}{2},k+\frac{1}{2}} = -2\sum_{l=0,q>0}^{q-1} I^l\big|_{i,j+\frac{1}{2},k+\frac{1}{2}}, \tag{201}$$

$$R_1\big|_{i+\frac{1}{2},j,k+\frac{1}{2}} = \frac{1}{C_z^H\big|_{i,j,k}}, \tag{202}$$

$$I_1\big|_{i+\frac{1}{2},j,k+\frac{1}{2}} = C_x^H\big|_{i,j,k}\left(V^q\big|_{i+1,j,k+\frac{1}{2}} - V^q\big|_{i,j,k+\frac{1}{2}}\right), \tag{203}$$

$$I_2\big|_{i+\frac{1}{2},j,k+\frac{1}{2}} = -2\sum_{l=0,q>0}^{q-1} I^l\big|_{i+\frac{1}{2},j,k+\frac{1}{2}}, \tag{204}$$

$$R_1\big|_{i+\frac{1}{2},j+\frac{1}{2},k} = \frac{1}{C_x^H\big|_{i,j,k}}, \tag{205}$$

$$I_1\big|_{i+\frac{1}{2},j+\frac{1}{2},k} = C_y^H\big|_{i,j,k}\left(V^q\big|_{i+\frac{1}{2},j+1,k} - V^q\big|_{i+\frac{1}{2},j,k}\right), \tag{206}$$

$$I_2\big|_{i+\frac{1}{2},j+\frac{1}{2},k} = -2\sum_{l=0,q>0}^{q-1} I^l\big|_{i+\frac{1}{2},j+\frac{1}{2},k}. \tag{207}$$

Schematic of the companion model described in (178)-(207) in the 3-D FDTD grid is shown in Figure 90 with the associated electric fields in the 3-D FDTD grid shown in Figure 91.

130
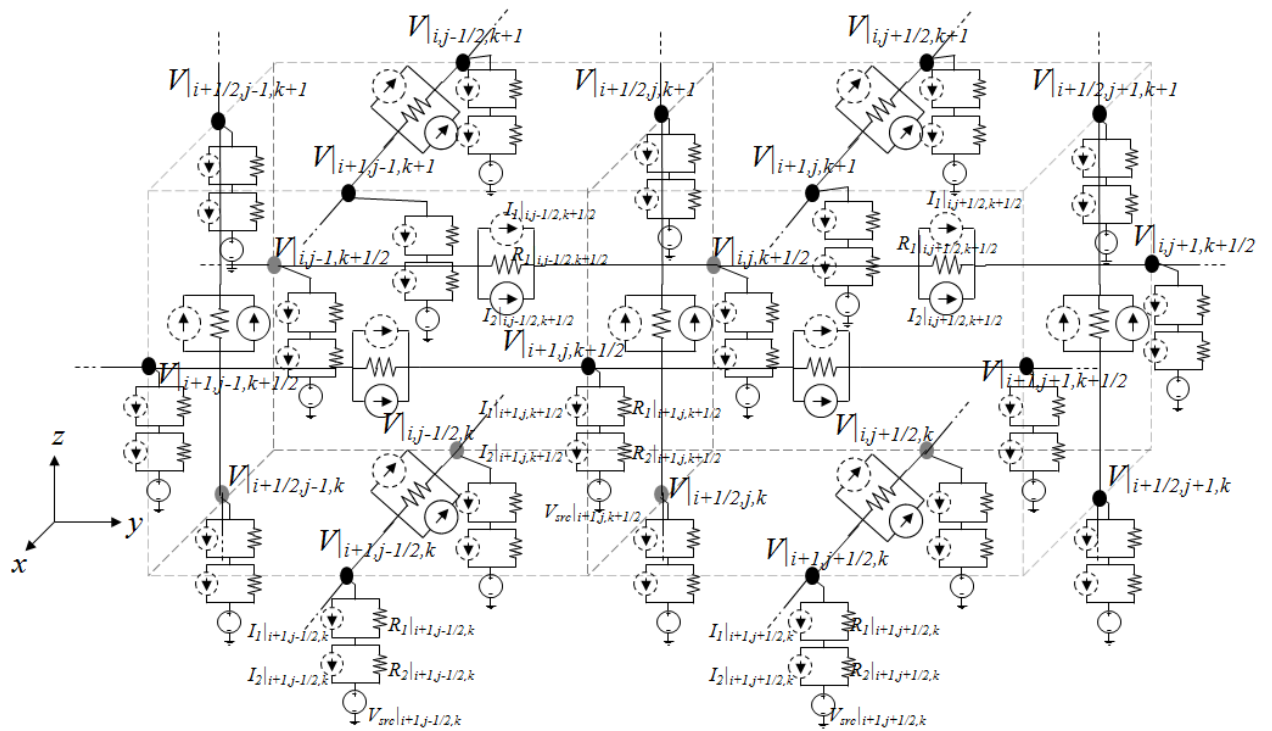
Figure 90. Companion model of the 3-D FDTD grid in Laguerre domain.
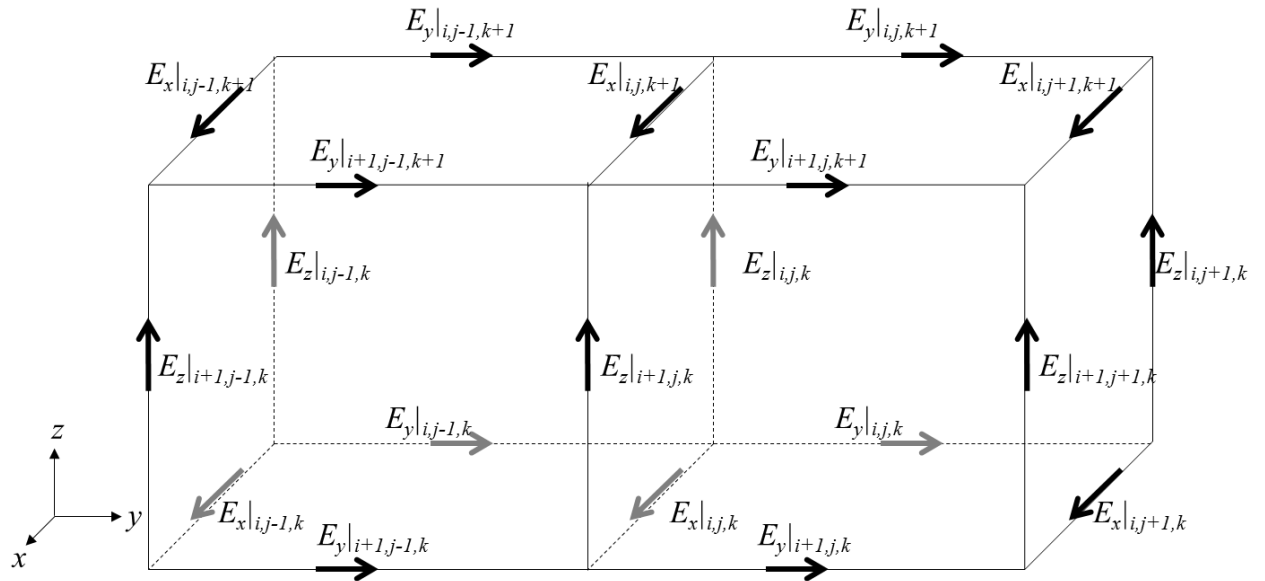
Figure 91. Electric fields in the 3-D FDTD grid.

131

The circuit given in Figure 90 can be stamped in a modified-nodal-analysis matrix [29] and solved to find the unknown Laguerre basis coefficients of the electric and magnetic fields.

APPENDIX B: MATHEMATICAL JUSTIFICATION FOR ERROR ANALYSIS AT THE INITIAL POINT

Let $E_{org}(t)$ be the original solution of the time-domain waveform which is represented as a sum of infinite number of weighted Laguerre basis functions where E_p represents pth Laguerre coefficient corresponding to the pth Laguerre basis function $\varphi_p(\bar{t})$:

$$E_{org}(t) = \sum_{p=0}^{\infty} E_p \cdot \varphi_p(\bar{t}). \tag{208}$$

where $\bar{t} = s \cdot t$, s is a time-scale factor. Using an approximation with N basis functions, the waveform is now represented as

$$E_{approx}(t) = \sum_{p=0}^{N-1} E_p \cdot \varphi_p(\bar{t}). \tag{209}$$

The error $\epsilon(t)$ at time t can be written as

$$\begin{aligned}
\epsilon(t) &= E_{org}(t) - E_{approx}(t) \\
&= \sum_{p=0}^{\infty} E_p \cdot \varphi_p(\bar{t}) - \sum_{p=0}^{N-1} E_p \cdot \varphi_p(\bar{t}) \\
&= \sum_{p=N}^{\infty} E_p \cdot \varphi_p(\bar{t}) \\
&= \lim_{M \to \infty} \sum_{p=N}^{N+M-1} E_p \cdot \varphi_p(\bar{t}).
\end{aligned} \tag{210}$$

Since $E_{org}(t)$ is approximated using the first N basis functions, E_N, E_{N+1}, E_{N+2}, ... are unknown while E_0, E_1, ..., E_{N-1} are known. Let us assume E_p where $p \geq N$ be a random variable with normal distribution (mean μ and variance σ^2) given by

$$E_p \sim N(0, \sigma^2) \text{ for } p \geq N. \tag{211}$$

Error at time $t = 0$ can be calculated as

$$\epsilon(0) = E_{org}(0) - E_{approx}(0)$$

$$= \sum_{p=0}^{\infty} E_p \cdot \varphi_p(0) - \sum_{p=0}^{N-1} E_p \cdot \varphi_p(0)$$

$$= \sum_{p=N}^{\infty} E_p \cdot \varphi_p(0) \qquad (212)$$

$$= \lim_{M \to \infty} M\mu.$$

The mean of E_p is given by

$$\mu = \lim_{M \to \infty} \frac{E_{org}(0) - \sum_{p=0}^{N-1} E_p \cdot \varphi_p(0)}{M} = 0. \qquad (213)$$

Therefore, under the assumption that E_p for $p \geq N$ is a Gaussian random variable, its mean should be zero.

Since the sum of M Gaussian random variables with zero mean and variance σ^2 is another Gaussian random variable with zero-mean and variance $M\sigma^2$, error at $t = 0$ is a Gaussian random variable with zero-mean and variance $M\sigma^2$ while M goes to infinity:

$$\epsilon(0) \sim N\left(0, \lim_{M \to \infty} \sum_{p=1}^{M} \sigma^2\right). \qquad (214)$$

Similarly, error at $t > 0$ also can be represented as a Gaussian random variable since it is the sum of weighted Gaussian random variables. While its mean is still zero, Since $\varphi_p(t) < 1$ for $t > 0$, as shown in Figure 92, variance of error $\epsilon(t)$ is always smaller than variance $\epsilon(0)$ of for $t > 0$:

$$Var\big(\epsilon(t)\big) = \lim_{M\to\infty} \sum_{p=N}^{N+M-1} \varphi_p(t)^2 \sigma^2$$

$$< \lim_{M\to\infty} \sum_{p=N}^{N+M-1} \sigma^2 \qquad (215)$$
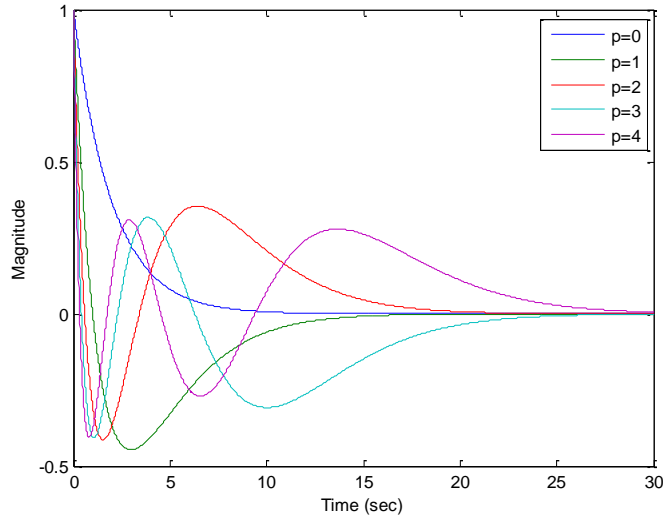
$$< Var\big(\epsilon(0)\big).$$

Figure 92. Laguerre basis functions for orders $p = 0$ to $p = 4$.

Since $\varphi_p(t)$ is smaller than 1 for $t > 0$, as shown in Figure 92, $Var\big(\epsilon(t)\big)$ is smaller than $Var\big(\epsilon(0)\big)$. Their probability density functions can therefore be approximated as shown in Figure 93. The probability that $|\epsilon(0)|$ is greater than $|\epsilon(t)|$ for $t > 0$ is very small, which implies that $|\epsilon(0)| > |\epsilon(t)|$ for $t > 0$ in most cases. Therefore, in most cases, error at time $t > 0$ is bounded by error at time $t = 0$. Thus, minimizing error at time is effective in reducing error at $t > 0$.
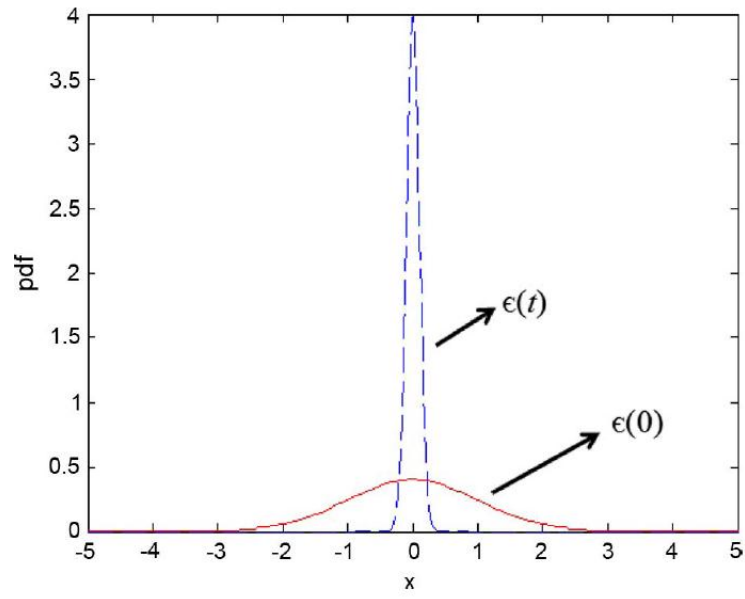
Figure 93. Probability density functions of normal distribution with large and small variances.

APPENDIX C: SLEEC SOFTWARE

I.   Overview.

SLeEC is a transient EM solver for multiscale structures. SLeEC consists of files shown in Table 4.

Table 4. Configuration of SLeEC software.

File name	Remarks
SLeEC.exe	SLeEC engine executable file
Config.txt	SLeEC Configuration file

As shown in Figure 94, SLeEC reads two input files in ASCII format which can be easily modified using text editors such as notepad: structure description file (*.sd) and simulation setup file (*.ss). Simulation description file has information about the structure. No information related to simulation is contained. Simulation setup file has information about setup of simulation such as port and source definitions. Both files are explained in detail in the later part of this appendix.
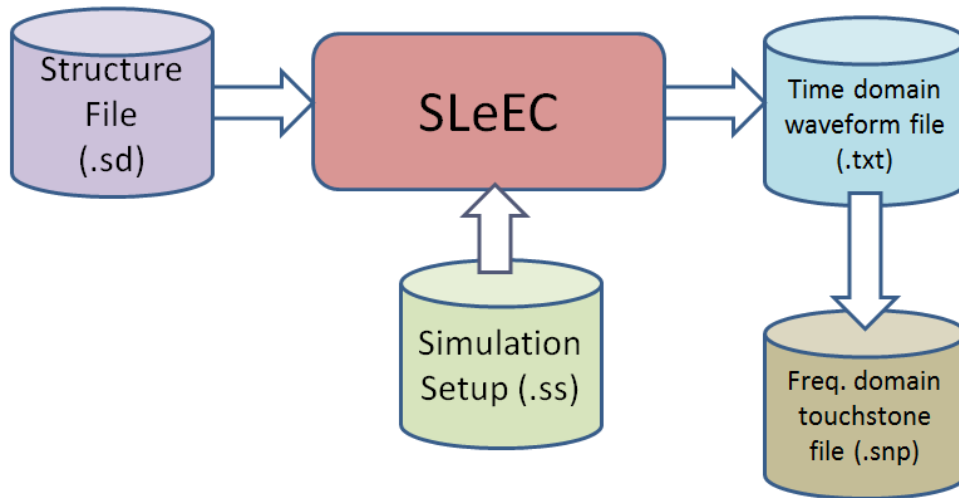
Figure 94. Flow chart of SLeEC software.

SLeEC performs time domain analysis. If user wants to do the time domain analysis, simulation setup file has information about simulation setup such as simulation time, source waveform, and probing point.

Following output files are generated by simulation: time domain waveform (*.txt) and Laguerre coefficients for simulated time domain waveform (*.txt). Time domain waveform file have series of numbers that represents time line in second, source current in Ampere, probed electric field value in V/m. Laguerre coefficient output file contains Laguerre coefficients of simulated time domain waveforms. Normally, this output file can be ignored since Laguerre coefficient itself does not have much value from user's point of view. Time domain waveform built from the Laguerre coefficients are contained in the time domain waveform output file.

II.   Execution of SLeEC Program

To execute the SLeEC software, the following command is executed,

Sleec sample1 sample2 sample3

138

Then, *SLeEC.exe* reads *sample1.sd*, *sample2.ss,* and performs the time-domain simulation. As a result of the simulation, one or two files are generated: *sample.txt* for time-domain waveforms, and *sampleOutputLagCoefs.txt* for Laguerre coefficients. Second file is optional.

III. Configuration file

Config.txt is configuration file for *SLeEC.exe*. It has several properties as following.

1. Energy Variation at Knee

Knee value is the number of basis function that energy content begins to be saturated and flatten. If the energy content's fluctuation as increasing the number of basis functions is smaller than Energy Variation at Knee and keep being within the boundary, then the number of basis function at that time is regarded as knee value that energy fluctuation begins to flatten.

2. Bounded Iteration

If this is true, then the simulation is terminated when time-domain waveform seems to be mature even though termination condition in terms of energy variation does not meet. If the number of basis function is set to be unbounded, then simulation is going on until the number of basis function is found that satisfies energy variation, which may provides accurate result, but longer simulation time.

3. Export Coefficients

If this is true, optional output file that contains Laguerre coefficients of time-domain waveform is generated.

4. Show Progress

Show the number of basis functions whose coefficient is obtained and whether knee value is reached. If this property is off, then just dot will be shown for every 20 basis functions.

IV. Structure Description File

The SLeEC structure description file (*.sd extension) is a file that contains the meshed structure data to be provided to SLeEC. It has three sections:

```
[Basic Mesh Info]
```

```
[Material Info]
```

```
[Structure Info]
```

1. [Basic Mesh Info]

This contains unit, origin, the number of cells, cell size, and boundary condition.

Unit can be either meters, mils, inches, millimeters, or centimeters.

LowerLimitX, LowerLimitY, LowerLimitZ define the starting coordinate of the structure. In other words, In other words, in x-direction, minimum x coordinate is {LowerLimitX}, and maximum x coordinate is {LowerLimitX + sum of dx}. See the following figure that shows concept of LowerLimitX and LowerLimitY on the xy-plane. Boxes represent cells. LowerLimitZ is also the same concept.
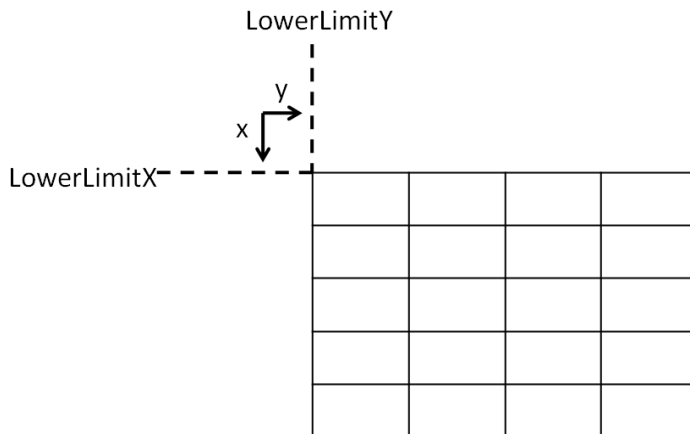
dx, dy, and dz shows dimensions of cells. Boundary condition can be PEC, PMC, or ABC. Old version of SLeEC supported all three boundary condition. However, new version of SLeEC,

which considerably improved old version of SLeEC's inefficiency in the implementation of the SLeEC algorithm, supports only PEC boundary at this time.

```
---Example--
[Basic Mesh Info]
Unit = meters
LowerLimitX = 0
LowerLimitY = 0
LowerLimitZ = 0
NumCellinXDirection = 10
NumCellinYDirection = 10
NumCellinZDirection = 5
dx = 1e-3, 1e-3, 1e-3, 1e-3, 1e-3, 1e-3, 1e-3, 1e-3, 1e-3, 1e-3
dy = 1e-3, 1e-3, 1e-3, 1e-3, 1e-3, 1e-3, 1e-3, 1e-3, 1e-3, 1e-3
dz = 5e-6, 1e-6, 1e-3, 1e-3, 1e-3
BoundaryCondition = PEC
```

2. [Material Info]

This contains the characteristics of materials that consists the structure being described.

```
Material  =  <Material  Name>,  <Material  Number>,  <Material  Type:
Metal/Dielectric>, <Relative Permittivity>, <Loss Tangent>, <Conductivity>
```

Conductivity is in unit of mho/m. Dielectric is tagged 0, Metal is tagged 1. Material Numbers of 0 and 1 are reserved for vacuum and PEC, respectively. Thus, material number begins from 2.

```
---Example---
[Material Info]
Material = FR4, 2, 0, 3.9, 0.02, 0
Material = Copper, 3, 1, 1, 0, 5.8e7
Material = Silicon, 4, 0, 11.9, 0, 10
```

3. [Structure Info]

This describes actual structure in terms of materials assigned on each cell.

For example, if materials are defined as the previous example in Material Info section, '2' indicates FR4, '3' indicates Copper, and '4' indicates Silicon. a, b, c, …, z will be used after 9. So, at most, 36 materials can be applied on the structure. Materials of cells are defined layer-by-layer. z=0 and z=NumCellinZDirection represent bottom and top layer, respectively. Each row represents material assignment of cells that shares common x coordinates. Top Left coordinate is (x, y) =(0, 0).

```
---Example---
[Structure Info]
Background = 0
z = 0
0000000000000000000000000000000
0000000000000000000000000000000
0000000000000000000000000000000
0000022222222222222222222200000
0000022222222222222222222200000
0000022222222222222222222200000
0000022222222222222222222200000
0000000000000000000000000000000
0000000000000000000000000000000
0000000000000000000000000000000

z = 1
0000000000000000000000000000000
0000000000000000000000000000000
0000000000000000000000000000000
0000033333333333333333333300000
```

```
00000333333333333333333300000
00000333333333333333333300000
00000333333333333333333300000
00000000000000000000000000000
00000000000000000000000000000
00000000000000000000000000000
```

Actual structure description file for the example shown in Figure 30 in CHAPTER IV is shown below.

```
[Basic Mesh Info]
Unit = meters
LowerLimitX = 0
LowerLimitY = 0
LowerLimitZ = 0
NumCellinXDirection = 38
NumCellinYDirection = 43
NumCellinZDirection = 16
dx = 0.001, 0.001, 0.001, 0.001, 0.001, 0.0049, 0.0001, 0.00001, 0.00002,
0.00001, 0.00004, 0.000009, 0.0000001, 0.0000001, 0.0000001, 0.0000001,
0.0000001, 0.0000001, 0.0000001, 0.0000001, 0.0000001, 0.0000001, 0.0000001,
0.0000001, 0.0000001, 0.0000001, 0.000009, 0.00004, 0.00001, 0.00002, 0.00001,
0.0001, 0.0049, 0.001, 0.001, 0.001, 0.001, 0.001
dy = 0.001, 0.001, 0.001, 0.001, 0.001, 0.0049, 0.0001, 0.00001, 0.00002,
0.00001, 0.00004, 0.000009, 0.0000001, 0.0000001, 0.0000001, 0.0000001,
0.0000001, 0.0000001, 0.0000001, 0.0000001, 0.0000001, 0.0000001, 0.0000001,
0.0000001, 0.0000001, 0.0000001, 0.0000001, 0.0000001, 0.0000001, 0.0000001,
0.0000001, 0.000009, 0.00004, 0.00001, 0.00002, 0.00001, 0.0001, 0.0049,
0.001, 0.001, 0.001, 0.001, 0.001
```

```
dz = 0.0002, 0.00000018, 0.00000018, 0.00000018, 0.00000018, 0.00000018,
0.00000018, 0.00001, 0.000005, 0.0001, 0.00002, 0.001, 0.001, 0.001, 0.001,
0.001
    BoundaryCondition = PEC

    [Material Info]
    Material = silicon, 2, 0, 11.8, 0, 0
    Material = epoxy, 3, 0, 3.9, 0, 0
    Material = air, 4, 0, 1, 0, 0
    Material = fr4, 5, 0, 4.3, 0, 0

    [Structure Info]
    z = 0
    000000000000000000000000000000000000000000000
    000000000000000000000000000000000000000000000
    000000000000000000000000000000000000000000000
    000000000000000000000000000000000000000000000
    000000000000000000000000000000000000000000000
    000002222222222222222222222222222222200000
    000002222222222222222222222222222222200000
    000002222222222222222222222222222222222200000
    000002222222222222222222222222222222222200000
    000002222222222222222222222222222222222200000
    000002222222222222222222222222222222222222200000
    000002222222222222222222222222222222222222200000
    000002222222222222222222222222222222222222200000
    000002222222222222222222222222222222222222222200000
    000002222222222222222222222222222222222222222200000
    000002222222222222222222222222222222222222222222200000
    000002222222222222222222222222222222222222222222200000
```

```
000002222222222222222222222222222222200000
000002222222222222222222222222222222200000
000002222222222222222222222222222222200000
000002222222222222222222222222222222200000
000002222222222222222222222222222222200000
000002222222222222222222222222222222200000
000002222222222222222222222222222222200000
000002222222222222222222222222222222200000
000002222222222222222222222222222222200000
000002222222222222222222222222222222200000
000002222222222222222222222222222222200000
000002222222222222222222222222222222200000
000002222222222222222222222222222222200000
000002222222222222222222222222222222200000
000002222222222222222222222222222222200000
000002222222222222222222222222222222200000
000000000000000000000000000000000000000000
000000000000000000000000000000000000000000
000000000000000000000000000000000000000000
000000000000000000000000000000000000000000
000000000000000000000000000000000000000000
```

z = 1
```
000000000000000000000000000000000000000000
000000000000000000000000000000000000000000
000000000000000000000000000000000000000000
000000000000000000000000000000000000000000
000000000000000000000000000000000000000000
000003333333333333333333333333333333300000
000003333333333333333333333333333333300000
```

```
00000333333333333333333333333333333300000
00000333333333333333333333333333333300000
00000333333333333333333333333333333300000
00000333333333333333333333333333333300000
00000333333333333333333333333333333300000
00000333333333331333333313333333333300000
00000333333333333333333333333333333300000
00000333333333331333133313333333333300000
00000333333333333333333333333333333300000
00000333333333333331333333333333333300000
00000333333333333333333333333333333300000
00000333333333333333333333333333333300000
00000333333333333333333333333333333300000
00000333333333133333133331333333333300000
00000333333333333333333333333333333300000
00000333333333333333333333333333333300000
00000333333313331333133313331333333300000
00000333333333333333333333333333333300000
00000333333333331333333313333333333300000
00000333333333333333333333333333333300000
00000333333333333333333333333333333300000
00000333333333333333333333333333333300000
00000333333333333333333333333333333300000
00000333333333333333333333333333333300000
00000333333333333333333333333333333300000
00000333333333333333333333333333333300000
00000000000000000000000000000000000000000
00000000000000000000000000000000000000000
00000000000000000000000000000000000000000
00000000000000000000000000000000000000000
```

000000000000000000000000000000000000000000

z = 2

000000000000000000000000000000000000000000
000000000000000000000000000000000000000000
000000000000000000000000000000000000000000
000000000000000000000000000000000000000000
000000000000000000000000000000000000000000
000000333333333333333333333333333333300000
000000333333333333333333333333333333300000
000000333333333333333333333333333333300000
000000333333333333333333333333333333300000
000000333333333333333333333333333333300000
000000333333333333333333333333333333300000
000000333333333333333333333333333333300000
000000333333311111111111111111333333300000
000000333333333333333333333333333333300000
000000333333333331333133133333333333300000
000000333333333333333333333333333333300000
000000333333333313333313333313333333300000
000000333333333313333333333313333333300000
000000333333111111111111111111333333300000
000000333333333333333333333333333333300000
000000333333333313333313333313333333300000
000000333333333333333333333333333333300000
000000333333333333333333333333333333300000
000000333333313331333133313331333333300000
000000333333333333333333333333333333300000
000000333333111111111111111111333333300000
000000333333333333333333333333333333300000

147

```
000003333333333333333333333333333333300000
000003333333333333333333333333333333300000
000003333333333333333333333333333333300000
000003333333333333333333333333333333300000
000003333333333333333333333333333333300000
000003333333333333333333333333333333300000
000000000000000000000000000000000000000000
000000000000000000000000000000000000000000
000000000000000000000000000000000000000000
000000000000000000000000000000000000000000
000000000000000000000000000000000000000000
```

z = 3

```
000000000000000000000000000000000000000000
000000000000000000000000000000000000000000
000000000000000000000000000000000000000000
000000000000000000000000000000000000000000
000000000000000000000000000000000000000000
000003333333333333333333333333333333300000
000003333333333333333333333333333333300000
000003333333333333333333333333333333300000
000003333333333333333333333333333333300000
000003333333333333333333333333333333300000
000003333333333333333333333333333333300000
000003333333333333333333333333333333300000
000003333333333331333133313333333333300000
000003333333333333333333333333333333300000
000003333333333331333133313333333333300000
000003333333333333333333333333333333300000
000003333333333133333133333133333333300000
```

148

```
00000333333333333333333333333333333300000
00000333333333333333333333333333333300000
00000333333333333333333333333333333300000
00000333333331333331333331333333333300000
00000333333333333333333333333333333300000
00000333333333333333333333333333333300000
00000333333313331333133313331333333300000
00000333333333333333333333333333333300000
00000333333333331333133313333333333300000
00000333333333333333333333333333333300000
00000333333333333333333333333333333300000
00000333333333333333333333333333333300000
00000333333333333333333333333333333300000
00000333333333333333333333333333333300000
00000333333333333333333333333333333300000
00000333333333333333333333333333333300000
00000000000000000000000000000000000000000
00000000000000000000000000000000000000000
00000000000000000000000000000000000000000
00000000000000000000000000000000000000000
00000000000000000000000000000000000000000

z = 4
00000000000000000000000000000000000000000
00000000000000000000000000000000000000000
00000000000000000000000000000000000000000
00000000000000000000000000000000000000000
00000000000000000000000000000000000000000
00000333333333333333333333333333333300000
00000333333333333333333333333333333300000
```

```
000003333333333333333333333333333333300000
000003333333333333333333333333333333300000
000003333333333333333333333333333333300000
000003333333333333333333333333333333300000
000003333333333333333333333333333333300000
000003333333133313331333133313333333300000
000003333333133333331333333331333333300000
000003333333133313331333133313333333300000
000003333333133313333331333313333333300000
000003333333133131333111131331333333300000
000003333333133131333333313133313333333300000
000003333333133131333333313133133333300000
000003333333133131333333313133133333300000
000003333333133131333333313133133333300000
000003333333133131111133313133133333300000
000003333333133331333333313333313333333300000
000003333333133331333333313333313333333300000
000003333333113331333133313331133333300000
000003333333133333331333333331333333300000
000003333333133331333133313331333333300000
000003333333333333333333333333333333300000
000003333333333333333333333333333333300000
000003333333333333333333333333333333300000
000003333333333333333333333333333333300000
000003333333333333333333333333333333300000
000003333333333333333333333333333333300000
000003333333333333333333333333333333300000
000000000000000000000000000000000000000000
000000000000000000000000000000000000000000
000000000000000000000000000000000000000000
000000000000000000000000000000000000000000
```

000000000000000000000000000000000000000000

z = 5

000000000000000000000000000000000000000000
000000000000000000000000000000000000000000
000000000000000000000000000000000000000000
000000000000000000000000000000000000000000
000000000000000000000000000000000000000000
000000333333333333333333333333333333300000
000000333333333333333333333333333333300000
000000333333333333333333333333333333300000
000000333333333333333333333333333333300000
000000333333333333333333333333333333300000
000000333333333333333333333333333333300000
000000333333333333333333333333333333300000
000000333333333333333311333333333333300000
000000333333333333333333333333333333300000
000000333333333333333333333333333333300000
000000333333333333333333333333333333300000
000000333333333333333333333333333333300000
000000333333333333333333333333333333300000
000000333333313333333333333313333333300000
000000333333333333333333333333333333300000
000000333333333333333333333333333333300000
000000333333333333333333333333333333300000
000000333333333333333333333333333333300000
000000333333333333333333333333333333300000
000000333333333333333333333333333333300000
000000333333333333333133333333333333300000
000000333333333333333333333333333333300000

151

```
00000333333333333333333333333333333300000
00000333333333333333333333333333333300000
00000333333333333333333333333333333300000
00000333333333333333333333333333333300000
00000333333333333333333333333333333300000
00000333333333333333333333333333333300000
00000000000000000000000000000000000000000
00000000000000000000000000000000000000000
00000000000000000000000000000000000000000
00000000000000000000000000000000000000000
00000000000000000000000000000000000000000
```

z = 6

```
00000000000000000000000000000000000000000
00000000000000000000000000000000000000000
00000000000000000000000000000000000000000
00000000000000000000000000000000000000000
00000000000000000000000000000000000000000
00000333333333333333333333333333333300000
00000333333333333333333333333333333300000
00000333333333333333333333333333333300000
00000333331111111111111111111133333300000
00000333333333333333313333333333333333300000
00000333333333333333313333333333333333300000
00000333133333333333313333333333331333300000
00000333133333333333313333333333331333300000
00000333133333333333333333333331333300000
00000333133333333333333333333331333300000
00000333133333333333333333333331333300000
00000333133333333333333333333331333300000
```

```
000000333133333333333333333333333133300000
000000333111113333333333333111111133300000
000000333133333333333333333333333133300000
000000333133333333333333333333333133300000
000000333133333333333333333333333133300000
000000333133333333333333333333333133300000
000000333133333333333333333333333133300000
000000333133333333333333333333333133300000
000000333133333333333133333333333133300000
000000333133333333333133333333333133300000
000000333333333333333133333333333333300000
000000333333333333333133333333333333300000
000000333333111111111111111111133333300000
000000333333333333333333333333333333300000
000000333333333333333333333333333333300000
000000333333333333333333333333333333300000
000000000000000000000000000000000000000000
000000000000000000000000000000000000000000
000000000000000000000000000000000000000000
000000000000000000000000000000000000000000
000000000000000000000000000000000000000000

z = 7
000000000000000000000000000000000000000000
000000000000000000000000000000000000000000
000000000000000000000000000000000000000000
000000000000000000000000000000000000000000
000000000000000000000000000000000000000000
000000333333333333333333333333333333300000
000000333333333333333333333333333333300000
```

```
000000333333333333333333333333333333300000
000000333331111111111111111111133333300000
000000333333333333333333333333333333300000
000000333333333333333333333333333333300000
000000333133333333333333333333333133300000
000000333133333333333333333333333133300000
000000333133333333333333333333333133300000
000000333133333333333333333333333133300000
000000333133333333333333333333333133300000
000000333133333333333333333333333133300000
000000333133333333333333333333333133300000
000000333133333333333333333333333133300000
000000333133333333333333333333333133300000
000000333133333333333333333333333133300000
000000333133333333333333333333333133300000
000000333133333333333333333333333133300000
000000333133333333333333333333333133300000
000000333133333333333333333333333133300000
000000333133333333333333333333333133300000
000000333333333333333333333333333333300000
000000333333333333333333333333333333300000
000000333331111111111111111111133333300000
000000333333333333333333333333333333300000
000000333333333333333333333333333333300000
000000333333333333333333333333333333300000
000000000000000000000000000000000000000000
000000000000000000000000000000000000000000
000000000000000000000000000000000000000000
000000000000000000000000000000000000000000
```

154

000000000000000000000000000000000000000000000

z = 8

000000000000000000000000000000000000000000000
000000000000000000000000000000000000000000000
000000000000000000000000000000000000000000000
000000000000000000000000000000000000000000000
000000000000000000000000000000000000000000000
000004444444444444444444444444444400000
000004441111111111111111111111144400000
000004444441111111111111111114444400000
000004144441111111111111111111144441400000
000004144444444444444444444444441400000
000004144444444444444444444444441400000
000004111444444444444444444444444111400000
000004111444444444444444444444444111400000
000004111444444444444444444444444111400000
000004111444444444444444444444444111400000
000004111444444444444444444444444111400000
000004111444444444444444444444444111400000
000004111444444444444444444444444111400000
000004111444444444444444444444444111400000
000004111444444444444444444444444111400000
000004111444444444444444444444444111400000
000004111444444444444444444444444111400000
000004111444444444444444444444444111400000
000004111444444444444444444444444111400000
000004111444444444444444444444444111400000
000004111444444444444444444444444111400000

155

```
0000041444444444444444444444444441400000
0000041444444444444444444444444441400000
0000041444411111111111111111144441400000
0000044444411111111111111111114444400000
0000044411111111111111111111111144400000
0000044444444444444444444444444444400000
0000000000000000000000000000000000000000
0000000000000000000000000000000000000000
0000000000000000000000000000000000000000
0000000000000000000000000000000000000000
0000000000000000000000000000000000000000
```

z = 9

```
0000000000000000000000000000000000000000
0000000000000000000000000000000000000000
0000000000000000000000000000000000000000
0000000000000000000000000000000000000000
0000000000000000000000000000000000000000
0000044444444444444444444444444444400000
0000044411111111111111111111111144400000
0000044444444444444444444444444444400000
0000041444444444444444444444444441400000
0000041444444444444444444444444441400000
0000041444444444444444444444444441400000
0000041444444444444444444444444441400000
0000041444444444444444444444444441400000
0000041444444444444444444444444441400000
0000041444444444444444444444444441400000
0000041444444444444444444444444441400000
0000041444444444444444444444444441400000
```

```
00000414444444444444444444444444441400000
00000414444444444444444444444444441400000
00000414444444444444444444444444441400000
00000414444444444444444444444444441400000
00000414444444444444444444444444441400000
00000414444444444444444444444444441400000
00000414444444444444444444444444441400000
00000414444444444444444444444444441400000
00000414444444444444444444444444441400000
00000414444444444444444444444444441400000
00000414444444444444444444444444441400000
00000414444444444444444444444444441400000
00000414444444444444444444444444441400000
00000414444444444444444444444444441400000
00000444444444444444444444444444444400000
00000444111111111111111111111111144400000
00000444444444444444444444444444444400000
00000000000000000000000000000000000000000
00000000000000000000000000000000000000000
00000000000000000000000000000000000000000
00000000000000000000000000000000000000000
00000000000000000000000000000000000000000

z = 10
00000000000000000000000000000000000000000
00000000000000000000000000000000000000000
00000000000000000000000000000000000000000
00000000000000000000000000000000000000000
00000000000000000000000000000000000000000
00000000011111111111111111111111100000000
00000000011111111111111111111111100000000
```

```
00000000000000000000000000000000000000000000
00000011000000000000000000000000000001100000
00000011000000000000000000000000000001100000
00000011000000000000000000000000000001100000
00000011000000000000000000000000000001100000
00000011000000000000000000000000000001100000
00000011000000000000000000000000000001100000
00000011000000000000000000000000000001100000
00000011000000000000000000000000000001100000
00000011000000000000000000000000000001100000
00000011000000000000000000000000000001100000
00000011000000000000000000000000000001100000
00000011000000000000000000000000000001100000
00000011000000000000000000000000000001100000
00000011000000000000000000000000000001100000
00000011000000000000000000000000000001100000
00000011000000000000000000000000000001100000
00000011000000000000000000000000000001100000
00000011000000000000000000000000000001100000
00000011000000000000000000000000000001100000
00000011000000000000000000000000000001100000
00000011000000000000000000000000000001100000
00000011000000000000000000000000000001100000
00000000000000000000000000000000000000000000
00000000111111111111111111111111100000000
00000000111111111111111111111111100000000
00000000000000000000000000000000000000000000
00000000000000000000000000000000000000000000
00000000000000000000000000000000000000000000
00000000000000000000000000000000000000000000
```

158

00000000000000000000000000000000000000000

z = 11
00000000000000000000000000000000000000000
00000000000000000000000000000000000000000
00000000000000000000000000000000000000000
00000000000000000000000000000000000000000
00000000000000000000000000000000000000000
00000000000000000000000000000000000000000
00000000000000000000000000000000000000000
00000000000000000000000000000000000000000
00000000000000000000000000000000000000000
00000000000000000000000000000000000000000
00000000000000000000000000000000000000000
00000000000000000000000000000000000000000
00000000000000000000000000000000000000000
00000000000000000000000000000000000000000
00000000000000000000000000000000000000000
00000000000000000000000000000000000000000
00000000000000000000000000000000000000000
00000000000000000000000000000000000000000
00000000000000000000000000000000000000000
00000000000000000000000000000000000000000
00000000000000000000000000000000000000000
00000000000000000000000000000000000000000
00000000000000000000000000000000000000000
00000000000000000000000000000000000000000
00000000000000000000000000000000000000000
00000000000000000000000000000000000000000

```
0000000000000000000000000000000000000000000
0000000000000000000000000000000000000000000
0000000000000000000000000000000000000000000
0000000000000000000000000000000000000000000
0000000000000000000000000000000000000000000
0000000000000000000000000000000000000000000
0000000000000000000000000000000000000000000
0000000000000000000000000000000000000000000
0000000000000000000000000000000000000000000
0000000000000000000000000000000000000000000
0000000000000000000000000000000000000000000
```

z = 12

```
0000000000000000000000000000000000000000000
0000000000000000000000000000000000000000000
0000000000000000000000000000000000000000000
0000000000000000000000000000000000000000000
0000000000000000000000000000000000000000000
0000000000000000000000000000000000000000000
0000000000000000000000000000000000000000000
0000000000000000000000000000000000000000000
0000000000000000000000000000000000000000000
0000000000000000000000000000000000000000000
0000000000000000000000000000000000000000000
0000000000000000000000000000000000000000000
0000000000000000000000000000000000000000000
0000000000000000000000000000000000000000000
0000000000000000000000000000000000000000000
0000000000000000000000000000000000000000000
0000000000000000000000000000000000000000000
```

```
0000000000000000000000000000000000000000000000000
0000000000000000000000000000000000000000000000000
0000000000000000000000000000000000000000000000000
0000000000000000000000000000000000000000000000000
0000000000000000000000000000000000000000000000000
0000000000000000000000000000000000000000000000000
0000000000000000000000000000000000000000000000000
0000000000000000000000000000000000000000000000000
0000000000000000000000000000000000000000000000000
0000000000000000000000000000000000000000000000000
0000000000000000000000000000000000000000000000000
0000000000000000000000000000000000000000000000000
0000000000000000000000000000000000000000000000000
0000000000000000000000000000000000000000000000000
0000000000000000000000000000000000000000000000000
0000000000000000000000000000000000000000000000000
0000000000000000000000000000000000000000000000000
0000000000000000000000000000000000000000000000000
0000000000000000000000000000000000000000000000000
0000000000000000000000000000000000000000000000000
0000000000000000000000000000000000000000000000000
```

z = 13
```
0000000000000000000000000000000000000000000000000
0000000000000000000000000000000000000000000000000
0000000000000000000000000000000000000000000000000
0000000000000000000000000000000000000000000000000
0000000000000000000000000000000000000000000000000
0000000000000000000000000000000000000000000000000
0000000000000000000000000000000000000000000000000
```

0000000000000000000000000000000000000000000
0000000000000000000000000000000000000000000
0000000000000000000000000000000000000000000
0000000000000000000000000000000000000000000
0000000000000000000000000000000000000000000
0000000000000000000000000000000000000000000
0000000000000000000000000000000000000000000
0000000000000000000000000000000000000000000
0000000000000000000000000000000000000000000
0000000000000000000000000000000000000000000
0000000000000000000000000000000000000000000
0000000000000000000000000000000000000000000
0000000000000000000000000000000000000000000
0000000000000000000000000000000000000000000
0000000000000000000000000000000000000000000
0000000000000000000000000000000000000000000
0000000000000000000000000000000000000000000
0000000000000000000000000000000000000000000
0000000000000000000000000000000000000000000
0000000000000000000000000000000000000000000
0000000000000000000000000000000000000000000
0000000000000000000000000000000000000000000
0000000000000000000000000000000000000000000
0000000000000000000000000000000000000000000
0000000000000000000000000000000000000000000
0000000000000000000000000000000000000000000
0000000000000000000000000000000000000000000
0000000000000000000000000000000000000000000
0000000000000000000000000000000000000000000
0000000000000000000000000000000000000000000
0000000000000000000000000000000000000000000
0000000000000000000000000000000000000000000

162

0000000000000000000000000000000000000000

z = 14

0000000000000000000000000000000000000000
0000000000000000000000000000000000000000
0000000000000000000000000000000000000000
0000000000000000000000000000000000000000
0000000000000000000000000000000000000000
0000000000000000000000000000000000000000
0000000000000000000000000000000000000000
0000000000000000000000000000000000000000
0000000000000000000000000000000000000000
0000000000000000000000000000000000000000
0000000000000000000000000000000000000000
0000000000000000000000000000000000000000
0000000000000000000000000000000000000000
0000000000000000000000000000000000000000
0000000000000000000000000000000000000000
0000000000000000000000000000000000000000
0000000000000000000000000000000000000000
0000000000000000000000000000000000000000
0000000000000000000000000000000000000000
0000000000000000000000000000000000000000
0000000000000000000000000000000000000000
0000000000000000000000000000000000000000
0000000000000000000000000000000000000000
0000000000000000000000000000000000000000
0000000000000000000000000000000000000000
0000000000000000000000000000000000000000

```
000000000000000000000000000000000000000000
000000000000000000000000000000000000000000
000000000000000000000000000000000000000000
000000000000000000000000000000000000000000
000000000000000000000000000000000000000000
000000000000000000000000000000000000000000
000000000000000000000000000000000000000000
000000000000000000000000000000000000000000
000000000000000000000000000000000000000000
000000000000000000000000000000000000000000
000000000000000000000000000000000000000000
```

```
z = 15
```

```
000000000000000000000000000000000000000000
000000000000000000000000000000000000000000
000000000000000000000000000000000000000000
000000000000000000000000000000000000000000
000000000000000000000000000000000000000000
000000000000000000000000000000000000000000
000000000000000000000000000000000000000000
000000000000000000000000000000000000000000
000000000000000000000000000000000000000000
000000000000000000000000000000000000000000
000000000000000000000000000000000000000000
000000000000000000000000000000000000000000
000000000000000000000000000000000000000000
000000000000000000000000000000000000000000
000000000000000000000000000000000000000000
000000000000000000000000000000000000000000
000000000000000000000000000000000000000000
```

164

```
00000000000000000000000000000000000000000
00000000000000000000000000000000000000000
00000000000000000000000000000000000000000
00000000000000000000000000000000000000000
00000000000000000000000000000000000000000
00000000000000000000000000000000000000000
00000000000000000000000000000000000000000
00000000000000000000000000000000000000000
00000000000000000000000000000000000000000
00000000000000000000000000000000000000000
00000000000000000000000000000000000000000
00000000000000000000000000000000000000000
00000000000000000000000000000000000000000
00000000000000000000000000000000000000000
00000000000000000000000000000000000000000
00000000000000000000000000000000000000000
00000000000000000000000000000000000000000
00000000000000000000000000000000000000000
00000000000000000000000000000000000000000
00000000000000000000000000000000000000000
00000000000000000000000000000000000000000
```

V.   Simulation Setting File

SLeEC simulation setting file (*.ss extension) contains information about simulation setting such as simulation time, time step, definition of source and probes.

Format for defining simulation time

```
Simulation Time = <simulation time in second>
```

Next, time step for describing time-domain waveform is defined. This time step is just the resolution of source and output time domain waveform and not directly related to the performance of the simulation since SLeEC is not marching-on-time scheme.

```
dt = <time step in second>
```

Source definition format is as follows:

```
Source = <x Coordinate(s)>, <y Coordinate(s)>, <z Coordinate(s)>,
<Direction of Source>, <Source Type>, <Source Parameter 1>, <Source Parameter
2>
```

Unit and coordinate system for definition of source and probing points are same as ones in the structure file.

When source is excited along several cells in a row, then source's starting point and ending point can be can be represented as (a:b) form, for example, if current is flowing from (x=1,y=1,z=0) to (x=1,y=1,z=1), then, its coordinates can be represented as (x=1,y=1,z=0:1). Source is heading to the positive direction on indicated axis. For example, if source's direction is z, then positive current is flowing toward z direction. Source Type can be Gaussian, GaussianDerivative, or ModulatedGaussian. For Gaussian and GaussianDerivative, Source parameter 1 is timing of pulse's center and Source parameter 2 is sigma value (standard deviation). For Modulated Gaussian, Source parameter 1 is also center of pulse and Source parameter 2 is bandwidth of pulse in Hz.

Format for defining a probe

```
Probe = <x Coordinate>, <y Coordinate>, <z Coordinate>, <Probing Field>
```

Probing field can be either Ex, Ey, or Ez.

166

```
---Example--
[Simulation Info]
Simulation Time = 100e-9
Source = 30, 30, .1:.5, z, Gaussian, 2.5e-9, 7.5e-10
Probe = 5, 3, 1, Ez
Probe = 3, 3, 2, Ex
```

Actual simulation setup file for the example shown in Figure 30 in CHAPTER IV is shown below.

```
[Simulation Info]
Simulation Time = 5e-9
dt = 5e-13
Source = 1.00897e-2, .0099, 0:3e-4, z, GaussianDerivative, 2.5e-9, 7.5e-11
Probe = 1.00897e-2, .0099, 2.0081e-4, Ez
Probe = 1.00897e-2, 0.01028, 2.0081e-4, Ez
```

VI.   Time-domain Waveform File

SLeEC produces time-domain waveform file as an output. First column in the file is time line in second. Second column is source current waveform in Ampere. Following columns represent probed E-field values in V/m.

VII.   Laguerre Coefficient File (optional)

Number at ith row and jth column represents coefficient for (i-1)th basis function of jth probe point.

APPENDIX D: LAGUERRE-FDTD FORMULATION FOR VARIOUS BOUNDARY CONDITIONS

I.   Perfect Electric Conductor (PEC) Boundary Condition

In the PEC boundary, the tangential electric fields to the boundary are set to zero.

II.   Perfect Magnetic Conductor (PMC) Boundary Condition

In the PMC boundary, the tangential magnetic fields to the boundary are set to zero.

III.   Absorbing Boundary Condition

In [47], the Laguerre-domain formulation for Mur's 2nd order absorbing boundary conditions has been proposed and is summarized in this section.

Taking the electric field E_x at the boundary $z = 0$ for example, the Mur's second-order ABC for 3-D Maxwell's is [48]

$$\left[\frac{1}{v}\frac{\partial^2}{\partial z \partial t} - \frac{1}{v^2}\frac{\partial^2}{\partial t^2} + \frac{1}{2}\left(\frac{\partial^2}{\partial x^2} + \frac{\partial^2}{\partial y^2}\right)\right]E_x\big|_{z=0} = 0, \tag{216}$$

where v is the local wave speed.

Inserting (127) and (128) into (216) and applying the temporal testing procedure with $\varphi_m(st)$, we get

$$\begin{aligned}
\frac{s}{v}\frac{\partial}{\partial z}&\left[\frac{1}{2}E_x^m(\vec{r}) + \sum_{l=0,m>0}^{m-1} E_x^l(\vec{r})\right] \\
&- \frac{s^2}{v^2}\left[\frac{1}{4}E_x^m(\vec{r}) + \sum_{l=0,m>0}^{m-1}(m-l)E_x^l(\vec{r})\right] \\
&+ \frac{1}{2}\left(\frac{\partial^2}{\partial x^2} + \frac{\partial^2}{\partial y^2}\right)E_x^m(\vec{r}) = 0.
\end{aligned} \tag{217}$$

168

Using the second-order central difference scheme at an auxiliary grid point $(i, j, 1+1/2)$, we can obtain

$$\left(-\frac{s}{2v\Delta z_1} - \frac{s^2}{4v^2} - \frac{1}{2\Delta x_{i-1}\Delta x_i} - \frac{1}{2\Delta y_{j-1}\Delta y_j}\right) E_x^m \Big|_{i,j,1}$$

$$+ \left(\frac{2}{2v\Delta z_1} - \frac{s^2}{4v^2} - \frac{1}{2\Delta x_{i-1}\Delta x_i}\right.$$

$$\left. - \frac{1}{2\Delta y_{j-1}\Delta y_j}\right) E_x^m \Big|_{i,j,2} + \frac{E_x^m \big|_{i-1,j,1} + E_x^m \big|_{i-1,j,2}}{2\Delta x_{i-1}(\Delta x_{i-1} + \Delta x_i)}$$

$$+ \frac{E_x^m \big|_{i+1,j,1} + E_x^m \big|_{i+1,j,2}}{2\Delta x_i(\Delta x_{i-1} + \Delta x_i)}$$

$$+ \frac{E_x^m \big|_{i,j-1,1} + E_x^m \big|_{i,j-1,2}}{2\Delta y_{j-1}(\Delta y_{j-1} + \Delta y_j)} \tag{218}$$

$$+ \frac{E_x^m \big|_{i,j+1,1} + E_x^m \big|_{i,j+1,2}}{2\Delta y_j(\Delta y_{j-1} + \Delta y_j)}$$

$$= -\frac{s}{v\Delta z_1} \sum_{l=0,m>0}^{m-1} \left(E_x^l \big|_{i,j,2} - E_x^l \big|_{i,j,1}\right)$$

$$+ \frac{s^2}{2v^2} \sum_{l=0,m>0}^{m-1} (m-l)\left(E_x^l \big|_{i,j,2} + E_x^l \big|_{i,j,1}\right).$$

The other ABC equations at $z = z_{max}$, $x = 0$, $x = x_{max}$, $y = 0$, and $y = y_{max}$ can be constructed in a similar way.

REFERENCES

[1] E. Mollick, "Estabiishing Moore's Law," *IEEE Annals of the History of Computing,* vol. 28, no. 3, pp. 62-75, Jul.-Sep. 2006.

[2] S. Adee, "the data: 37 Years of Moore's Law," *Solid-State Electronics,* vol. 45, no. 5, p. 56, May 2008.

[3] Jan 2011. [Online]. Available: http://en.wikipedia.org/wiki/System-on-a-chip.

[4] R. R. Tummala, "Moore's Law Meets Its Match," *IEEE Spectrum,,* vol. 43, no. 6, pp. 44-49, June 2006.

[5] R. R. Tummala, "Packaging: past, present and future," in *Electronic Packaging Technology, 2005 6th International Conference on* , 2005.

[6] R. R. Tummala, *Fundamentals of Microsystems Packaging*, McGraw-Hill, 2001.

[7] M. Swaminathan and E. Engin, *Power integrity modeling and design for semiconductors and systems*, 1st ed., Prentice Hall PTR, 2007.

[8] B. Young, *Digital Signal Integrity: Modeling and Simulation with Interconncts and Packages*, Prentice PTR, 2000.

[9] K. S. Yee, "Numerical solution of initial boundary value problems involving Maxwell's equations in isotropic media," *IEEE Trans. Antennas Propag.,* vol. 14, no. 3, pp. 302-307, Mar 1966.

[10] A. Taflove and S. C. Hagness, *Computational Electrodynamics: The Finite-Difference Time-Domain Method*, 3 ed., Boston: Artech House, 2005.

[11] M. Krumpholz and L. Katehi, "MRTD: New time-domain schemes based on multiresolution analysis," *IEEE Trans. on Microwave Theory and Techniques,* vol. 44,

pp. 555-571, April 1996.

[12] R. Holland and L. Simpson, "Finite-difference analysis of EMP coupling to thin struts and wires," *IEEE Trans. on Electromagnetic Compatibility,* vol. 23, pp. 88-97, May 1981.

[13] M. N. Ozisik, *Finite Difference Methods in Heat Transfer*, Boca Raton, FL: CRC Press, 1994.

[14] Griffit and Michell, *The Finite Difference Method in Practical Differential Equations*, New York: Wiley, 1980.

[15] T. Namiki and K. Ito, "A new FDTD algorithm free from the CFL condition restraint for a 2D-TE wave," in *IEEE AP-S Symp. Dig.*, Orlando, FL, 1999.

[16] S. G. Garcia, T. Lee and S. C. Hagness, "On the Accuracy of the ADI-FDTD Method," *IEEE Antennas and Wireless Propagaion Letters,* vol. 1, pp. 31-34, 2002.

[17] F. Zheng, Z. Chen and J. Zhang, "Toward the development of a three-dimensional unconditionally," *IEEE Trans. Microwave Theory Tech.,* vol. 48, pp. 1050-1058, 2000.

[18] F. Zheng and Z. Chen, "Numerical Dispersion Analysis of the Unconditionally Stable 3-D ADI–FDTD Method," *IEEE Trans.Microwave Theory and Technique,* vol. 49, no. 5, pp. 1006-1009, May 2001.

[19] Y.-S. Chung, T. K. Sarkar, B. H. Jung and M. Salazar-Palma, "An unconditionally stable scheme for the finite-difference time-domain method," *IEEE Trans. Microw. Theory Tech.,* vol. 51, no. 3, pp. 697-704, Mar 2003.

[20] I. S. Gradshteyn, I. M. Ryzhik and A. Jeffrey, *Table of Integrals, Series, and Products*, 5th ed., Academic Press, 1994.

[21] K. Srinivasan, M. Swaminathan and E. Engin, "Enhancement of Laguerre-FDTD with

Initial Conditions for Fast Transient EM/Circuit Simulation," in *Electronic Components and Technology Conference (ECTC)*, 2007.

[22] K. Srinivasan, E. Engin and M. Swaminathan, "Fast FDTD Simulation Using Laguerre Polynomials in MNA Framework," in *International Symposium on Electromagnetic Compatibility*, 2007.

[23] K. Srinivasan, *Multiscale EM and Circuit Simulation Using the Laguerre-FDTD Scheme for Package-Aware Integrated-Circuit Design,* PhD Thesis, Georgia Institute of Technology, 2008.

[24] K. Srinivasan, E. Engin and M. Swaminathan, "Fast FDTD simulation of multiscale 3-D models using Laguerre-MNA," in *IEEE Workshop Signal Propag. Interconnects*, May 2007.

[25] S. M. Rao, *Time-domain Electromagnetics*, 1st ed., Academic Press, 1999.

[26] L. T. Pillage, R. A. Rohrer and C. Visweswariah, Electronic Circuit and System Simulation Methods, McGraw-Hill, 1994.

[27] L. Nagel and D. Pederson, *SPICE (Simulation Program with Integrated Circuit Emphasis).*

[28] K. Srinivasan, P. Yadav, E. Engin and M. Swaminathan, "Choosing the Right Number of Basis Functions in Multiscale Transient Simulation Using Laguerre Polynomials," in *IEEE 19th Conference on Electrical Performance of Electronic Packaging*, 2007.

[29] A. Reineix and B. Jecko, "Analysis of microstrip patch antennas using finite difference time domain method," *IEEE Trans. Antennas Propagation,* vol. 37, no. 11, pp. 1361-1369, 1989.

[30] M. Piket-May, A. Taflove and J. Baron, "FD-TD modeling of digital signal

propagation in 3-D circuits with passive and active loads," *IEEE Trans. Microwave Theory Tech.,* vol. 42, no. 8, pp. 1514-1523, 1994.

[31] R. J. Luebbers and H. S. langdon, "A simple feed model that reduces time steps needed for FDTD antenna and microstrip calculations," *IEEE Trans. Antennas Propagation,* vol. 44, no. 7, pp. 1000-1005, 1996.

[32] C. Birtcher, S. Georgakopoulos and C. Balanis, "Artificial loss in FDTD predictions of high-Q cavities," in *Antennas and Propagation Society International Symposium, 2000. IEEE* , 2000.

[33] R. Luebbers, F. Hunsberger, K. Kunz, R. Standler and M. Schneider, "A frequency-dependent finite-difference time-domain formulation for dispersive materials," *IEEE Trans. Electromagnetic Compatibility,* vol. 32, no. 3, pp. 222-227, aug 1990.

[34] M. Koledintseva, K. Rozanov, A. Orlandi and J. Drewniak, "Extraction of Lorentzian and Debye parameters of dielectric and magnetic dispersive materials for FDTD modeling,," *Journal of Electrical Engineering,* vol. 53, no. 9, pp. 97-100, 2002.

[35] J. Stewart, *Calculus*, 6th Edition ed., Brooks Cole, 2007.

[36] K. Srinivasan, M. Swaminathan and E. Engin, "Overcoming limitations of Laguerre-FDTD for fast time-domain EM simulation," in *IEEE MTT-S Int. Microwave Symp.*, Jun. 2007.

[37] W. Shao, B.-Z. Wang and X.-F. Liu, "Second-Order Absorbing Boundary Conditions for Marching-on-in-Order Scheme," *IEEE Microwave and Wireless Components Letters,* vol. 16, no. 5, pp. 308-310, May 2006.

VITA

Myunghyun Ha was born in Daegu, South Korea. He received his B.S. degree and the M.S. degree, both in electrical engineering, from Korea Advanced Institute of Science and Technology (KAIST), Daejeon, South Korea, in 2004 and 2007, respectively. He is currently pursuing his Ph.D. degree in the school of electrical and computer engineering (ECE) at the Georgia Institute of Technology, Atlanta.

In the spring of 2004 and from June 2006 to August 2007, he was with Terahertz Interconnection and Package Laboratory at Korea Advanced Institute of Science and Technology, Daejeon, South Korea, where he was involved in the design of a number of mixed-signal system-in-package (SiP) products and the development of SiP design methodology for noise isolation in mixed-signal 3-D stacked SiP. In the summer of 2009, he interned at Rambus where he was involved in the development the automated simulation environment for signal integrity and power integrity analysis of interface between DRAM controller and chip and the investigation of terminal-reduced models for system-level simultaneous switching output (SSO) noise analysis. He is currently a graduate research assistant in Mixed Signal Design Group at the Georgia Institute of Technology, Atlanta. From November 2011, he will be with Intel Corporation as an analog engineer.

His research interests include computational electromagnetics, signal/power integrity for high-speed digital design, high-frequency and high-speed mixed signal board/package design and modeling, and silicon interposer with through silicon via (TSV) technology.